

Study on synthesis processes and characterization of tin and carbon nanocomposites

BORUDE Ranjit Rohidas

2019

Department of Electrical Engineering and Computer Science,

Graduate School of Engineering, Nagoya University.

Contents

Chapter 1 Introduction

1.1 Materials: Science and synthesis	01
1.1.1 Metal oxides: tin oxide (SnO ₂).....	03
1.1.2 Conducting polymers: polyaniline (PANI).....	06
1.1.3 Carbon materials	10
1.2 Material functionalization: Composites	15
1.2.1 Tin oxide-polyaniline composite	16
1.2.2 Tin oxide -graphene composite	18
1.3 Plasma processing	24
1.3.1 Atmospheric pressure plasma for surface treatment	25
1.3.2 In-liquid plasma for nanomaterial synthesis	26
1.4 Objective and composition of this dissertation	29
References	32

Chapter 2 Experimental setup and evaluation methods

2.1 Synthesis and surface treatment methods	37
2.1.1 Synthesis of tin oxide (sol-gel method).....	37
2.1.2 Synthesis of polyaniline (chemical oxidative method)	39
2.1.3 Deposition of carbon films (magnetron sputtering method)	41
2.1.4 Synthesis of tin oxide-graphene composite (in-liquid plasma method)	43
2.1.5 Low-temperature atmospheric pressure plasma surface treatment	45
2.2 Plasma diagnostic technique	47
2.2.1 Optical emission spectroscopy (OES)	47

Contents

2.2.2 Electrical parameters for plasma process	48
2.3 Evaluation methods	49
2.3.1 Scanning electron microscopy (SEM)	49
2.3.2 Energy dispersive X-ray spectroscopy (EDS)	52
2.3.3 Atomic force microscopy (AFM).....	54
2.3.4 Transmission electron microscopy (TEM)	56
2.3.5 X-ray diffraction (XRD)	59
2.3.6 X-ray photoelectron spectroscopy (XPS).....	62
2.3.7 Near-edge X-ray absorption fine structure spectroscopy (NEXAFS)	65
2.3.8 Fourier transform infrared spectroscopy (FTIR)	67
2.3.9 Raman spectroscopy	68
2.3.10 Optical spectrophotometry	71
2.4 Gas sensing measurements.....	72
2.4.1 Sample preparation	72
2.4.2 Gas sensing set-up	73
References	76

Chapter 3 *Ex-situ* binding of Sn-PANI composites – Synthesis and gas sensing properties

3.1 Introduction	78
3.2 Experimental details	80
3.2.1 Synthesis of PANI	80
3.2.2 Synthesis of SnO ₂	80
3.2.3 Synthesis of Sn-PANI composite	81
3.2.4 Sample preparation	81
3.3 Results and discussion	83
3.3.1 Surface morphology	83
3.3.2 Chemical composition	84
3.3.3 Crystal structure analysis	85

Contents

3.3.4 Ammonia sensing properties of Sn-PANI composite.....	87
3.3.5 Humidity sensing properties of Sn-PANI composite	89
3.4 Conclusion	91
References	92

Chapter 4 Surface and bulk modifications of magnetron-sputtered carbon films by post treatments of atmospheric pressure plasma

4.1 Introduction	94
4.2 Deposition of carbon films.....	96
4.3 Effect of power density variation on carbon films	98
4.3.1 Deposition rate	98
4.3.2 Surface morphology.....	99
4.3.3 Microstructure of carbon films	100
4.3.4 Optical and electrical properties of carbon films.....	103
4.4 APP post-treatments of as-deposited carbon films	106
4.5 Effect of APP post-treatments on carbon films	107
4.5.1 Surface morphology.....	108
4.5.2 Surface roughness	110
4.5.3 Chemical structure.....	113
4.5.4 Microstructure.....	116
4.3.5 Optical and electrical properties of APP treated carbon films	118
4.6 Discussion	120
4.7 Conclusion	122
References	124

Chapter 5 SnO₂ nanoparticle bound graphene composites - In-liquid plasma assisted synthesis using SnO₂ dispersed ethanol

5.1 Introduction 126

5.2 Experimental details 128

5.3 Results and discussion 132

 5.3.1 Morphology and elemental distribution 132

 5.3.2 Chemical composition 136

 5.3.3 Microstructure analysis 137

 5.3.4 Crystal structure analysis 140

 5.3.5 Optical properties 143

 5.3.6 Plasma diagnosis 145

5.4 Formation mechanism 146

5.5 Post synthesis mixing of SnO₂ and graphene 148

 5.5.1 Overview 148

 5.5.2 Experimental 149

 5.5.3 Surface morphology 150

 5.5.4 Microstructure analysis 151

 5.5.5 Crystal structure analysis 153

5.6 Conclusion 156

References 157

Chapter 6 One-step, *in-situ* binding of tin oxide nanoparticles to graphene nanosheets by in-liquid plasma

6.1 Introduction 159

6.2 Experimental details 161

6.3 Results and discussion 163

 6.3.1 Morphology and elemental distribution 163

 6.3.2 Microstructure analysis 166

Contents

6.3.3 Crystal structure analysis	168
6.3.4 Chemical composition.....	170
6.3.5 Plasma diagnosis	171
6.4 Formation mechanism	172
6.5 Conclusion	174
References	175

Chapter 7 Conclusions and future works

7.1 Summary of this dissertation	177
7.2 Scopes for future works	180

Acknowledgments	182
------------------------------	-----

List of papers	184
-----------------------------	-----

Chapter 1

Introduction

1.1 Materials: Science and synthesis

Historically, one of the fundamental elements in the development of humankind is the field of materials, it is even associated with the name to the ages of civilizations of humankind. The scientific journey of humankind started with the discovery of fire (*plasma?*) and continued, we observed many breakthroughs in this journey, from a discovery of a wheel to the rockets to take humankind to the space, from the smallest chip on electronic devices to the massive structures built on earth, throughout this journey, materials are strangleholds, owing to extensive research, new tools and approaches for research and developed interdependence between scientific research and technical development.

In the last few decades, with industrial advancements and increasing demands, the field of material has expanded. The modern technologies of energy sources, aerospace, semiconductors and the like, are dependent on material science and research. The dependency and demands for materials are increasing day by day. The source of all materials is the earth, the processing of raw materials converts them into use for application development. Innovation in the field of material processing is most necessary. Of course, materials science is limited but has endless possibilities, in a view of future requirements, improvement in the properties of existing materials (functionalization) with various processes as well as finding a new range of materials such as composite, alloys are going to be essential for the continued growth of humankind. Traditional methods are insignificant for the functionalization of the materials and

to tune the properties of the materials as per requirements, along with this, the composite formation and surface modification were complex processes (Fig. 1-1).

The fabrication methods for materials are needed to be revised, since, with advancement in material research, the modern physicochemical material synthesis techniques overcome the high temperature and subsequent high-cost requirement of conventional thermal techniques and now the methods based on non-thermal plasma are starting a revolution for material synthesis by reducing process complexity of physicochemical methods. Non-thermal plasma-based techniques have also impacted the properties of the materials,

Material properties requirement is subject to the field of the possible use of perspective materials. Materials having sound electrical (e.g. conductivity), mechanical (e.g. strength), chemical (e.g. stable or inert), optical properties are always in demand for various applications. Considering a sustainable future and current scenario, fulfillment of the increasing need for energy and environment monitoring should be addressed on a priority with the help of materials.

Materials such as metal oxides, polymers specifically conducting polymers and carbons have proved their wide applicability with extraordinary chemical, physical, electrical and mechanical properties. Detailed study and advancement in these materials will be helpful to solve current problems and also futuristic application development.

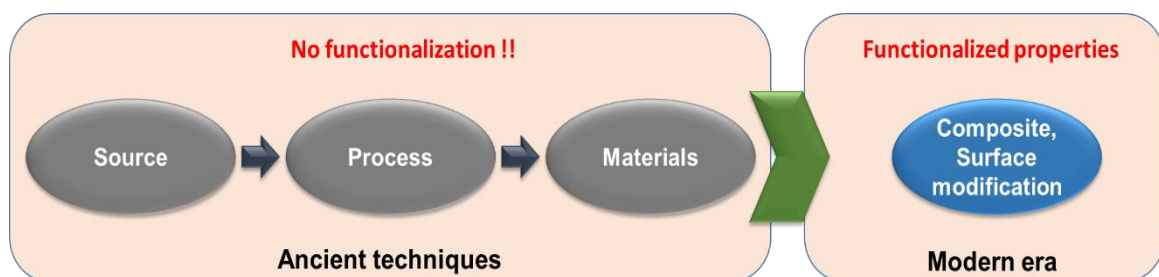


Fig. 1-1 The modern approach for functionalization of materials.

1.1.1 Metal oxides: Tin oxide (SnO_2)

The metal oxides constitute a miscellaneous and intriguing class of materials whose properties cover the entire range from metals to semiconductors and insulators due to different structural geometries and electronic structures. A wide variety in the chemical, physical and electrical properties of metal oxides has made metal oxides exciting material for basic research and technological applications.¹⁾ Semiconducting property of several metal oxides has made them the most useful in electronics and optoelectronics applications.²⁾ Tin oxide also is known as stannic oxide (SnO_2) belongs to this family having high electrical conductivity and optical transparency enabling its use in a wide range of applications.³⁾

SnO_2 has one stable phase having a tetragonal arrangement of the atoms as shown in Fig. 1-2. It is an n-type semiconducting material due to oxygen vacancies acting as electron donors. In SnO_2 , the formation energy of tin interstitial and oxygen vacancies is comparatively low.⁴⁾ The presence of high electrical conductivity and optical transparency of SnO_2 is a result of the wide bandgap (3.6 eV) prohibiting interband transitions as well as adsorption of photons in visible light, oxygen deficiency, and uniform distribution of electron charge density thus high mobility of conduction electrons.⁵⁾ Mutual existence of high conductivity and optical transparency makes SnO_2 differ from other metal oxides.

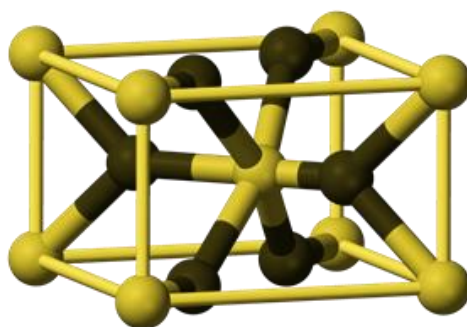


Fig. 1-2 The unit cell of crystalline SnO_2 (black spheres represent oxygen atoms).⁶⁾

The nanostructures of SnO₂ possess great diversity, it is available in the form of nanosheets, nanobelts, nanowires, nano diskettes, and nanorods.⁷⁾ Nanostructures of SnO₂ have a great effect on its applicability for applications such as gas sensing, and catalysis as surface properties of nanostructured tin oxide plays a vital role due to the increased surface to volume ratio.⁸⁾ Thus, it's necessary to study the surface and size-dependent properties of SnO₂.

Materials which have the effect of ambient gas on its physical or chemical properties can be used as gas sensing material. Most of the metal oxides show the changes in their properties as the effect of ambient gas, however, SnO₂ is widely studied material for gas sensing applications owing to its surface sensitive properties. TiO₂, for example, increases its conductivity due to the formation of bulk oxygen vacancies under reducing conditions and thus is categorized as a bulk-sensitive gas sensing material. SnO₂ on the other hand, although bulk defects affect its conductivity, belongs to the category of surface-sensitive materials.⁵⁾ Gas sensors characteristics of SnO₂ are summarized in Table 1-I.⁹⁾ The gas sensing mechanism of SnO₂ is debatable, but basically trapping of electrons at adsorbed molecules and band bending induced by these charged molecules are responsible for a change in conductivity.¹⁰⁾ Gas sensors based on SnO₂ require a high temperature for its operation thus during fabricating sensors based on SnO₂ additional heater assembly is essential. This increases the operation cost of the sensors based on SnO₂. The high-temperature required for operation is due to the absorption of oxygen on SnO₂ surface in air. The adsorbed oxygen species on surface captures electrons, the charge trapping by oxygen species cause the formation of the depletion layer, reducing conductivity. Upon reaction with gases, the electrons are injected resulting increase in conductivity. The oxygen vacancies are important for gas sensing response of SnO₂, the desorption temperature for absorbed oxygen species determines the operation temperature of the SnO₂. The number of free electrons and electron mobility are important for effective gas sensing response of the SnO₂. The porosity and size are also effecting parameters for gas sensors based on SnO₂.¹²⁾

SnO₂ is also considered as a promising anode material in lithium-ion batteries (LIB) due to its high theoretical specific capacity (790 mAh/g), low operating voltage (charge and discharge), and cost among other metal oxides. However, a large volume change during charge

and discharge process has a big impact on its applicability in LIBs. ^{13, 14)} The process can be understood by following chemical reactions.



In the above processes, transformation stated in Eq. 1.1 is the formation of Sn and Li₂O, this is an irreversible process. At the second step, the alloying/dealloying process of Li_xSn occurs. Since the first step is irreversible, the formation of Sn causes the change in volume of SnO₂, leading to pulverization of SnO₂ anode electrodes, a mechanical failure of SnO₂ electrodes.

To overcome the problems with SnO₂, the surface processing, synthesis of different nanostructures and composite formations are necessary.

The synthesis of SnO₂ nanostructures with various morphology and size is possible with synthesis techniques such as sol-gel method (spherical particles of size 20 nm), solvothermal method (spherical particles of size 5 nm), microemulsion method (flower-like of size 8 nm), microwave irradiation method (irregular shape of size 25 nm), laser ablation (nanowire of diameter 20 nm), chemical vapor deposition (spherical particles of size 5 nm), and even biosynthesis methods (spherical particles of size 30 nm), as per requirement. However, these methods need a high temperature to synthesize SnO₂ particles (minimum 150 °C for biosynthesis, maximum 900 °C for laser ablation method). In addition, the above methods are based on multi-step progression requiring multi precursors for synthesis. ^{7, 15, 16)}

Table 1-I Gas sensing characteristics of tin oxide for ethanol, methanol and carbon monoxide.⁹⁾

	Sensor response at 150 ppm (R _a /R _g)	Detection limit (ppm)	Operating temperature (°C)	Response time (sec)	Recovery time (sec)
Ethanol	3.2	3	225	165	170
Methanol	3.5	2	180	140	173
Carbon monoxide	1.3	50	280	120	137

1.1.2 Conducting polymers: Polyaniline (PANI)

Polymers are formed by regular repetition of their respective monomers. Until 1977, the polymers were known to be insulating materials but the discovery of conducting polymers (CPs) gave rise to the entirely new field for material research, owing to the conducting properties they are widely referred as synthetic metals.¹⁷⁾ The conductivity of the CPs is subject to the doping. The polymers are made up of σ - bond, immobile charges. Certain polymers possess π -conjugation along the polymer backbone. The π -conjugation in polymers deliberates the mobility requirement to charges which are created by the doping process.^{18, 19)} The applications based on CPs include batteries, supercapacitors, sensors, and light emitting diodes. There are many conjugated polymers reported as CPs, out of which polyaniline (PANI) has studied widely, PANI is made up of aniline monomer connected to form a backbone of alternating nitrogen and benzene rings. PANI possesses good thermal and environmental stability, which makes it unique from other CPs.²⁰⁾

The PANI takes in four different forms depending on the state of nitrogen atoms. Figure 1-3 shows different structures of PANI. The physical and chemical properties of PANI varies with its structure, the structure variation of PANI is due to the degree of oxidation of the nitrogen atoms. The leucoemeraldine is fully reduced state, emeraldine is half oxidizer state, called as emeraldine base, upon doping this can be converted into emeraldine salt. The permigraniline is fully oxidized state of PANI. The emeraldine salt is a most useful form of PANI. Its stability and high conductivity upon doping make its perfect state of PANI for various application, the properties of PANI can be tuned as required reversibly.^{21, 22)}

Table 1-II Physical properties of structures of PANI.

Name	Conductivity (S cm ⁻¹)	Color
Leucoemeraldine	< 10 ⁻⁵	Yellow
Emeraldine base	< 10 ⁻⁵	Blue
Emeraldine salt	~20	Greenish black
Pernigraniline	< 10 ⁻⁵	Violet

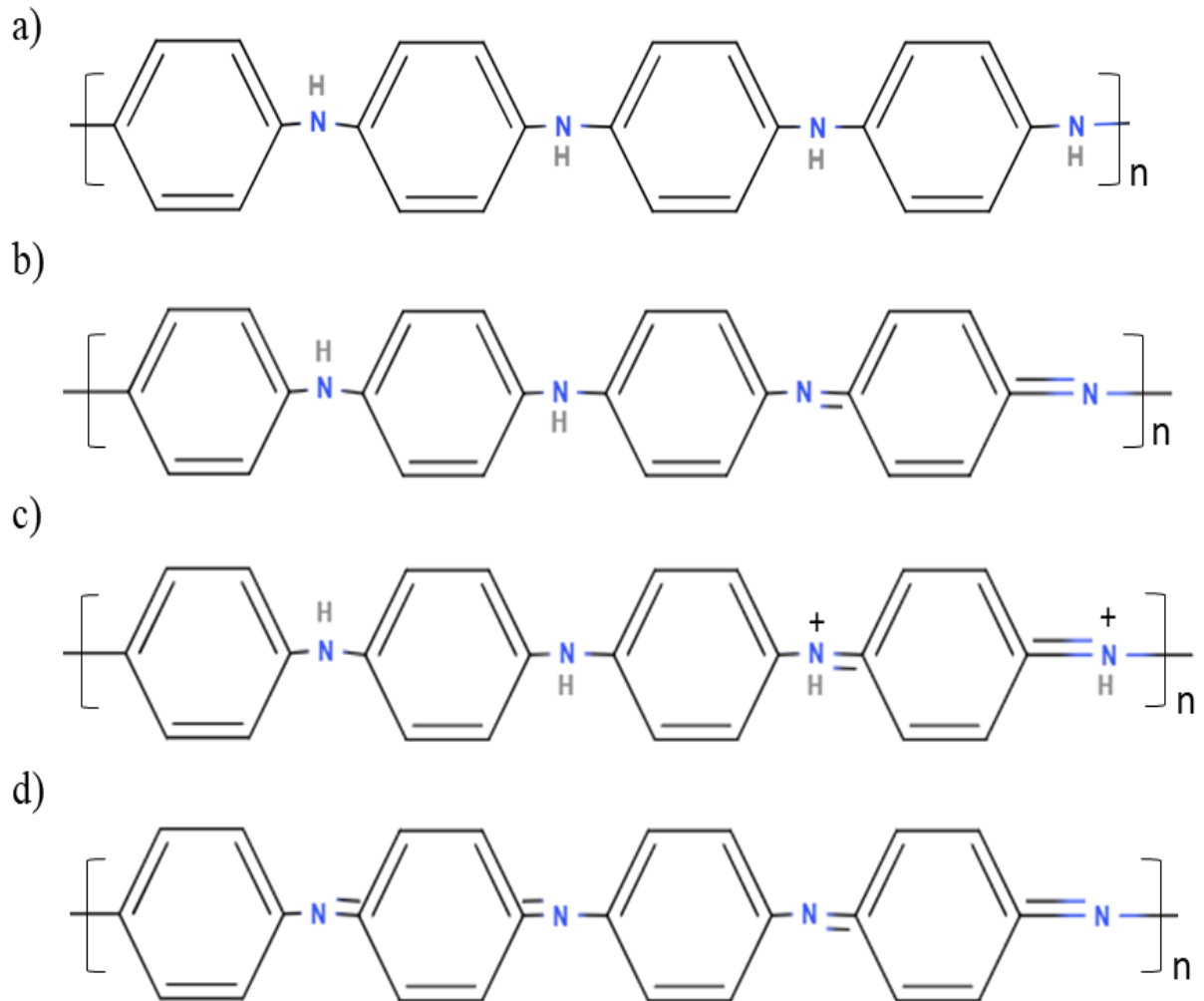


Fig. 1-3 Structures of PANI a) Leucoemeraldine, b) Emeraldine base, c) Emeraldine salt, d) Pernigraniline.

PANI has potential applications in various fields such as tissue engineering, drug delivery, supercapacitors, solar cells, and sensors.²³⁾ PANI has been explored widely for its gas sensing applications owing to its versatile properties such as electrical conductivity, electrochemical properties, and stability. In addition to this, PANI can be synthesized in various shapes giving rise to applicability.

The controlled electrical conductivity with doping level makes PANI suitable material for gas sensing applications. The doping level in the PANI can be altered by introducing gases to be analyzed and transferring or receiving electrons through it. This transfer phenomenon caused a change in electrical conductivity and work function of the PANI.²⁴⁾ Thus, PANI can be effective as chemo-resistive gas sensor and it has been as an effective gas sensing material for ammonia at room temperature. As per previous studies for the ammonia sensing mechanism by researchers, the ammonia sensing of PANI is a result of protonation/deprotonation of PANI.²⁵⁾ The protons on $-NH-$ groups were transferred to NH_3 molecules to form ammonium ions while PANI turned into emeraldine base form. This process is reversible when the desorption of ammonia occurs, PANI goes back to its emeraldine salt form. (Fig. 1-4) In this process, the change in conductivity occurs.

PANI shows the high response to ammonia, PANI based sensors operate at room temperature but long time instability and irreversibility are the major problems of PANI based gas sensors, making use of PANI based composites or nanostructures may help to overcome the drawbacks of the PANI.^{26, 27)}

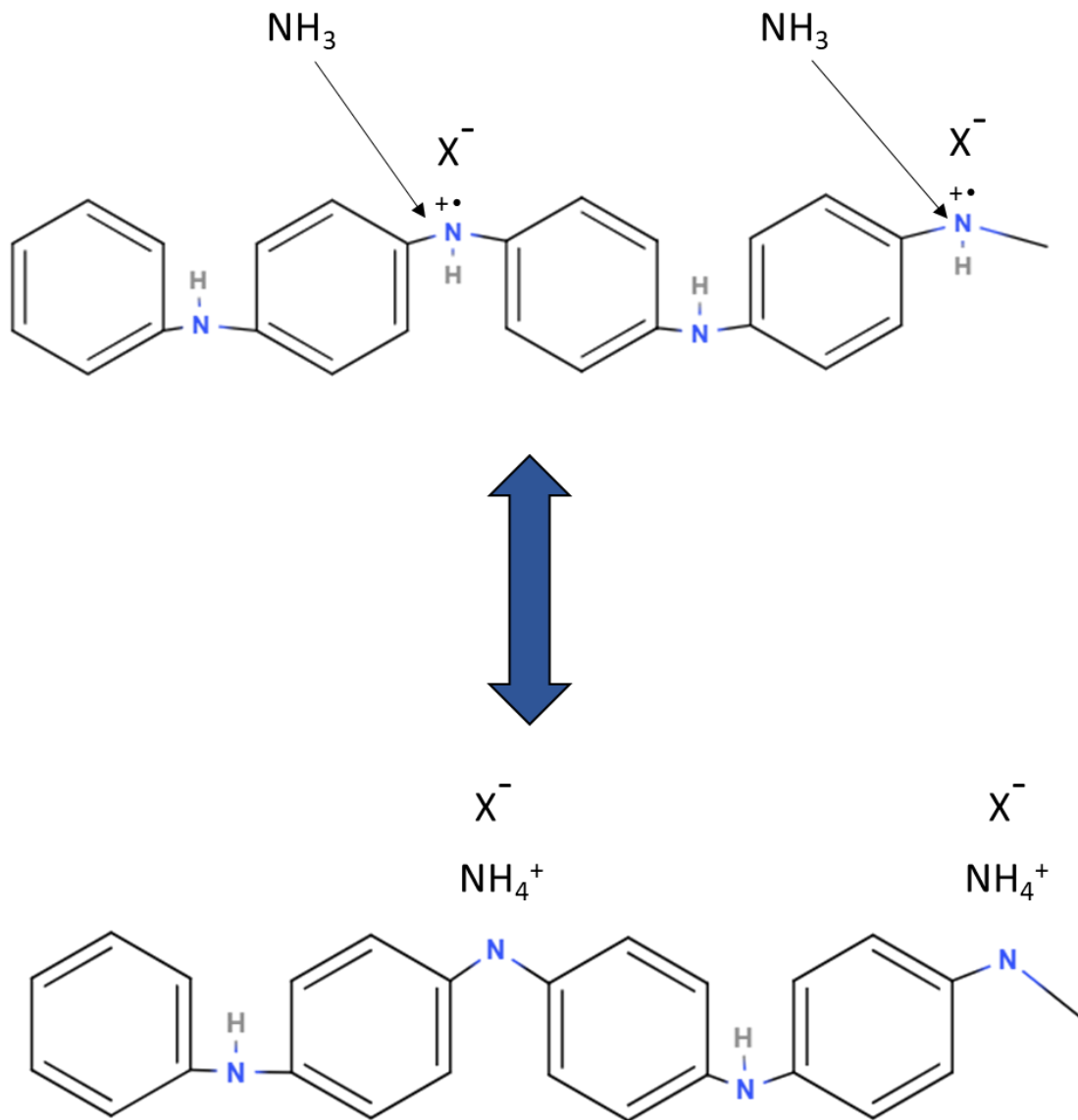


Fig. 1-4 Ammonia response mechanism of PANI in a reversible process.²⁷⁾

1.1.3 Carbon materials

Carbon materials are the most versatile materials, present in various allotropes. The great diversity in structural, chemical and physical properties of carbon-based materials come from their bonding structure.

Carbon has three types of hybridizations, sp , sp^2 , and sp^3 . The carbon atom has 4 valence electrons, 2 electrons in the 2s orbital, and other 2 electrons occupy one 2p orbital each. All four valence electrons of carbon actively take part in bonding. In sp^3 hybridization, the 2s orbital and three 2p orbitals of carbon are hybridized to form four equivalent sp^3 hybrid orbitals of equivalent energies, one electron occupying each hybridized orbital. These four orbitals can form strong C–C σ bonds when the sp^3 orbitals of adjacent carbon atoms overlap. In sp^2 hybridization, three electrons occupy three equivalent sp^2 hybridized orbitals with the 2s orbital and two 2p orbitals taking part in hybridization. During bonding, the sp^2 orbitals form strong σ bonds, whereas the p orbital forms a comparably weaker p bond via a side-to-side overlap with another π orbital on the adjacent atom, causing the π electrons to be delocalized between the two adjacent atoms. The sp^2 bonding in carbon is typically depicted as a C=C double bond, where the double bond consists of one σ bond and one π bond. The sp bonding in carbon follows a similar trend, forming two equivalent sp hybridized orbitals with higher σ bond energy and two π orbitals with lower p bond energy, resulting in a C \equiv C triple bond. ²⁸⁾

The ratio of sp^2 to sp^3 determines the properties of carbon materials. This ratio depends on the deposition conditions and post-deposition treatments of carbon materials. Materials composed of 100 sp^3 bonds are diamond material, known for hardness and wide optical band gap. Graphite is an example of 100 % sp^2 bonded carbon material recognized for its exceptional conducting behavior. Another type of carbon materials is mixed bonded materials, such as amorphous and nanocrystalline carbons, they have mixed properties from diamond and graphite materials, this includes electrical conductive to insulating, hard to soft and from optically transparent to opaque, depending on the ratio of sp^2 to sp^3 . Figure 1-5 is a ternary phase diagram for the carbon materials based on bonding. ²⁹⁾

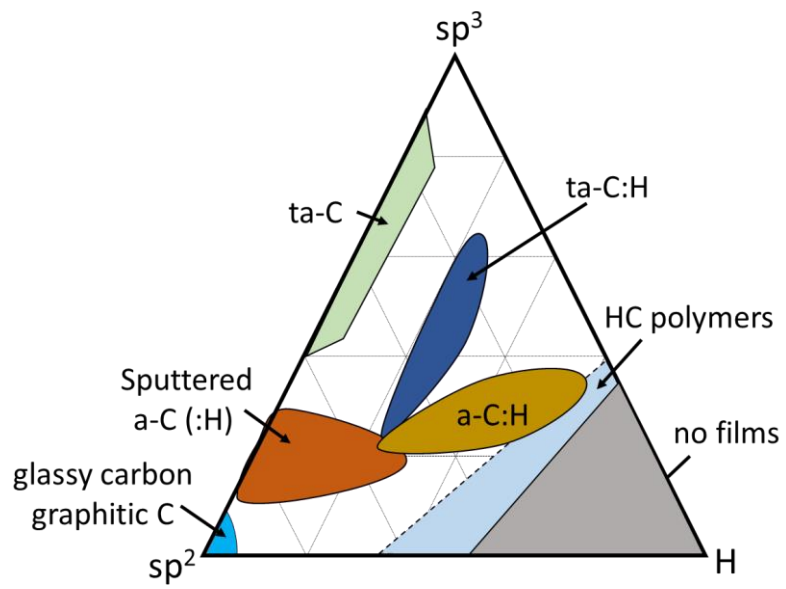


Fig. 1-5 Ternary phase diagram for the classification of carbon materials. ²⁹⁾

Carbon nanomaterials possess a unique place in an area of material science and research due to their exceptional chemical, electrical, mechanical and thermal properties and are being used and researched for various applications ranging from sensors, supercapacitors, fuel cells, and drug delivery. The era of carbon nanomaterials started with the discovery of fullerene in mid-eighties, followed by the discovery of carbon nanotubes. The major breakthrough of carbon nanomaterial-related research was the discovery of graphene.³⁰⁻³³⁾ Figure 1-6 shows structures of carbon nanomaterials discussed here.

Fullerene zero-dimensional carbon material having a spherical shape composed of sixty carbon atoms, consisting of 60 carbon atoms involving 12 membered 5 rings and 20 six-membered rings. Although fullerene is available in different range symmetries, the C₆₀ is the most dominant and stable one and hence widely studied. Fullerenes have photosensitive, electron-accepting-transporting with other attractive physical and chemical properties, leading use of fullerenes in various areas such as photovoltaics, catalysis, medicinal chemistry, and biological applications.³⁴⁾

Carbon nanotubes (CNTs) are one-dimensional carbon materials having a co-axial tubular shape. CNTs have six-membered ring structures discovered by Iijima et al in 1991.³³⁾ CNTs have a high length to diameter ratio, the diameters of CNTs is from few to hundred nanometers. CNTs possess superior mechanical, electrical, and thermal properties. CNTs are widely in use for energy, and sensing applications.³⁵⁾

Graphene is a two-dimensional monolayer of carbon atoms. Graphene has a honeycomb lattice formed by a strong covalent sp² bond. By the hybridization of orbitals of p orbit and s orbit, the sp² hybrid bonds form three angles 120° with each other in one plane. A single layer of graphene of thickness 0.34 nm was peeled off from graphite by a simple exfoliation of graphite.³²⁾ Graphene, being a two dimensional one atom thick sheet of carbon possess extraordinary properties. It is clearly different from other carbon nanomaterials and can be called as a parent of nanocarbon materials.³⁶⁾ Graphene possesses distinctive properties such as large surface area (2,630 m²g⁻¹), chemically stability, high charge carrier mobility (250,000 cm² V⁻¹), excellent thermal conductivity (5,000 W m⁻¹ K⁻¹) and high electrical conductivity

($6,000 \text{ S cm}^{-1}$), but graphene has almost zero optical band gap (optical transmittance $\sim 97.7 \%$). The excellent properties of graphene make it an ideal material for next-generation devices.³⁷⁾

Traditionally, graphene has been synthesized by several methods, these methods broadly can be categorized into two approaches: the bottom-up approach and the top-down approach. The bottom-up approach includes pyrolysis method, epitaxial growth, and chemical vapor deposition (thermal and plasma) and the top-down approach includes methods based on exfoliation (mechanical, chemical) and chemical synthesis, summarized in Fig. 1-7.³⁸⁻⁴⁰⁾ The bottom-up approach methods are useful to synthesize high crystalline graphene but require vacuum systems, a cost and time assisted with vacuum systems are of prime concerns. In addition to this, bottom-up methods yield a low quantity of graphene. The top-down approach methods are widely used by researchers to yield a high quantity of graphene at a relatively low cost but these methods have problems with the low crystallinity/quality and multistep processing of graphene.^{41, 42)}

The traditional graphene methods are not the best methods for graphene synthesis, as there is a trade-off relationship between synthesis amount and quality of synthesized graphene.

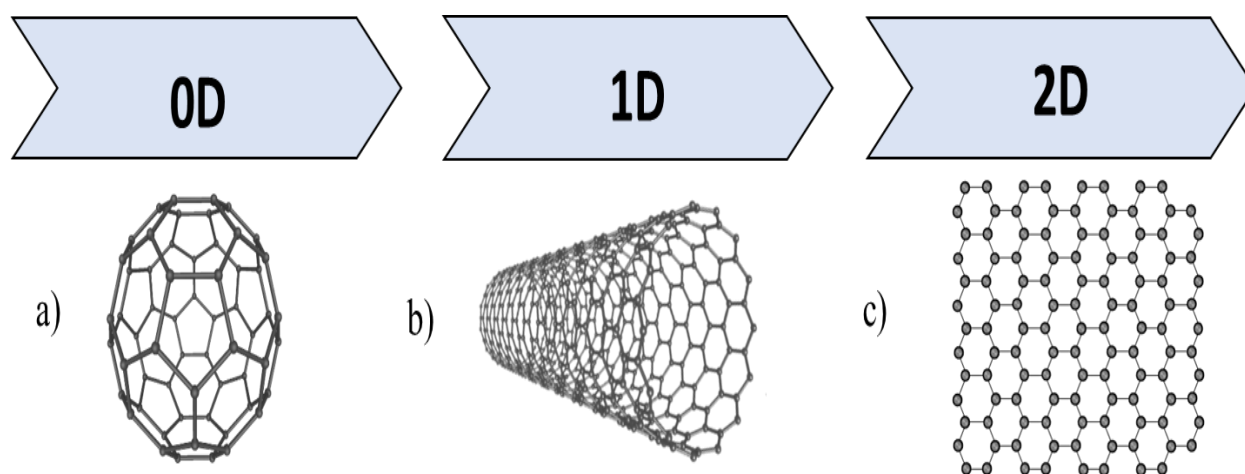


Fig. 1-6. Carbon nanomaterials as per dimensions a) 0D – Fullerene, b) 1D – Carbon nanotube, and c) 2D – Graphene.

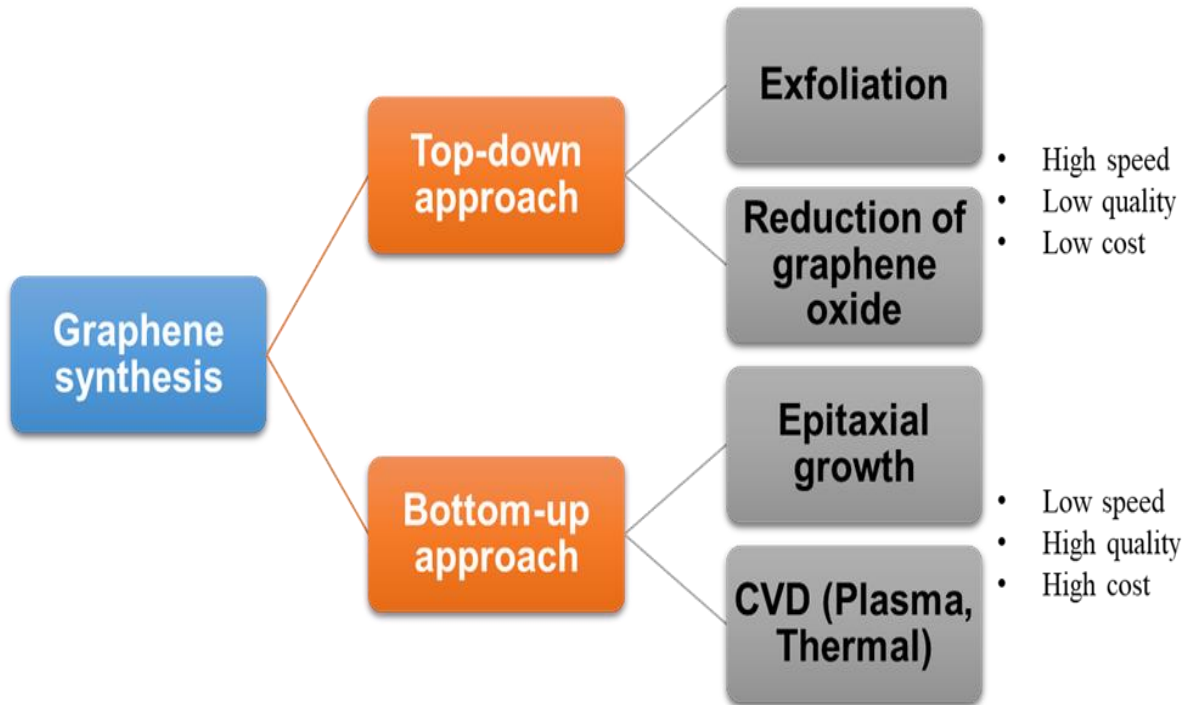


Fig. 1-7 Classification of graphene synthesis methods.

1.2 Material functionalization: Composites

Composite can be simply defined as a material formed by combining two or more materials to alter/modify the properties of constituent materials or to have unique properties by combinations due to synergetic effect. Composites are not fully manmade, even some natural things are present in the form of the composite such as wood, formed by a cellulose fiber and weaker substance lignin, making it stronger material. Cellulose and lignin, both are weak materials but together they form a stronger material. Use of composite and research in the field of composite has increased exponentially mostly due to the requirements of special properties and after understanding limitations of single component materials, for example, for aerospace applications, high strength to weight ratio, high corrosion, and temperature resistance are important requirements from material properties, traditional materials cannot fulfill all the requirements. Nowadays, composites are the prime part of aerospace, automobile and other manufacturing industries replacing traditional single component materials.

With technological advancements and increasing demands, a need for new composite materials has been observed and thus wide research has been carried out on the composite materials focusing on composite fabrication methods, controlling properties for specific applications, and mechanism behind special properties.

Laboratory synthesis methods of the composite can be realized in two different approaches, *ex-situ* approach, and *in-situ* approach. In *ex-situ* approach, presynthesized constituent materials are bind together by means of some physical processes (grinding, mixing) to get a composite and in the case of *in-situ* methods, synthesis of composite carried out by using precursors of constituent materials followed by chemical processes to get a composite material. Both approaches have some advantages and disadvantages, but in comparison, the *in-situ* approach offers better composite material properties over *ex-situ* approach. Numerous composites have been proposed by researchers such as composites based on metal oxides-polymers, metal-oxide-metal, metals-polymers, polymer-carbon and metal oxide-carbon for their potential applications in various fields.

1.2.1 Tin oxide - Polyaniline composite (Sn-PANI)

Composites based on metal oxide and polymers have been studied widely mainly for gas sensing applications to overcome the drawbacks such as high operating temperature requirement of metal oxide based sensors, and irreversibility of polymer-based sensors.⁴³⁻⁴⁵⁾

(i) Composite synthesis

The synthesis methods for SnO₂-polyaniline composite have been achieved by *ex-situ* and *in-situ* methods.⁴⁶⁻⁴⁹⁾ PANI being a conducting polymer, its electrical conductivity is sensitive to the dopants, increase in conductivity of PANI has observed as an effect of SnO₂ addition by researchers.⁵⁰⁾

(ii) Composite properties

The gas response studies of Sn-PANI composite revealed that the sensor performance in terms of sensitivity, operational temperature requirements, selectivity, response time and recovery time can be improved. Though metal oxides need a high temperature for their operation, however, when combined with PANI, it was observed that the sensor based on Sn-PANI can operate at room temperature.⁵¹⁾

As observed by L. Yang et al., the sensor composed of Sn-PANI composite had a high surface to volume ratio compared to constituent materials, which provides more adsorption sites for the sensing and facilitates the adsorption and diffusion of the target gas molecules, thus leading to enhanced the response and accelerated the response and recovery.⁵²⁾ It has been reported that p-type PANI and n-type SnO₂ forms p/n heterojunction in Sn-PANI composite. The formation of p/n heterojunction results in efficient charge movement at the interface and reduced activation energy and enthalpy for adsorption of gases.⁵²⁻⁵⁵⁾ Similar trends of improvement in an ammonia gas sensing properties has observed by N. Deshpande et. al as an effect of SnO₂ incorporation in PANI to form Sn-PANI composite.⁴⁷⁾ They proposed that when Sn-PANI composite get exposed to ammonia, which permeated into PANI matrix freely, some of the NH₃ molecules might reach into the depletion region, which is surrounding the SnO₂ crystallite and act as a dielectric between the PANI and SnO₂ border. The depletion region field might polarize the ammonia molecules, and in turn provide a positive charge to PANI

molecules, which can become mobile on its transfer to the central N atom of PANI molecule. So in all this process creates some free holes on PANI molecules, which increase the hopping conductivity of the film, and therefore make the composite film relatively more conducting electrically as stated by N. Deshpande et. al.

Most of the researchers studied *in-situ* methods for gas sensing applications, it will be interesting to check gas sensing response of Sn-PANI composite fabricated by *ex-situ* methods as *ex-situ* methods are relatively easy and low-cost methods.

1.2.2 Tin oxide-Graphene composite

As a 2D material, graphene not only provides a material platform to explore the physics and developing applications based on 2D materials but also acts as a building block to construct material assemblies and integrated devices from the bottom up.⁵⁶⁾

(i) Composite synthesis

In the last few years, wide researches have been devoted to exploring the synthesis methods and applications of tin oxide-graphene (SnO_2 -graphene) composite. It has proved its applicability for various applications such as supercapacitors, lithium-ion batteries, gas sensing, photocatalysis, and water purification.⁵⁷⁻⁶²⁾ In spite of its applicability for various applications, the big issue research community has been facing is the synthesis of SnO_2 -graphene composite, mainly due to the synthesis methods for the graphene.

The synthesis approach for SnO_2 -graphene composite is highly graphene synthesis oriented as SnO_2 can be synthesized by simple chemical routes at atmospheric pressure and relatively low temperature as compared to the graphene. The synthesis approach for SnO_2 -graphene composite or binding of SnO_2 to graphene can be realized in two ways: *ex-situ* binding or *in-situ* binding (Fig. 1-8). *Ex-situ* binding involves mixing of presynthesized SnO_2 and graphene, in some cases, the graphene has been functionalized by non-covalent π - π stacking or covalent C-C coupling prior to mixing to enhance the processability of the composite.⁶³⁾ The graphene used in these methods is often synthesized by traditional graphene synthesis methods, these methods (CVD, epitaxial growth) need a low pressure and high temperature to yield the high-quality graphene which increases the cost, the common method of graphene synthesis for SnO_2 -graphene composite is modified Hummer's method, offering high yield but low-quality graphene. The *ex-situ* binding methods for SnO_2 -graphene composite are easy but have serious issues with distribution of SnO_2 particles on graphene sheets.⁶⁴⁾

On the other hand, the *in-situ* methods for SnO_2 -graphene composite have extensively studied as these methods do not have problems with the distribution of SnO_2 particles on graphene sheets and can offer control over size, the shape of SnO_2 particles, composite

assembly and the overall process of composite formation (Fig. 1-9). *In-situ* binding methods involves simultaneous reduction of graphite oxide (GO) and tin chloride (SnCl_2 or SnCl_4), the reduction of GO is carried out by modified Hummer's method, which yields graphene at atmospheric pressure and doesn't need high temperature, however, multi-step processing and quality of graphene were the major issues. ⁶⁵⁻⁶⁷⁾

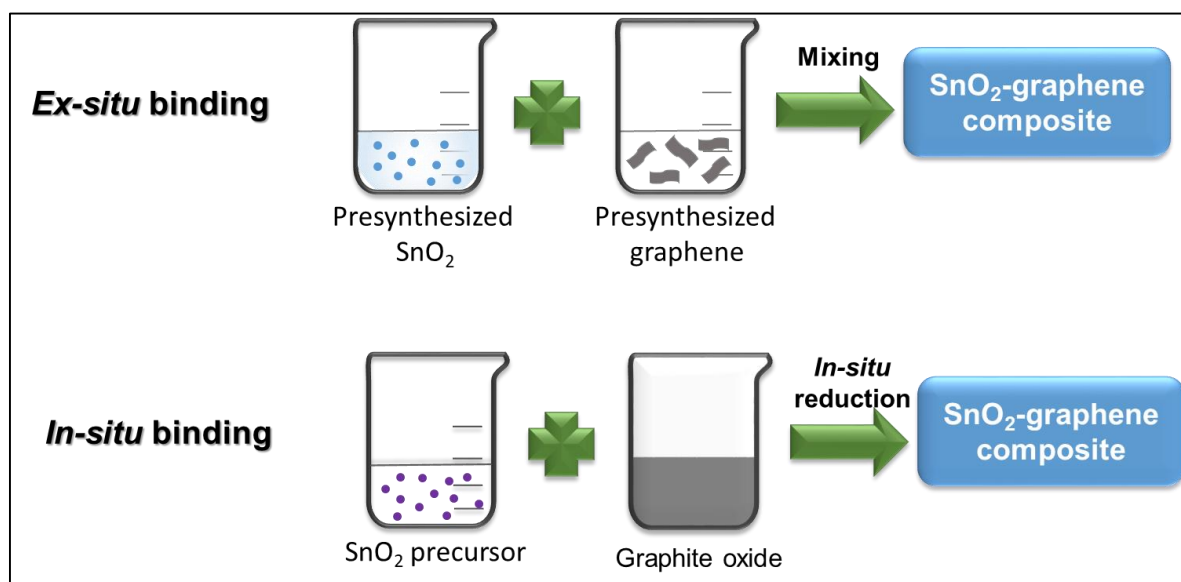


Fig. 1-8 Approaches for binding of SnO_2 -graphene composite. ⁶³⁾

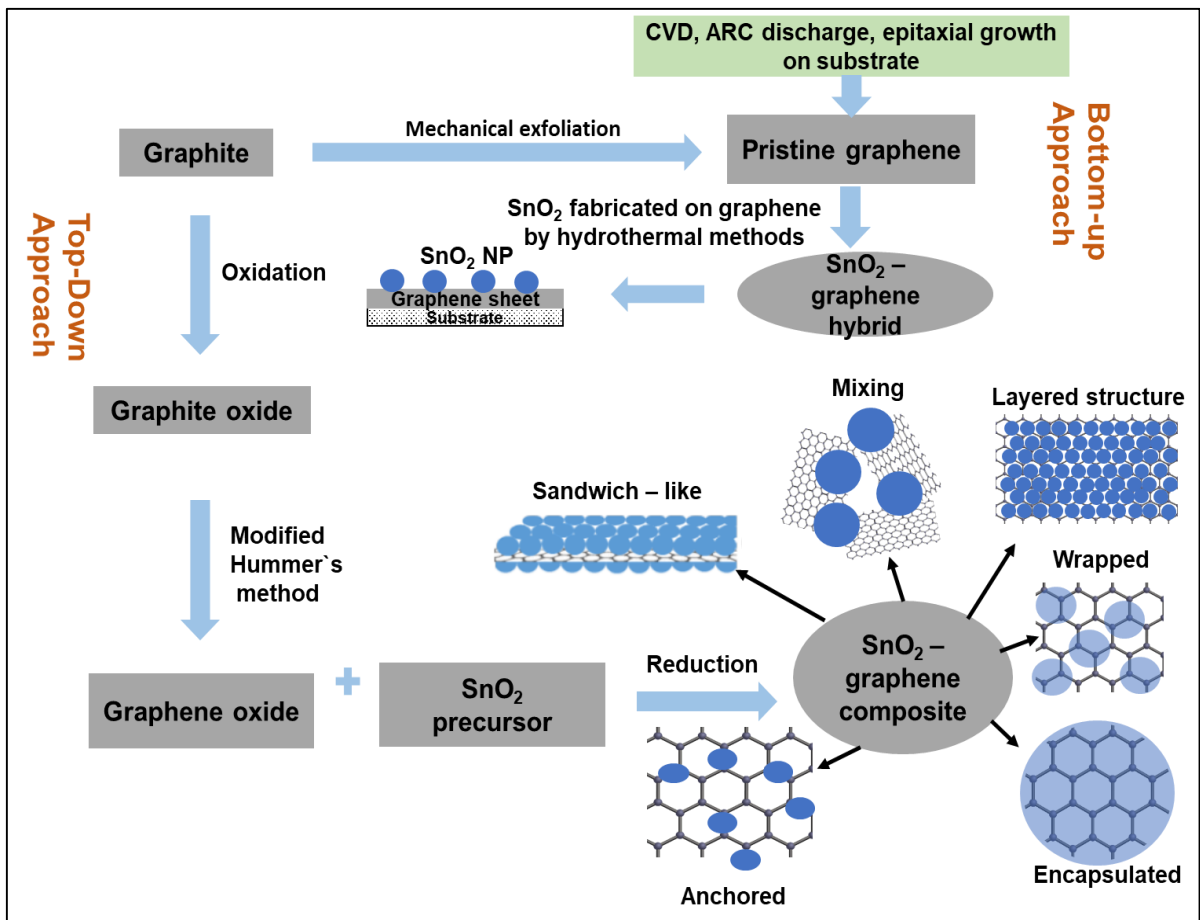


Fig. 1-9 Different structural assemblies of SnO₂-graphene composite with respect to the graphene synthesis approach. ⁶⁵⁾

(ii) Composite properties

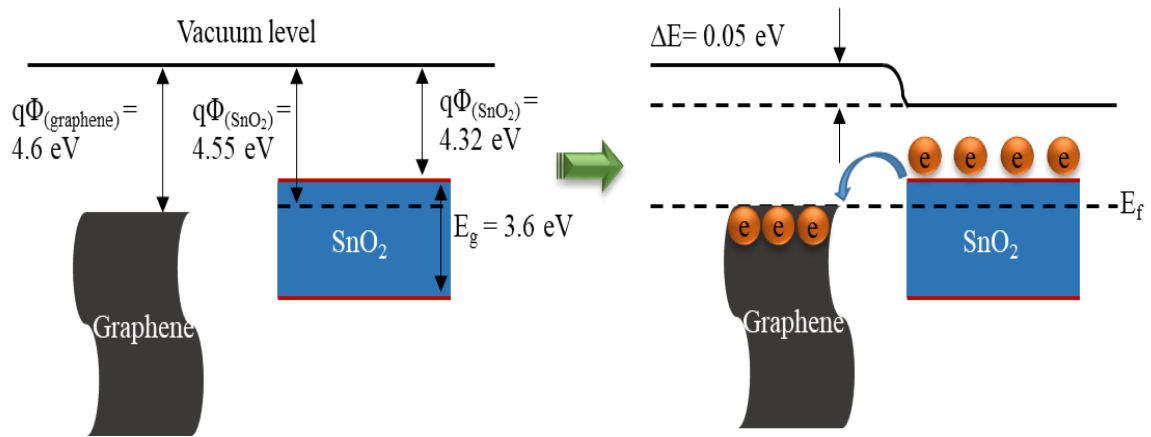
J. Liang et. al studied the formation of SnO₂-graphene composite by *in-situ* approach for anode material for Li-Ion battery application, using modified Hummer's method and *in-situ* synthesis of SnO₂.⁶⁸⁾ In another study by A. Dhanabalan et. al for anode material for Li-Ion battery application, the synthesis was carried out by mixing SnO₂ precursors with presynthesized graphene followed by *in-situ* binding of SnO₂ binding.⁶⁹⁾ In the case of SnO₂ anodes in Li-ion batteries pulverization of SnO₂ is a big issue leading to loss of electrical contact and thus poor cycle performance. Graphene has a high theoretical capacity of 744 mAh g⁻¹ as an anode material, however, agglomeration and re-stacking minimize its performance. Above researchers found out that the SnO₂-graphene composite can overcome the problems of SnO₂ and graphene, this is due to the high specific area of graphene acted as an additional accessible area for electrolyte ions, and adsorption of Li⁺ ions on its surface resulting in better charge transfer kinetics, on the other hand, incorporation of SnO₂ prevented restacking and agglomeration of graphene. Since the graphene acted as a barrier to avoid the aggregation of SnO₂ and a buffer to prevent the volume expansion of SnO₂. In a review studies by Y. Deng et. al, it was reported that the small size of SnO₂ nanoparticles in SnO₂-graphene also contribute for the better outcomes.⁷⁰⁾

Next, the applicability of SnO₂-graphene composite as a gas sensing material has been studied comprehensively in order to overcome problems with gas sensors based on pure SnO₂ such as high operating temperature, low selectivity. Graphene's high specific surface area, exceptional conductivity, and high carrier mobility are the ideal properties to be gas sensing material but large-scale production, no optical band gap, and unavailability of functional groups in intrinsic graphene are issues.⁷¹⁾ F. Meng et. al studied the SnO₂-graphene composite to response at parts per billion (ppb) level concentration of benzene which was 200-fold lower than SnO₂ based benzene sensor (1 ppm), attributed to increasing in absorption sites due to the incorporation of graphene.⁷²⁾ The adsorption of benzene is analogous to mend the π -conjugate system of graphene, which may provide more active sites. The synthesis process was based on *in-situ* approach. Z. Abideen et. al investigated the gas sensing response of SnO₂-graphene to various gases (C₆H₆, C₇H₈, CO, CO₂, and H₂S), synthesizing composite by *in-situ* loading SnO₂

particles on graphene and observed improved sensing performance as a result of composite formation. The reason behind improved sensing performance was accredited to the formation of a heterojunction between p-type graphene and n-type SnO₂. In the heterojunctions, the work functions of SnO₂ and graphene are 4.55 and 4.60 eV, respectively and the Fermi energy of SnO₂ is lower than that of graphene. According to the study, upon the generation of graphene/SnO₂ heterointerfaces, electrons will flow from SnO₂ to graphene, ultimately equilibrating the Fermi level. This charge transfer will form a potential barrier at the heterojunctions, causing the vacuum energy level and the energy band to bend. As a first possibility, the initial transfer of electrons from SnO₂ to graphene will develop a surface depletion region on the SnO₂ surface. As the initial resistance increases, the same change in resistance upon introduction/removal of a target gas will lead to higher sensitivity. As a second possibility, the electrical current across the SnO₂/graphene interfaces will provide an additional change in the resistance. The reducing gases and oxidizing gases will react with adsorbed oxygen, which provides and remove electrons, respectively.⁷³⁾ Similar improved sensing characteristics of SnO₂-graphene have observed by other researchers also, however, in spite of improved characteristics, the traditional synthesis methods for the composite were complex mainly due to problems associated with graphene synthesis.⁷⁴⁻⁷⁵⁾

The applications of SnO₂-graphene based composite are not limited to the above-discussed topics only, it is necessary to investigate the possible applications of SnO₂-graphene composite and mechanism associated with it to tune it for the best outcome. However, decreasing process complexity in the synthesis of SnO₂-graphene composite is need of an hour.

a)



b)

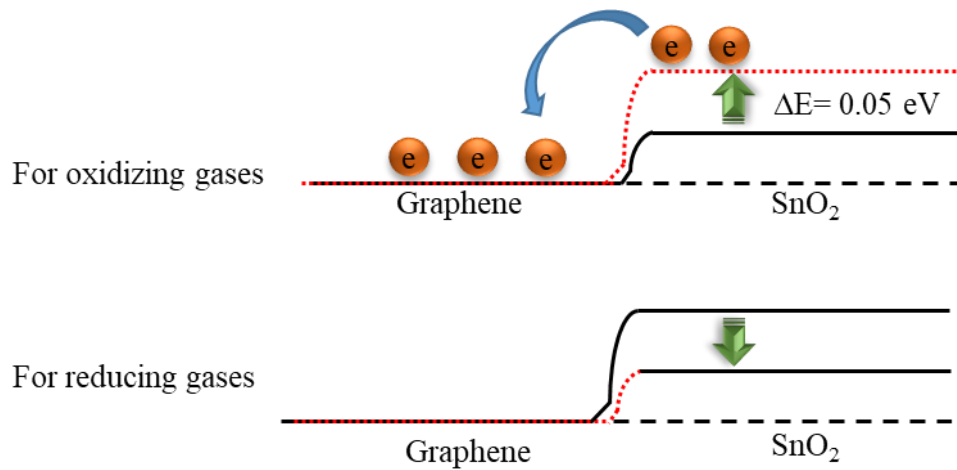


Fig. 1-10 Schematic illustration of a) heterojunction between graphene and tin oxide, b) gas sensing response of graphene-tin oxide composite for oxidizing and reducing gases.⁷³⁾

1.3 Plasma processing

A plasma can be defined as partially or fully ionized gas containing electrons, ions, and neutral atoms and or molecules. The plasma processing is a plasma-based material processing technology that aims at modifying the chemical and physical properties of a surface, however, with years of research and studies, it hasn't been limited to the surface processing, expanding its field to nanomaterial synthesis, waste treatment and even bioprocesses utilizing interactions of plasma constituents with solids, liquids, and gases. Figure 1-11 gives insights of broadened areas of atmospheric pressure plasma processing and advantages of plasma processing.

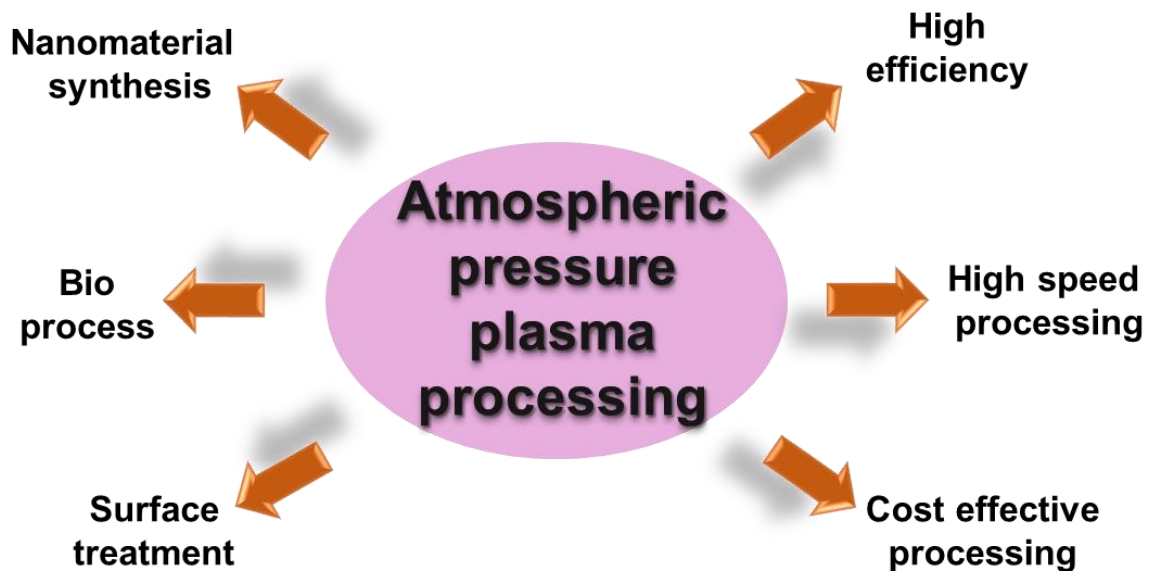


Fig. 1-11 Atmospheric pressure plasma processes and advantages.

1.3.1 Atmospheric pressure plasma surface treatment

In last few years, the atmospheric pressure plasma (APP) has gained a lot of interest from researchers and industry for surface treatment due to easy operation, process simplicity, low cost as compared to low-pressure plasma and applicability for surface treatment of almost all materials. The APP can be driven at ambient air and the temperature is almost a room temperature, the highly reactive process is given because the electron temperature is high nevertheless the low gas temperature. ⁷⁶⁾

The APP induces several distinctive reactions and the mechanism of these reactions has not understood fully. However, it is well known that the APP produces several reactive species when APP generated at ambient air. In addition to this, various wavelength lights are also emitted from molecules, or atoms excited as an effect of APP, especially, 10-400 nm of wavelength light ultraviolet/vacuum ultraviolet gives very high energy to an irradiation material and results into excitation, ionization, and dissociation. The APP can also be called as non-equilibrium plasma as it contains relatively high energized electrons compared to the gas temperature ($T_e \gg T_g$). Several factors are crucial in the case of APP surface treatment, such as the distance between APP source and material, as reactive species generated in the APP has a limit over transmission distance. Short lifetime species such as electrons, VUV, and reactive chemical species cannot travel a longer distance, thus material to the APP distance is important.

The effect of APP on the material surface morphological and chemical properties has studied comprehensively and found that the APP can modify surface morphology and surface chemistry effectively. Y. Kusano et. al studied the effect of the APP on glassy carbon and improved the adhesion of glassy carbon films. ⁷⁷⁾ In another study, the surface roughness was increased by M. Costa et. al by the APP treatment. ⁷⁸⁾ H. Watanabe et. al extensively researched the APP treatment to modify surface properties of carbon nanowalls (CNWs) and found that hydrophobic and hydrophilic properties of CNW surface can be controlled effectively by APP treatment. ⁷⁹⁾

1.3.2 In-liquid plasma for nanomaterial synthesis

Vast researches in the field of atmospheric pressure plasma (APP) have opened doors of numerous applications based on APP, the in-liquid plasma-based material synthesis is one of them. The in-liquid plasma nanomaterial synthesis method is based on the non-equilibrium chemistry offered by the plasma-liquid interaction. This technique can be used to synthesize metal nanoparticles, alloys, metal oxide nanoparticles, carbon materials, and composite materials.⁸⁰⁾

As stated by D. Mariotti et. al, the low-temperature plasma limits the agglomeration and enables the formation of crystalline nanomaterials by selective heating.⁸¹⁾ The mechanism of nanomaterial formation consists of several steps, at first, due to plasma discharge, precursor material undergoes rapid reduction without external reducing agents followed by nucleation and finally formation of nanoparticles. The reduction of precursors might be due to the energized radicals, and ions present in the plasma. Besides this, numerous physical and chemical processes at the gas phase, liquid phase, and gas-liquid interface play a role in nanomaterial formation.⁸²⁾ However, the exact mechanism behind nanomaterial synthesis using in-liquid plasma is still unclear. The plasma parameters have to evaluate to control the size and shape of synthesized nanoparticles along with the synthesis conditions.⁸³⁾

The in-liquid plasma process for nanomaterial synthesis is simple, operated at normal temperature and pressure, thus can be utilized for rapid nanomaterial synthesis. The non-equilibrium chemistry offered by plasma has a big role in this material synthesis process, in a conventional process, molecules get enough energy for reaction by colliding with other particles or with walls but in non-equilibrium plasma, necessary energy is supplied by photons or electrons generated in the plasma.

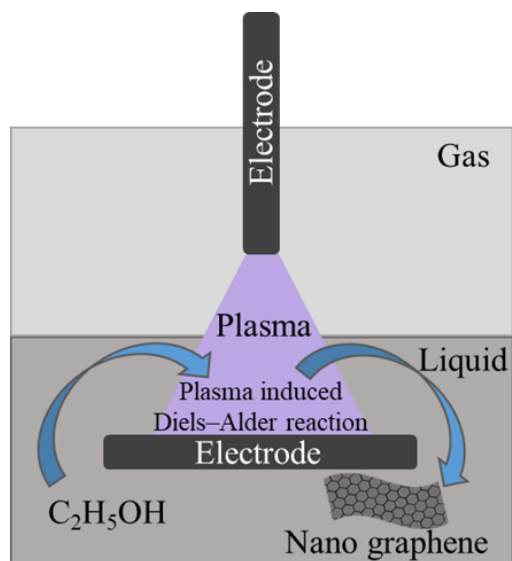
A pioneering study by Hagino et. al showed that the in-liquid plasma nanomaterial synthesis method can be used for graphene synthesis using alcohol as a single precursor at atmospheric pressure without providing external heat.⁸⁴⁾ It was also reported that the graphene synthesized by in-liquid plasma has a high synthesis rate compared to other conventional methods. The in-liquid plasma method yielded high crystalline graphene. The experimental assembly was simple as shown in Fig. 1-12, two electrodes were positioned to form a sandwich between gas and the liquid phase. As shown in Fig. 1-12 (a), one electrode was placed in a gas phase (Ar gas) while other submerged in liquid (ethanol). The plasma was generated in between two electrodes making it 3 phase plasma (gas phase, liquid phase, and gas-liquid interface phase). The three-phase plasma generation provided rich plasma chemistry, high energy electrons generated atomic species in a gas phase and radical generation from the liquid phase (from alcohol). The reaction between the gas phase generated species and liquid phase generated radical from alcohol gave products in the non-equilibrium state. The reaction was found to be plasma induced Diels-Alder reaction as stated by Hagino et. al. Figure 1-12 (b) shows the formation mechanism of graphene based on the GC-MS analysis of residual liquid.

T. Amano et. al. extensively studied the tradeoff relationship between synthesis rate, the crystallinity of graphene, type of alcohol, and type of electrode, and found that lower molecular weight alcohols synthesize high crystalline graphene when combined with graphite electrode, however, a rate of synthesis found to be lower in that case.⁸⁵⁾

In another study, as reported from A. Ando et. al, hydrocarbons (n-hexane and benzene) can synthesize graphene at higher synthesis rate than alcohols due to easy graphitization of long-carbon chain alcohols in in-liquid plasma. However, hydrocarbons also yielded amorphous carbons and graphite-like structures along with graphene.⁸⁶⁾

In summary, the in-liquid plasma method for graphene synthesis offers high-quality graphene synthesis at atmospheric pressure, relatively low temperature with the high rate of synthesis compared to conventional graphene synthesis methods.

a)



b)

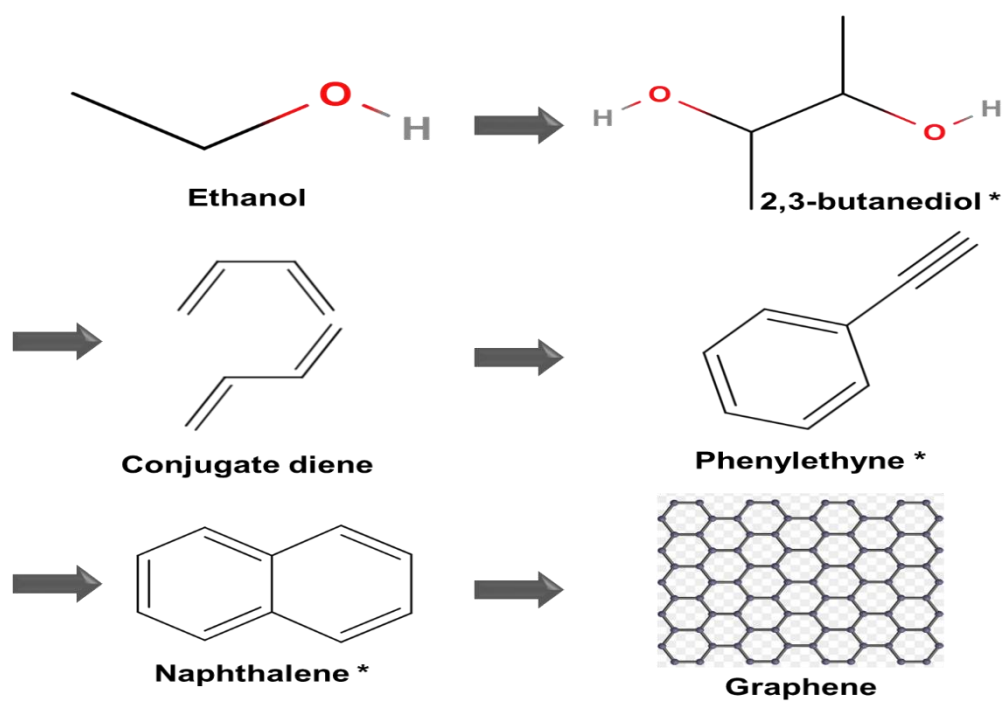


Fig. 1-12 a) In-liquid plasma for graphene synthesis, b) Synthesis model based on GC-MS study of residual liquid. ⁸⁴⁾

1.4 Objectives and composition of this dissertation

To overcome the drawbacks and to make use of beneficial properties of materials efficiently, much attention has to provide for surface modification and composite formation of the materials. The composite materials have versatility in the properties and their properties can be tuned as per requirements. The composites of SnO₂-PANI, and SnO₂-graphene have been of great interest due to the synergetic effect and the wide range of applications such as gas sensing materials, Li-ion batteries, fuel cells, supercapacitors, and electrochemical sensors, thus its necessary to find easiest synthesis method for these composite, along with this, the evaluation of different approaches for composite synthesis is also important.

The plasma processes offer numerous benefits in material processing such as fast, cost-effective and efficient processing. The in-liquid method for material synthesis has more advantageous than any other material synthesis processes. Nanographene synthesized by in-liquid plasmas can be synthesized at a high speed and has high crystallinity. If the in-liquid plasma method can be applied to the SnO₂-graphene composite formation, it can synthesize composites at low cost and easily. The APP surface treatment contributes to control/alter surface structural properties effectively thus it was thought that the plasma processes can be employed effectively for surface modifications and tuning material properties for desired applications. The surface structure and chemical properties of the carbon films are crucial for gas sensing applications. Surface roughness has a vital role in the improvement of gas sensing characteristics of carbon films, the increase in surface roughness can contribute towards an increase in overall surface area for gas adsorption for better sensitivity.

The structures and properties of SnO₂, polyaniline, and carbon materials are described in Section 1.1 along with the advantages and disadvantages of these materials. In Section 1.2, the definition of composites and their formation approaches have explained. The author emphasizes the superiority of composites over component materials. In addition to this, the problems with current composite formations approaches have been discussed. Section 1.3 describes the plasma processes for material syntheses and surface modifications. The applicability of the in-liquid plasma method has been discussed in details.

In Chapter 2, various material synthesis and evaluation methods are described. The plasma diagnosis tools are also discussed.

In Chapter 3, an *ex-situ* approach for the formation of SnO₂-polyaniline (Sn-PANI) composite and its gas sensing response are discussed. The Sn-PANI composite was synthesized by blending materials together and their ammonia and humidity sensing response have shown. The Sn-PANI composite has shown the better gas sensing response than PANI based sensors. A study of surface morphology, crystal structure and chemical composition of Sn-PANI composite was carried out to check the applicability of the *ex-situ* method for Sn-PANI composite synthesis.

In Chapter 4, the modification of surface and bulk properties of carbon films has shown. An effect of deposition conditions on the surface and bulk properties of magnetron sputtered carbon films have been discussed. The changes in the properties were monitored by morphological, microstructural observations. The effects of deposition conditions on optical and electrical properties of carbon films have been presented. Next, the applicability of the APP for the surface modification of carbon films was studied. As a result of APP treatment, the chemical modification of the surface of carbon occurred. It was realized that APP promoted the surface oxidation as well selective removal of sp² clusters. The changes in the optical and electrical properties as a result of surface modification by an APP surface treatment have been illustrated.

In Chapter 5, a synthesis method for SnO₂-graphene composite formation based on in-liquid plasma developed by dispersing SnO₂ nanoparticles in ethanol has been discussed. In this chapter, a hybrid approach for composite formation by in-liquid plasma method has been proposed. A uniform distribution of SnO₂ nanoparticles on graphene sheets was achieved. As found from the microstructural and crystallographic analyses, the SnO₂ dispersion caused the formation of disorder and less crystalline graphene. The chemical composition analysis from showed SnO₂ and graphene functional groups indicating the formation of SnO₂-graphene composite. This chapter focusses on a simple, low cost, atmospheric pressure and room temperature operation of in-liquid plasma assisted hybrid approach for graphene-based composite formation.

In Chapter 6, the *in-situ* binding of SnO₂ nanoparticles to graphene sheets by in-liquid plasma method has been discussed. The SnO₂-graphene composite was fabricated at the low temperature and atmospheric pressure in a single step processing using SnCl₂ in ethanol as the only precursor. The structural observation showed the uniform distribution and formation of SnO₂ nanoparticles of size around 2-3 nm. Microstructural and crystallographic studies have shown confirming the formation of well-crystalline materials. This chapter focusses on the facile, low cost, one-step method for the SnO₂-graphene composite synthesis by the in-liquid plasma assisted *in-situ* binding.

Finally, the results and discussions in the present study are summarized, and the future scopes are described in Chapter 7.

References

- 1) X. Yu, T. Marks, and A. Facchetti, *Nat. Mater.* **15**, 383 (2016)
- 2) A. Dey, *Mater. Sci. Eng. B* **229**, 206 (2018).
- 3) K. Ellmer, *J. Phys. D: Appl. Phys.* **34**, 3097 (2001).
- 4) C. Kilic, and A. Zunger, *Phys. Rev. Lett.* **88**, 095501 (2002)
- 5) M. Batzill and U. Diebold, *Prog. Surf. Sci.* **79**, 47 (2005).
- 6) R. W. G. Wyckoff, *Crystal structures*, Interscience Publishers, New York (1963).
- 7) D. Mohanta, and M. Ahmaruzzaman, *RSC Adv.* **6**, 110996 (2016).
- 8) F. H. Jones, R. Dixon, J. S. Foord, R. G. Egdell, J. B. Pethica, *Surf. Sci.* **376**, 367 (1997)
- 9) R. Rella, A. Serra, P. Siciliano, L. Vasanelli, D. De, A. Licciulli, and A. Quirini, *Sens. Actuators B Chem*, **44**, 462 (1997).
- 10) Y. Sun, S. Liu, F. Meng, J. Liu, Z. Jin, L. Kong, and J. Liu, *Sensors* **12**, 2610 (2012).
- 11) N. Barsan, and U. Weimar, *J. Electroceram.* **7**, 143 (2001).
- 12) C. Wang, L. Yin, L. Zhang, D. Xiang, and R. Gao, *Sensors* **10**, 2088 (2010).
- 13) Y. Deng, C. Fang, and G. Chen, *J. Power Sources* **304**, 81 (2016).
- 14) W. Wei, P. Du, D. Liu, H. Wang and P. Liu, *J. Colloid Interface Sci.* **503**, 205 (2017).
- 15) S. Arote, and V. Tabhane, *Indian J. Pure Appl. Phys.* **56**, 7 (2018).
- 16) L.I. Popova, M.G. Michailov, V.K. Gueorguiev, A. Shopov, *Thin Solid Films* **186**, 107 (1990).
- 17) H. Shirakawa, E. Louis, A. MacDiarmid, C. Chiang, and A. Heeger, *J. Chem. Soc. Chem. Comm.* **16**, 579 (1977).
- 18) K. Wynne, and G. Street, *Ind. Eng. Chem. Prod. Res. Dev.* **21**, 23 (1982).
- 19) S. Kang, and G. Snyder, *Nat. Mater.* **16**, 252 (2017).
- 20) A. Syed, and M. Dinesan, *Talanta* **38**, 815 (1991).
- 21) S. Razak, I. Wahab, F. Fadil, F. Dahli, A. Khudzari, and H. Adeli, *Adv. Mater. Sci. Eng.* 356286 (2015).
- 22) Z. Boeva, and V. Segeyev, *Poly. Sci. Ser. C* **56**, 144 (2014).

- 23) T. Das, and S. Prusty, *Polym. Plast. Technol. Eng.* **14**, 1487 (2012).
- 24) D. Nicolas-Debarnot, and F. Poncin-Epaillard, *Anal. Chim. Acta.* **475**, 1 (2003)
- 25) E. Kang, Z. Li, K. Neoh, Y. Dong, and K. Tan, *Synth. Metals* **92**, 167 (1998).
- 26) P. Sengupta, S. Barik and B. Adhikari, *Mater. Manuf. Process* **21**, 263 (2007).
- 27) H. Bai and G. Shi, *Sensors* **7**, 267 (2007)
- 28) R. J. Yeo, Ultrathin Carbon-Based Overcoats for Extremely High-Density Magnetic Recording, Springer Theses, 2017.
- 29) J. Robertson, *Mater. Sci. Eng. R-Rep.* **37**, 129 (2002)
- 30) H. Kroto, J. Heath, S. O'Brien, R. Curl, and R. Smalley, *Nature* **318**, 162 (1985).
- 31) S. Iijima, *Nature* **354**, 56 (1991).
- 32) K. S. Novoselov, A. K. Geim, S. V. Morozov, D. Jiang, Y. Zhang, S. V. Dubonos, I. V. Grigorieva, and A. A. Firsov: *Science* **306**, 666 (2004).
- 33) A. Krueger, *Beilstein J. Org. Chem.* **10**, 1785 (2014).
- 34) Z. Li, Z. Liu, H. Sun and C. Gao, *Chem. Rev.* **115**, 7046 (2015).
- 35) J. Gooding, *Elect. Acta* **15**, 3049 (2005).
- 36) A. K. Geim, K. S. Novoselov, *Nat. Mater.* **6**, 183 (2007)
- 37) C. N. R. Rao, A. Sood, K. Subrahmanyam, and A. Govindraj, *Angew. Chem. Int. Ed.* **48**, 7752 (2009).
- 38) M. Bhuyan, M. Uddin, M. Islam, F. Bipasha, and S. Hossain, *Int. Nano Lett.* **6**, 65 (2016)
- 39) M. Allen, V. Tung, and R. Kaner, R.B. *Chem. Rev.* **110**, 132 (2010).
- 40) L. Viculis, J. Mack, and R. Kaner, *Science* **299**, 1361 (2003)
- 41) A. Reina, X. Jia, J. Ho, D. Nezich, H. Son, V. Bulovic, M. Dresselhaus, J. Kong, *Nano Lett.* **9**, 30 (2009).
- 42) W. S. Hummers Jr., and R. Offeman, *J. Am. Chem. Soc.* **80**, 1339 (2008).
- 43) G. Ciric-Marjanovic, *Synth. Metals* **170**, 31 (2013)
- 44) A. Asha, S. Goyal, D. Kumar, S. Kumar, and N. Kishor, *Indian J. Pure Appl. Phys.* **52**, 341 (2014).
- 45) F. Tudorache and M. Grigoras, *Optoelectron Adv. Mat.* **4**, 43 (2010)

- 46) S. Kondawar, S. Agarwal, S. Nimkar, H. Sharma and P. Patil, *Adv. Mat. Lett.* **3**, 393, (2012)
- 47) N. Deshpande, Y. Gudage, R. Sharma, J. Vyas, J. Kim, and Y. Lee, *Sens. Actuators B* **138**, 76 (2009)
- 48) T. Xiang, Z. Lin and Y. Qu, *J. Nanosci Nanotechnol.* **15**, 4493 (2015).
- 49) L. Geng, *Trans. Nonferrous Met. Soc. China* **19**, 678 (2009).
- 50) M. Diantoro, Kholid, A. Mustikasari, and Yudiyanto, *IOP Conf. Ser. Mater. Sci. Eng.* **367**, 12034 (2018).
- 51) H. Sharma, N. Sonwane, and S. Kondawar, *Fibers Polym.* **16**, 1527 (2015).
- 52) Y. Li, H. ban, M. Jiao, and M. Yang, *RSC Adv.* **6**, 74944 (2016).
- 53) H. Tai, Y. Jiang, G. Xie and J. Yu, *J. Mater. Sci. Technol.* **26**, 605 (2012).
- 54) H. Tai, Y. Jiang, G. Xie, J. Yu and X. Chen, *Sens. Actuators B* **125**, 644 (2007).
- 55) H. Tai, Y. Jiang, G. Xie, J. Yu, X. Chen and Z. Ying, *Sens. Actuators, B* **129**, 319 (2008).
- 56) H. Zhu, Z. Xu, D. Xie and Y. Fang, *Graphene Fabrication, Characterizations, Properties and Applications*, ScienceDirect, 2018.
- 57) Y. Chang, Y. Yao, B. Wang, H. Luo, T. Li and L. Zhi, *J. Mater. Sci. Technol.* **29**, 157 (2013)
- 58) F. Li, J. Song, H. Yang, S. Gan, Q. Zhang, D. Han, A. Ivaska, and L. Niu, *Nanotechno.* **20**, 455602 (2009)
- 59) L. Liu, M. An, P. Yang, and J. Zhang, *Sci. Rep.* **5**, 9055 (2015).
- 60) Y. Xiao, Q. Yang, Z. Wang, R. Zhang, Y. Gao, P. Shun, Y. Sun, and G. Lu, *Sens. Actuat. B* **227**, 419 (2016).
- 61) C. Hu, T. Lu, F. Chen and R. Zhang, *J. Chin. Ad. Mater. Soc.* **1**, 21 (2013).
- 62) S. Paek, E. Yoo, and I. Honma, *Nano Lett.* **9**, 72 (2009).
- 63) M. Khan, M. Tahir, A. Syed, H. Khan, M. Siddiqui, A. Al-warthan, and W. Tremel. *J. Mater. Chem. A* **3**, 18753 (2015).
- 64) K. P. Loh, Q. Bao, K. P. Ang and J. Yang, *J. Mater. Chem.* **20**, 2277 (2012).
- 65) A. Jana, E. Scheer, and S. Polarz, *Beilstein J. Nanotechnol.* **8**, 688 (2017).

- 66) H. Kim, H. Na, Y. Kwon, S. Kang, M. Choi, J. Bang, P. Wu, and S. Kim, *ACS Appl. Mater. Interfaces* **9**, 31667 (2017).
- 67) P. Lian, X. Zhu, S. Liang, Z. Li, W. Yang, and H. Wang, *Electrochim. Acta* **56**, 4532 (2011).
- 68) J. Liang, W. Wei, D. Zhong, Q. Yang, L. Li, and L. Guo, *ACS Appl. Mater. Interfaces* **4**, 454 (2012)
- 69) A. Dhanabalan, X. Li, R. Agarwal, C. Chen, and C. Wang, *Nanomater.* **3**, 606 (2013).
- 70) Y. Deng, C. Fang, and G. Chen, *J. Power Sources* **304**, 81 (2016).
- 71) S. Gupta-Chatterjee, S. Chatterjee, A. Ray, and A. Chakraborty, *Sens. Actuators B* **221**, 1170 (2015).
- 72) F. Meng, H. Li, L. Kong, J. Liu, Z. Jin, W. Li, Y. Jia, J. Liu, and X. Huang, *Anal. Chim Acta* **736**, 100 (2012).
- 73) Z. Abideen, J. Park, H. Kim, and S. Kim, *Nanotechnol.* **28**, 35501 (2017).
- 74) S. Mao, S. Cui, G. Lu, K. Yu, Z. Wen, and J. Chen, *J. Mater. Chem.* **22**, 11009 (2012).
- 75) Z. Song, Z. Wei, B. Wang, Z. Luo, S. Xu, W. Zhang, H. Yu, M. Li, Z. Huang, J. Zang, F. Yi, and H. Liu, *Chem. Mater.* **28**, 1205 (2016).
- 76) The 153rd Committee on Plasma Material Science, Japan Society for Promotion of Science, Atmospheric Pressure Plasma Fundamental and Applications, Tokyo, Japan (2009).
- 77) Y. Kusano, H. Mortensen, B. Stenum, S. Goutianos, S. Mitra, A. Ghanbari-Siahkali, P. Kingshott, B.F. Sørensen, and H. Bindslev, *Int. J. Adhesion Adhesives* **27**, 402 (2007).
- 78) M. Costa, and F. Freire Jr. *Dimon. Rel. Mater.* **22**, 1 (2012).
- 79) H. Watanabe, H. Kondo, M. Sekine, M. Hiramatsu, and M. Hori, *Jpn. J. Appl. Phys.* **51**, 01AJ07 (2012).
- 80) G. Saito, and T. Akiyama, *J. Nanomater.* 123696 (2015).
- 81) D. Mariotti, and R. Mohan Sankaran, *J. Phys. D: Appl. Phys.* **43**, 323001 (2010).

- 82) Q. Chen, J. Li, and Y. Li, *J. Phys. D: Appl. Phys.* **48**, 424005 (2015).
- 83) S. Horikoshi, and N. Serpone, *RSC Adv.* **7**, 47196 (2017).
- 84) T. Hagino, H. Kondo, K. Ishikawa, H. Kano, M. Sekine, and M. Hori, *Appl. Phys. Express* **5**, 035101 (2012)
- 85) T. Amano, H. Kondo, K. Takeda, K. Ishikawa, M. Hiramatsu, M. Sekine, and M. Hori, *Jpn. J. Appl. Phys.* **57**, 45101 (2018).
- 86) A. Ando, K. Ishikawa, H. Kondo, T. Tsutsumi, K. Takeda, T. Ohta, M. Ito, M. Hiramatsu, M. Sekine, and M. Hori, *Jpn. J. Appl. Phys.* **57**, 26201 (2018).

Chapter 2

Experimental setups and material evaluation methods

2.1 Synthesis methods

2.1.1 Synthesis of SnO₂ nanoparticles (sol-gel method)

The SnO₂ nanoparticles used in this study as a component material for the composite formation in this study were synthesized by sol-gel method. The sol-gel method is a flexible technique to synthesis materials at low temperatures. ¹⁾ The sols are solid particles in liquid and gels are a continuous network of the particles with pores filled with the liquid. Synthesis of sol-gel involves hydrolysis of precursors, condensation to form particles, gelation and drying to obtain the final product. ²⁾

The sol-gel method is one of the well-known and established as a method for metal oxide nanoparticle synthesis. The sol-gel method is an excellent tool to deploy a controlled architecture in material chemistry to fabricate metal oxide nanostructures. The sol-gel method offers control over various structural and chemical properties of metal oxides. ³⁾ The formation of metal oxide by sol-gel method encompasses successive steps, at first, the metal precursor undergoes the hydrolysis to yield the metal hydroxide solution, followed by condensation which leads to the formation of three-dimensional gels. ⁴⁾ Afterward, the obtained gel is subjected to the drying process. The schematic of the process has been shown in Fig. 2-1. The factors involved in these steps contribute towards determining the shape and the size of synthesized metal oxide particles such as choice of solvent, additives, aging time, and heat treatments. ⁵⁾

In the sol-gel synthesis of SnO₂ nanoparticles in this study, an aqueous solution of SnCl₂·2H₂O was used as a precursor. A 0.1M solution of SnCl₂·2H₂O was prepared using a distilled water. The solution was heated at 60°C and stirred for 15 min. With continued stirring, 1M NaOH was added to the solution dropwise until the solution turned the pH of 8. Persistent stirring of the solution with 400 rotation-per-minute (rpm) was carried out at 60°C for another 2 hours. After 2 hours of stirring, the solution changed its color from white to gray indicating the formation of SnO₂. The final product was cleaned several times with water and ethanol to remove impurities and then filtered to obtain a precipitate. The precipitate was air-dried and later, annealed at 400°C for 2 hours to a fine powder of SnO₂ nanoparticles.

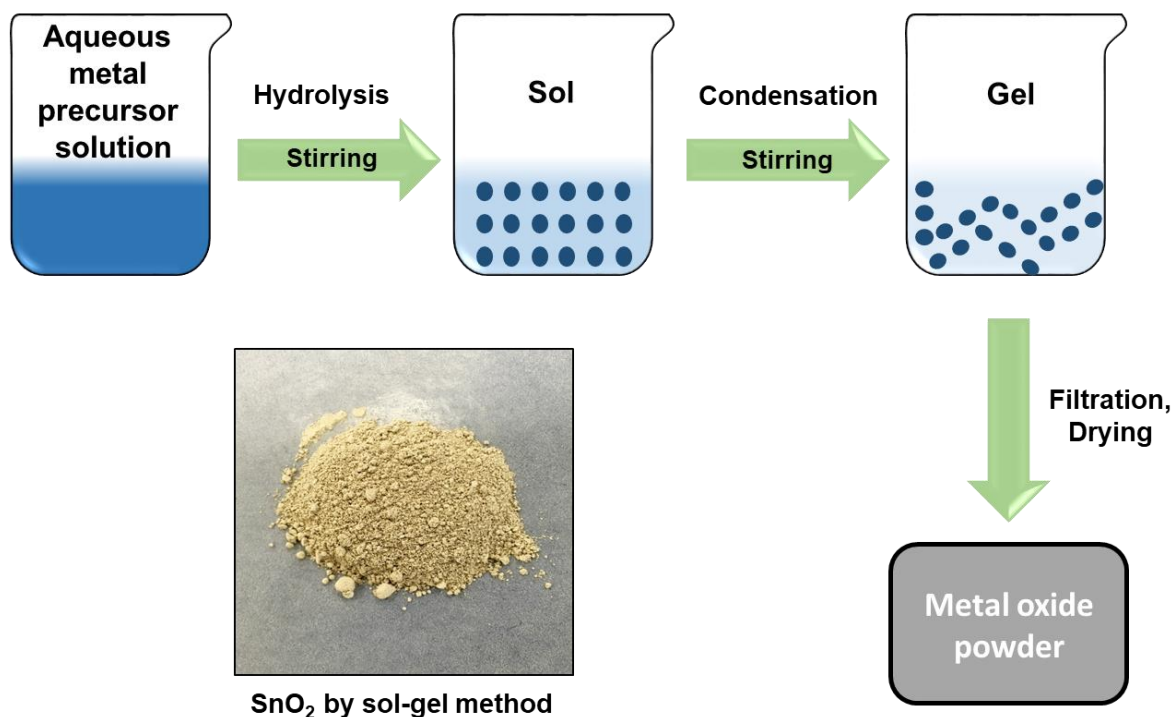


Fig. 2-1 Schematic of the sol-gel process for metal oxide synthesis.

2.1.2 Synthesis of Polyaniline (chemical oxidative method)

The polyaniline (PANI) can be synthesized by electrochemically or chemically induced oxidative polymerization.⁶⁾ In the present study, the polymerization of aniline monomer was carried out by the chemical oxidative method. This process consists of oxidation of aniline monomer followed by coupling of charged aniline monomers to get the polymer (PANI).

The choice of monomer in the oxidative polymerization process depends on the electron donor properties and high oxidation tendency of the monomer. Aromatic amines, phenols, and thiophenols or sulfur- and nitrogen-containing heterocycles due to the presence of electron donor substituent in benzene or heterocyclic ring fulfill the requirements of monomer properties. Oxidation of monomer takes place under the action of the inorganic (or organic) oxidizing agent. During this process, cation or cation radical sites are generated in monomer (polymer) molecule, thus initiating the polymer growth. In the case of aniline, the oxidized nitrogen-containing structure attacks the phenyl ring of another aniline molecule and substitutes one proton of the ring. Both the ring and nitrogen-containing structure lose one proton; after that, monomer units bind with each other, and the chain becomes longer. A wide range of oxidants is used in the chemical synthesis of PANI. As a rule, compounds with high oxidation potentials exceeding +1.0 V (persulfates, dichromates, cerium (IV) salts, aurates) are employed. This is associated with the fact that the onset of the propagation of the polymer chains in acidic media requires overcoming energy barrier corresponding to an oxidation potential of +1.05 V. Once the propagation starts, the oxidation potential of the reaction decreases. In the chemical synthesis of PANI, persulfates (having an oxidation potential of +2.01 V) are used most widely.^{7, 8)}

The stepwise chemical oxidative polymerization of aniline has been proposed by researchers. It includes 1) oxidation of nitrogen atom of monomer followed by oxidation of end nitrogen atom of oligomer and polymer; 2) addition of a monomer in the “nitrogen-carbon” fashion as a result of chain reaction (electrophilic substitution of the proton in the aromatic ring of monomer by oxidized polymer fragment).⁹⁾

In the present study, synthesis of PANI was carried out using an aqueous solution of aniline as precursor and ammonia peroxydisulphate (APS) as an oxidant. The PANI was doped by H_2SO_4 to improve electrical properties of the PANI as the PANI chain contains alternative single and double bonds leading to form a broad electron conjugation, dopants are requiring to inject electrons or remove electrons. The schematic of the chemical oxidative method for polyaniline synthesis has been shown in Fig. 2-2.

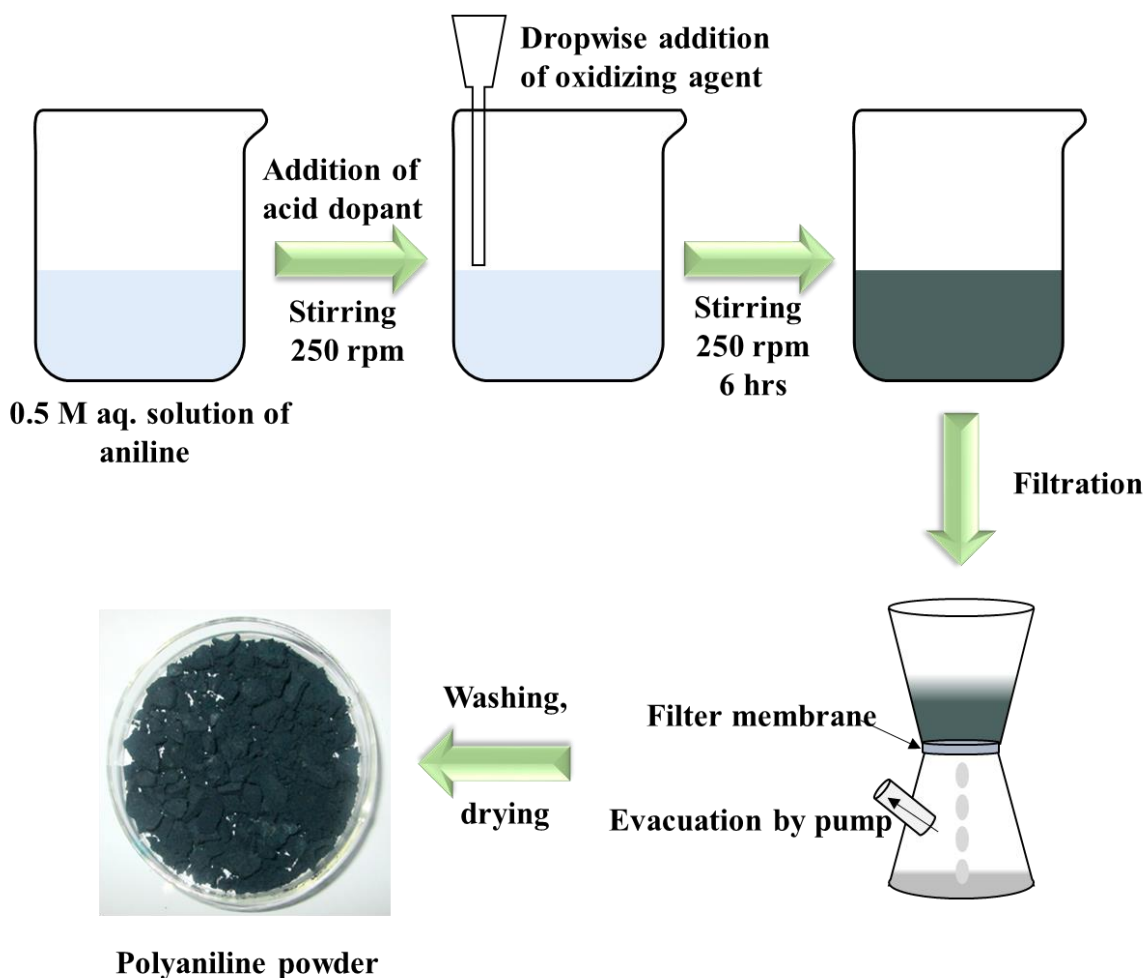


Fig. 2-2 Schematic of the chemical oxidative method for polyaniline synthesis.

2.1.3 Deposition of carbon films (Closed field unbalanced magnetron sputtering)

Among various deposition techniques for carbon films such as laser ablation, ion plating, and magnetron sputtering, carbon film deposition by magnetron sputtering offers homogeneous deposition with process simplicity.¹⁰⁾ In the present study, carbon films were deposited by the closed field unbalanced magnetron (CFUBM) sputtering process.

In the sputtering process, materials are evaporated by the bombardment of energetic ions on the target surface. Film structures are strongly correlated with the plasma density of magnetron sputtering as plasma properties, the degree of plasma confinement, ion energy, plasma density, plasma temperature, substrate temperature, and substrate position are the key parameters for the controllable film deposition.¹¹⁾ Conventional magnetron sputtering suffers low deposition rate due to low ionization in the plasma and confinement of the plasma in the only target region.¹²⁾ In an unbalanced magnetron, the plasma is not confined in the target region resulting in increased ion bombardment but it's difficult to maintain the uniformity of the deposited films. This issue led to the development of the CFUBM sputtering system. In CFUBM sputtering system, since unbalanced magnetron is facing each other, the magnetic field lines between magnetrons form a closed trap for the electrons in the plasma and form a dense plasma in the substrate region.¹³⁾

In the deposition process of carbon films by CFUBM sputtering process, glass substrates were used. The background pressure in the sputtering chamber was maintained at 3×10^{-5} Torr before introducing sputtering gas of Ar gas with a flow rate of 80 sccm. The glass substrate with a size of 20-mm²-squared shape was placed in a rotary sample holder at the center of the chamber (Fig. 2-3). The graphite targets with a total area of 80 cm² were applied by a radio-frequency (rf) power. The films were deposited with various discharge powers (1200, 1600 and 2000 W) for different power density values (15, 20, and 25 W/cm²). The film thickness was controlled at a constant of 180 nm by the deposition time. The glass substrates were cleaned ultrasonically in a mixture of acetone and alcohol prior to deposition.

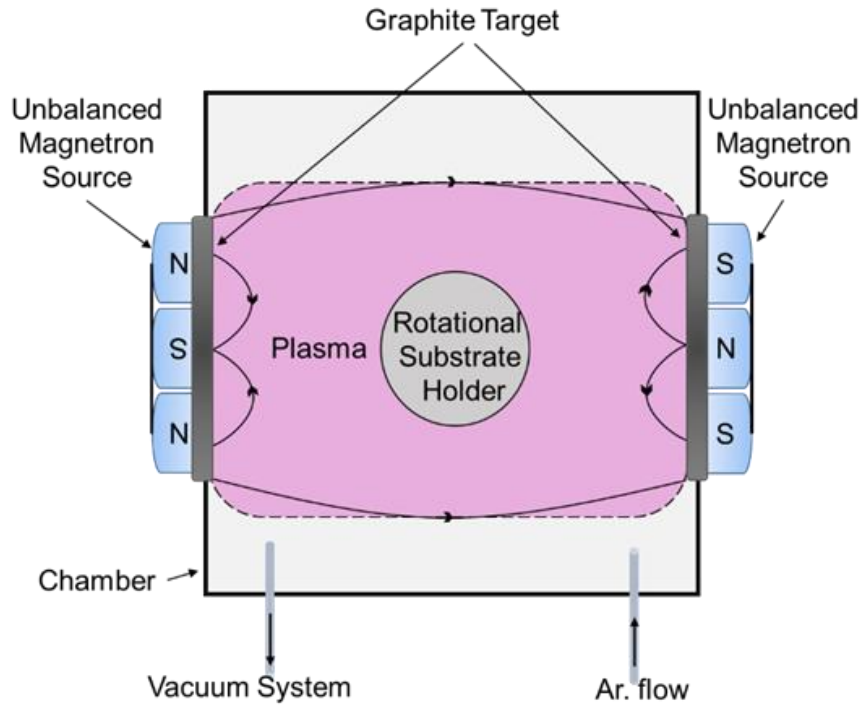


Fig. 2-3 The schematic of closed field unbalanced magnetron sputtering system. ¹¹⁾

2.1.4 Synthesis of graphene and graphene-based composite (the in-liquid plasma method)

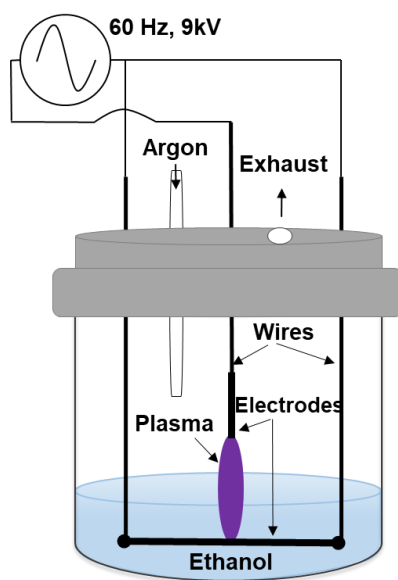
The in-liquid plasma used in this study utilizes the micro hollow cathode method.¹⁴⁻¹⁶⁾ The electrode above the liquid surface is an electrode using a micro hollow cathode, and the tip of the electrode above the liquid surface is cylinder-shaped. By applying a voltage to the electrode above the liquid surface, electrons are emitted from the inside of the electrode and accelerated to the inside of the electrode below the liquid surface. Due to the electric field, the repulsion and acceleration of electrons in opposite direction take place. An iterating repulsion of electrons leads to a constant collision with neutral particles contributing towards maintaining the discharge. The micro hollow cathode method provides a higher current density than the ordinary discharge thus the discharge sustaining current turn out to be low. In this study, a non-equilibrium atmospheric plasma having a high electron density or more is generated in the micro hollow region at the tip of the electrode above the liquid surface.^{17, 18)}

Figure 2-4 (a) is a schematic diagram of the in-liquid plasma device used in this study.¹⁷⁾ A pure Ar gas was flown into the glass reactor at atmospheric pressure with a flow rate of 6 standard-liter-per-minute (slm) to fill the upper part of the glass reactor above the liquid surface. The electrodes were positioned as shown in Fig. 2-4 (a) to make three phase system. In the case of the upper electrode, a distance between the liquid surface and electrode was 10 mm and the liquid inside the liquid was 10 mm below from the liquid surface. As shown in Figure 2-4 (a), a 9 kV was applied to the electrode above liquid surface and electrode inside liquid via the liquid level ethanol with a 60 Hz AC power source to generate the in-liquid plasma. A chronological discharge then was ensued between high-density plasma and electrode was immersed in liquid through the gas-liquid interface. The solution changed its color to black within a few minutes of plasma discharge. The upper gas phase electrode has a micro hollow cathode structure, and the generated nonequilibrium atmospheric pressure plasma reaches the lower liquid phase electrode. Decomposition of ethanol occurred due to the plasma discharge to form graphene (Fig. 2-4 (b)). After 30 min of the discharge, the synthesized material was

collected by filtering the black colored solution with the suction filtration using a membrane filter with pore size of 1 μm and dried at 60°C for 15 min.

For a composite synthesis, similar process parameters were utilized with the dispersion of SnO_2 or SnO_2 precursors.

a)



b)

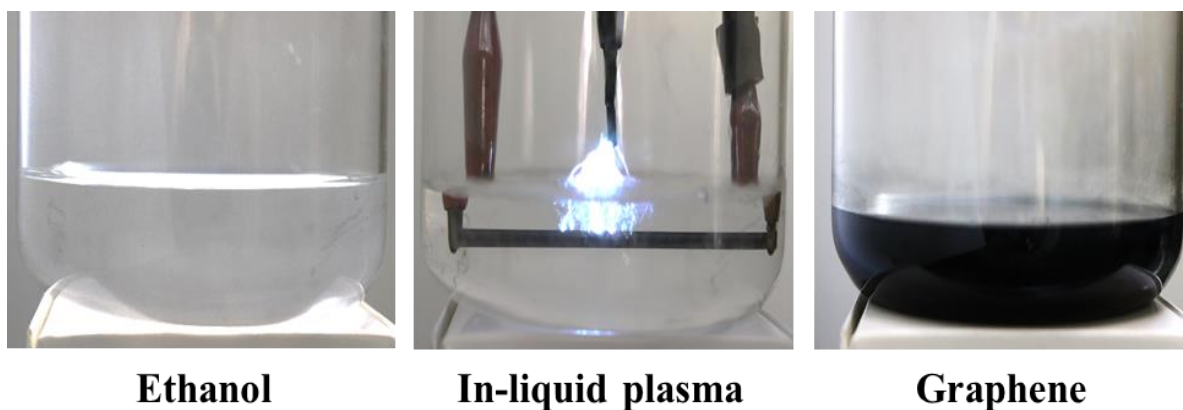


Fig. 2-4 a) The in-liquid plasma apparatus used in this study, and b) A state of art plasma discharge and formation of graphene.

2.1.5 Low temperature atmospheric pressure plasma surface treatment

The atmospheric pressure plasma (APP) surface treatment was carried out to modify the surface of magnetron sputtered carbon films. Figures 2-5 (a, b) show a schematic illustration of the bottom and the side of the APP source set above carbon films. The plasma plume was extended to about 6 mm from the exit and the exit slit was 20×1 mm. In previous studies, the characteristics of this source were analyzed by vacuum ultraviolet absorption spectroscopy. The plasma density was $2 \times 10^{16} \text{ cm}^{-3}$.¹⁹⁾

As deposited films (power density: 25 W/cm^2 , thickness: 180 nm, size: 10 mm x 10 mm) were treated by the APP operated with Ar gas flow of 2 slm. The high voltage of 60-Hz alternative current was applied with a voltage of 9 kV to the APP source. The substrate to source distance was maintained at 3 mm. The plasma treatment was uniform for the entire film surface by scanning. The effect of plasma exposure time was studied by varying treatment time (1, 3, 4 and 5 minutes). Figure 2-5 (c) shows the schematic of the APP surface treatment of carbon films.

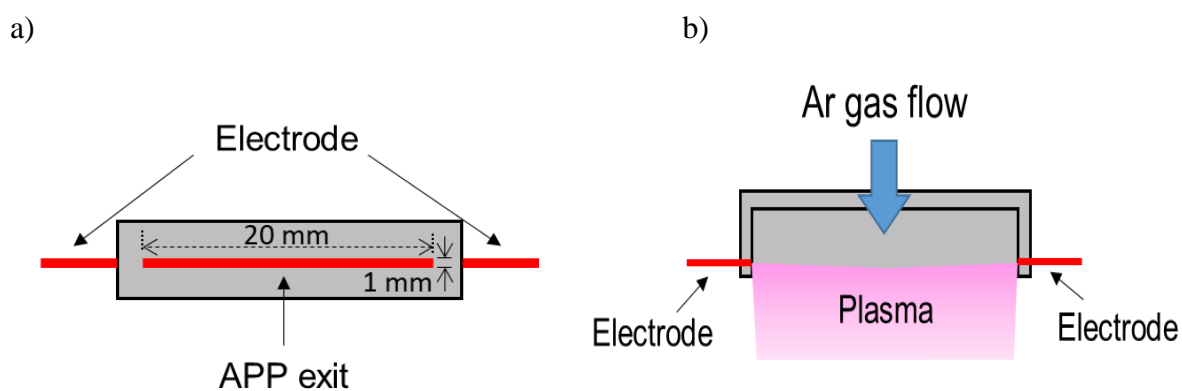


Fig. 2-5 a) Schematic illustration of the bottom and b) the side of the APP source.

(cont.)

c)

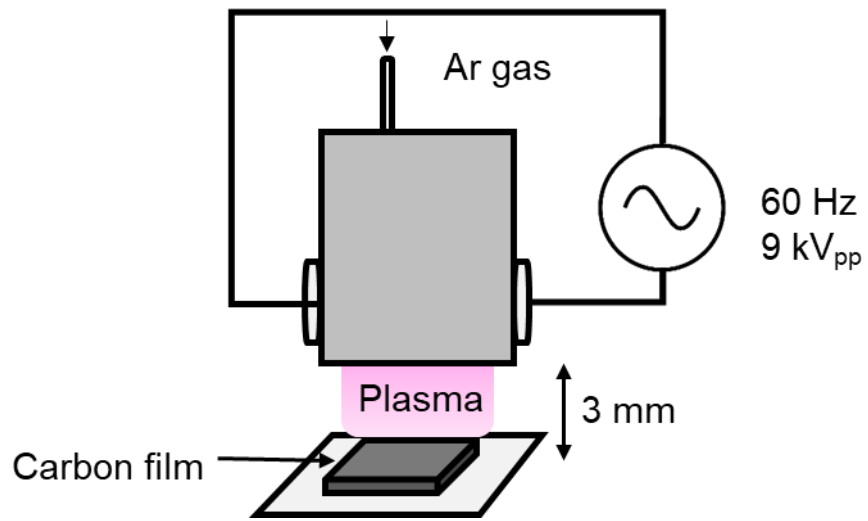


Fig. 2-5 c) Schematic illustration of the APP surface treatment of carbon films.

2.2 Plasma diagnosis

2.2.1 Optical emission spectroscopy (OES)

Plasma in a liquid has been investigated using imaging and OES technique enabling the measurement of basic plasma parameters, discharge morphology, gas temperature, electron density, and excitation temperature. ²⁰⁾

The plasma can be diagnosed optically by observing the light emission from excited species in the plasma. The excited atoms and ions in the plasma create a distinctive emission spectrum explicit to each element. This emission is a result of the collision of constituents of plasma (charged and neutral particles, electrons and ions). The collision of electrons with atoms, molecules, and radicals takes place, the particles at the electronic excited level emit light of a specific frequency by the transition to the lower level. The kind of light emitting particles (elements/species) can be identified from the wavelength depending on the energy state. ²¹⁾

In the emission spectrum, the intensity depends on the concentration of elements present and given by equation 2.1,

$$I_x \propto n_e n_X \int \sigma_X(\varepsilon) v(\varepsilon) f_e(\varepsilon) d\varepsilon = k_{eX} n_e n_X \quad \dots (2.1)$$

where n_e is the electron density, n_X is a concentration of element (X) present, $\sigma_X(\varepsilon)$ is the collision cross section for the electron impact excitation of X as a function of electron energy ε , $v(\varepsilon)$ is the electron velocity and $f_e(\varepsilon)$ is the electron energy distribution function, k_{eX} is the excitation rate coefficient for excited element (X^*) by electron impact on the element (X). Under a condition where k_{eX} and n_e values unchanging, the obtained emission intensity is proportional to density. However, these values depend on the experimental conditions.

In the present study, the gas phase plasma diagnosing has been focused to identify elements present in the plasma and to improve author's understandings of mechanism and operation. The optical emission from the in-liquid plasma was obtained in the gas phase region close to 3 mm above the liquid surface. The plasma emissions were measured using multi-channel Ocean optics HR-4000 spectrometer in the range between 200 and 900 nm.

2.2.2 Electrical diagnosis (Parameters for plasma processes)

Plasma generation is subject to the energy supply to neutral gas to form the charge carriers. Electrons and ions are produced in the gas phase when electrons or photons with sufficient energy collide with the neutral atoms and molecules in the feed gas. Any volume of a neutral gas always contains a few electrons and ions that are formed. These free charge carriers are accelerated by the electric field and new charged particles may be created when these charge carriers collide with atoms and molecules in the gas or with the surfaces of the electrodes. This leads to an avalanche of charged particles that is eventually balanced by charge carrier losses so that a steady-state plasma develops.²²⁾ Since the electric field and electric parameters have a key role in the plasma generation, it is necessary to pay attention to electric parameters for the plasma process.

In the present study, three different plasma processes have been studied, magnetron sputtering for carbon film deposition, atmospheric pressure plasma for surface treatment of carbon films and in-liquid plasma for graphene-based composite formation. In the case of magnetron sputtering, a radio frequency power of 13.56 MHz as applied and equally distributed using the single matching network with varying power density. It has been observed that electric parameters have a great effect on the plasma parameters (concentration of species in the plasma) contributing to deposition of carbon films.²³⁾ In the case of APP source for surface treatment, the APP source was connected to the 60 Hz AC high voltage power-source driven by 9 kV_{0-p}. Plasma behavior is strongly electric parameter dependent, thus the same parameters were used throughout the study.¹⁹⁾ In the case of in-liquid phase plasma, a 9 kV was applied to the upper and electrode and a lower electrode with 60 Hz AC power source to generate the in-liquid phase plasma. In this process, by applying a voltage to electrodes, electrons are emitted from inside electrodes and accelerated to the inside of opposing electrode. The current density in the discharge is higher in this arrangement compared to other. In addition to this, the plasma generation in the liquid is strongly dependent on the conductivity of the liquid.²⁴⁾

2.3 Material evaluation methods

2.3.1 Scanning electron microscopy (SEM)

The surface morphological observations of materials are important not only for the academic point of view but also for manufacturing and application development based on these materials. Scanning electron microscope (SEM) offers an easy way to observe the surface morphology of the materials with minimum efforts for the preparation of the sample, from low to high magnification without destruction to the material.

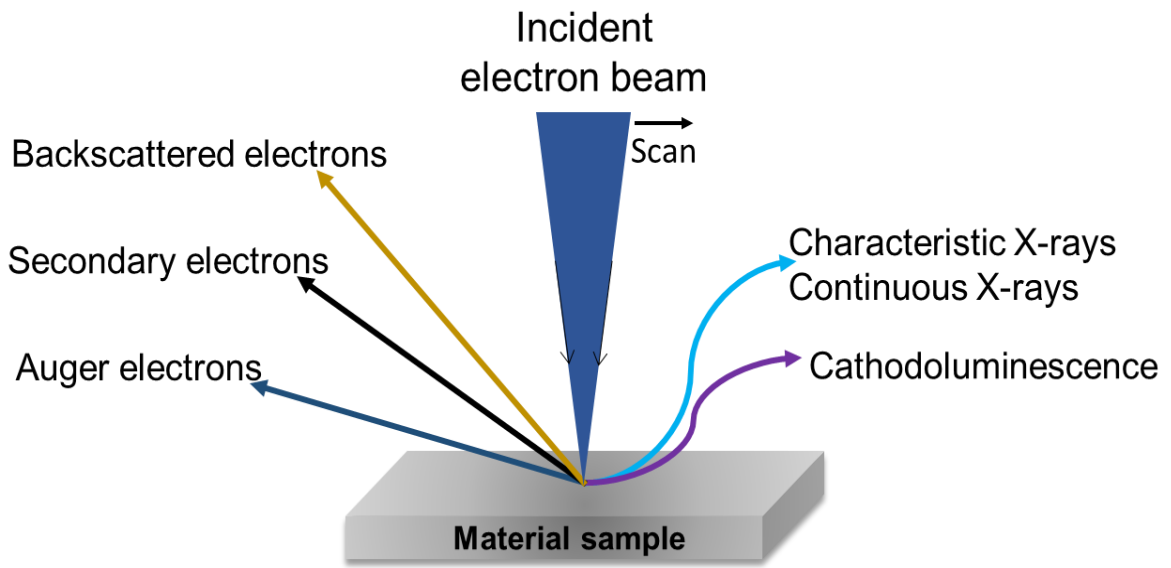
When an electron beam directed towards material with highly concentrated electrons irradiated on the material, the surface of the material emits secondary electrons, backscattered electrons, X-rays, cathode luminescence, and Auger electrons (Fig. 2-6 (a)). Secondary electrons which are of energy less than 50 eV are generated even deeper than material surface but among them, only those are generated close to sample surface (~10 nm) are able to get out of the surface into the vacuum. With the detection of these electrons, it is possible to acquire information about the surface shape and distribution of the materials.

The essential components of SEM include electron gun, electron lenses, a sample stage, detectors, and data output devices. An electron beam of diameter (~10 nm or less) originated from the electron gun converged by focusing lens and an objective lens. The deflection coil facilitates the 2-D scanning of the material surface by an electron beam. Detectors convert the data obtained (secondary electrons, backscattered electrons) into electric signals. After the amplification of the electric signal, it sends to the display unit. The scanning on the display unit is in synchronization with the electron beam. Dependable brightness variation with respect to secondary electrons enables the formation of the SEM image. An observation of atoms is not possible by the SEM as the resolution of the SEM is only 0.5 nm. The spatial resolution of the SEM is electron beam diameter dependent. A finely focused electron beam can generate a sharp SEM image. In the case of carbon materials, the electron beam aberrantly disseminates inside the sample, barring the performance of the SEM. The electron beam penetrates deeper in the case of carbon materials resulting in the generation of the information other than surface and backscattered electrons. The penetration of the electron beam and the diameter are depending

on the accelerating voltage thus, the choice of an optimum voltage for each sample can offer a good resolution of the SEM image of the material surface. In the case of conductive samples, such as sputtered carbon films, the disseminated electrons after the penetration into the material get absorbed after losing their energy and flow through the material, due to this charging of material occurs. Due to the charging of the material, a deflection of electron probe over the material surface gets by the repulsive forces from charged potential occurs leading the formation of a distorted image. To overcome this, the number of electrons flowing through sample should be equal to a number of electrons exiting the sample, this can be done by applying conductive tape to the sample.

Figure 2-6 (b) shows the SEM image of the SnO₂. This image was taken using an accelerating voltage of 15 kV, the emission current 10.1 μ A and with a working distance of 7011 μ m by an instrument SU8230 Hitachi High Technology Corporation. Grains in order of several tens of nanometers are observed. It is thought that each one of these was a SnO₂ nanoparticle.

a)



b)

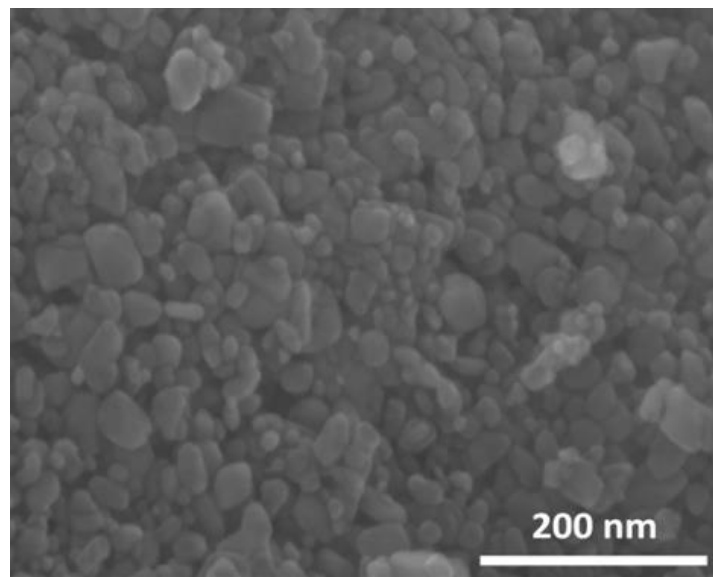


Fig. 2-6 (a) A principle of the SEM, and (b) SEM image of SnO₂.

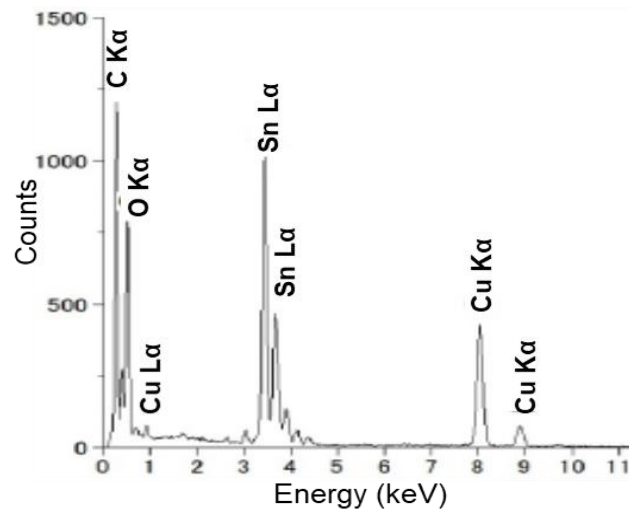
2.3.2 Energy dispersive X-ray spectroscopy (EDS or EDX)

The EDS offers the elemental or chemical analysis of the sample. When an electron beam directed towards material with highly concentrated electrons irradiated on the material, the surface of the material emits secondary electrons, backscattered electrons, X-rays, cathode luminescence, and Auger electrons (Fig. 2-7 (a)). The chemical analysis in the EDS is a result of detection of X-rays emitted by a material after the electron beam irradiation. A line identification in emitted X-ray spectrum gives the qualitative analysis (elements present) of the material and the line intensity measurements enable quantitative analysis (concentration of the elements present) of the material.

The EDS system contains an X-ray detector, a pulse processor and multiple channel analyzer as basic components of the system. The EDS produces the map or element distribution by the simple use of scanning electron beam and measuring intensities of emitted X-ray lines (characteristic X-rays). The intensities of X-rays are measured by counting photons. The spatial resolution of EDS depends on the penetration and spreading of the electron beam used for irradiation. ED spectra in a graphical form contain x-axis as X-ray energy and y-axis as counts per channel. With the addition of X-ray spectrometer, the SEM instrument can be used for EDS analysis, thus the sample preparation for EDS analysis is the same as the SEM. The backscattered electron analysis from SEM gives an image with compositional contrast, and the EDS enables elemental identification of the sample. The stationary electron beam can give the localized elemental information, and the map of elemental distribution can be generated by defining elements prior to scanning.

Figure 2-7 (a) shows EDS spectra of the SnO₂-graphene composite containing only carbon, oxygen and tin, and Fig. 2-7 (b) shows the EDS mapping of the SnO₂-graphene composite.

a)



b)

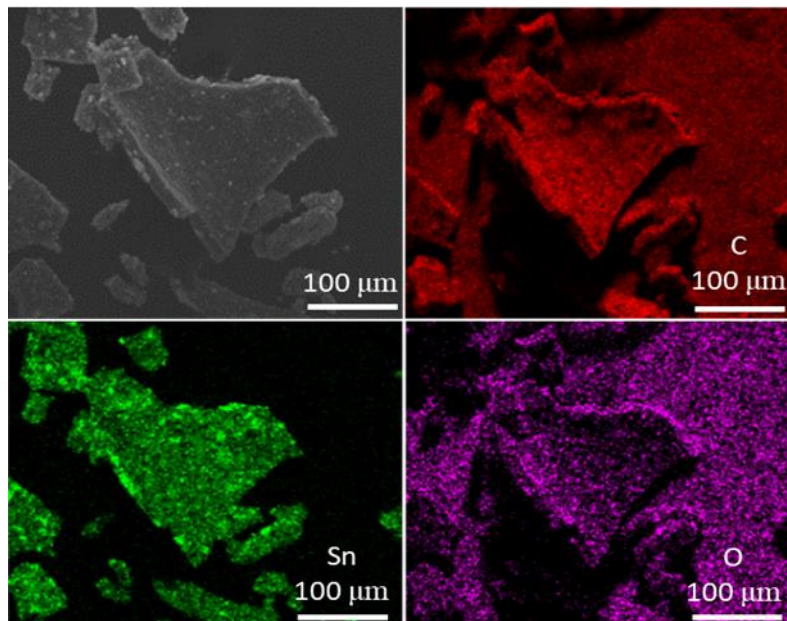


Fig. 2-7 a) Sample EDS spectra of SnO₂-graphene composite and b) Sample element mapping by EDS of SnO₂-graphene composite.

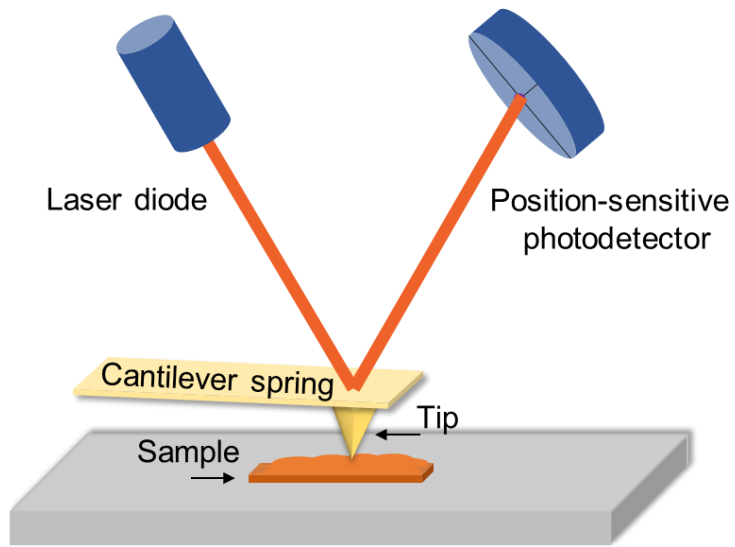
2.3.3 Atomic force microscopy (AFM)

The AFM is a unique characterization tool to get a 3D profile of the material surface at a nanoscale. The AFM uses a sharp probe (tip) of Si usually to measure the forces between the probe and the material surface. The force (Van der Waals interactions) measurements are carried out at a very short distance of 0.2 nm to 10 nm. The sharp tip in the AFM is supported by a supple cantilever and the tip is placed at end of the cantilever. The force between tip and material surface depends on the stiffness of the cantilever and distance between tip and material surface. The force is a product of cantilever deflection and stiffness of the cantilever and given by Hooke's law. During measurements, if the stiffness of the cantilever is less than surface then the bending of cantilever occurs, and deflection gets recorded.

The AFM system contains a sharp tip, cantilever, laser diode, and position sensitive photodiode. The position of these instruments is as shown in Fig. 2-8 (a). During the scanning of the sample surface by the tip, the bending of the cantilever is measured by the position sensitive photodiode to produce a map of the material surface. This process is called as a laser assisted beam bounce method. The AFM used two scanning modes, contact mode and non-contact mode respectively. In a contact mode, the deflection of the cantilever is constant and in a non-contact mode, the tip oscillates at the resonant frequency and the amplitude of oscillation is constant. These modes have some disadvantages such as surface destruction, low resolution, distorted image formation to name a few. Thus, a tapping mode imaging is generally used, it's the combination of the above two modes. The typical AFM resolution in x-y-direction is 1 nm and in z-direction its 0.1 nm. The sample preparation for AFM is simple with few requirements such as a flat and rigid substrate, and immobile sample.

Figure 2-8 (b) shows the typical AFM data obtained for APP treated carbon films. The topography of the surface was easily observed with AFM analysis. The roughness development was observed in the APP treated sample by AFM analysis.

a)



b)

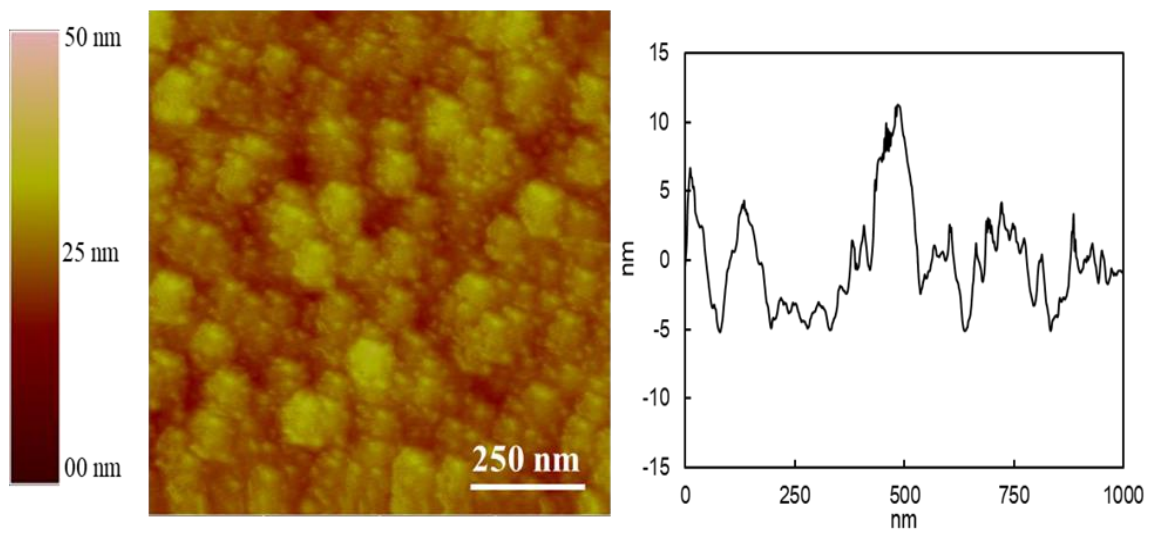


Fig. 2-8 a) A principle of the AFM and b) Sample AFM data of APP treated carbon film.

2.3.4 Transmission electron microscopy (TEM)

The TEM offers the structural analysis at the atomic level. In the TEM, the entire sample surface and/or localized area can be analyzed. The resolution of the TEM is 0.2 nm which is almost equal to the separation between two atoms in a solid. Through TEM, morphological (size, shape, arrangement), crystallographic, and compositional information can be acquired, which makes it a unique material characterization technique.

In the TEM, an electron beam is transmitted through a thin sample, some of the electrons pass through the sample called as unscattered electrons (direct beam) (Fig. 2-9 (a)). The detection of elastically scattered electrons and unscattered electrons is important for the formation of the TEM image. With magnification and focusing arrangement using lenses, the detection of the signal is carried out to get the final image.

The TEM consist of multiple and multistage lens systems (converging lens, an objective lens, intermediate lens and projector lens) as shown in Fig. 2-9 (b). With filament heating and an increasing electron accelerating voltage of the electron gun, the electron beam is generated. The TEM operates at the high accelerating voltage (several tens kV to several hundred kV). The wavelength of the electron beam is accelerating voltage. With increasing accelerating voltage shorter wavelength of the electron beam, the higher energy of electrons can be obtained to get the better resolution. An emitted electron beam from the electron gun is collected by a converging lens and irradiated on the material. A condenser aperture in between focusing lens and sample adjusts the light quantity of the electron beam. The position of the converging diaphragm should be at the center of the optical path. After passing through the material, the electron beam goes to the objective lens, as a result, the enlargement takes place. After this phase, the intermediate lens and projector lens enlarges the image again to get the final TEM image. In this process, the objective lens has an important role, the contrast of the image is increased by inserting an objective aperture into the back focal plane of the objective lens. The final image can be seen on the fluorescent screen. The sample preparation for TEM is very important. For the TEM analysis, a thin material sample is needed. In the present study, the

TEM grid made up of copper was used to deposit material on it. The TEM grid had a supporting amorphous carbon film with holes to get suspended material.

Figure 2-9 (c) is a TEM image and Fig. 2-9 (d) is a High Resolution (HRTEM) image of the SnO₂-graphene composite. The high contrast spots in the image (Fig. 2-9 (d)) were identified as a SnO₂. Such an image contrast is due to the interaction of electron beam and material. In the HRTEM, denser areas and elements containing heavier elements appear darker due to scattered electrons in the material. The scattering from the crystal planes causes the diffraction contrast depending on the orientation of the crystalline area. The left corner in the image of Fig. 2-9 (d) shows dark and bright lines. These lines can be counted for an estimation of a number of layers of graphene.

a)

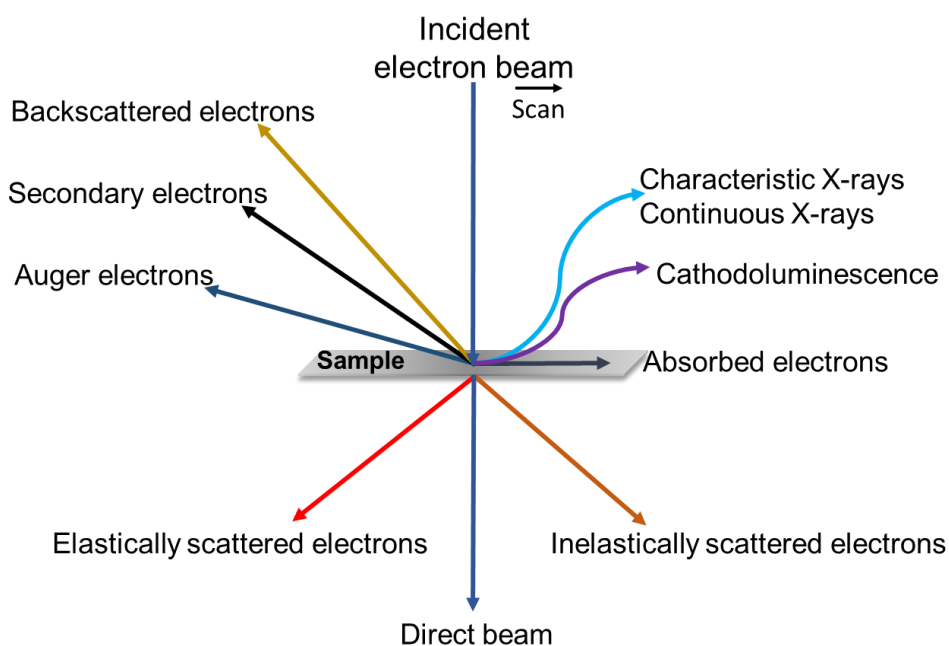
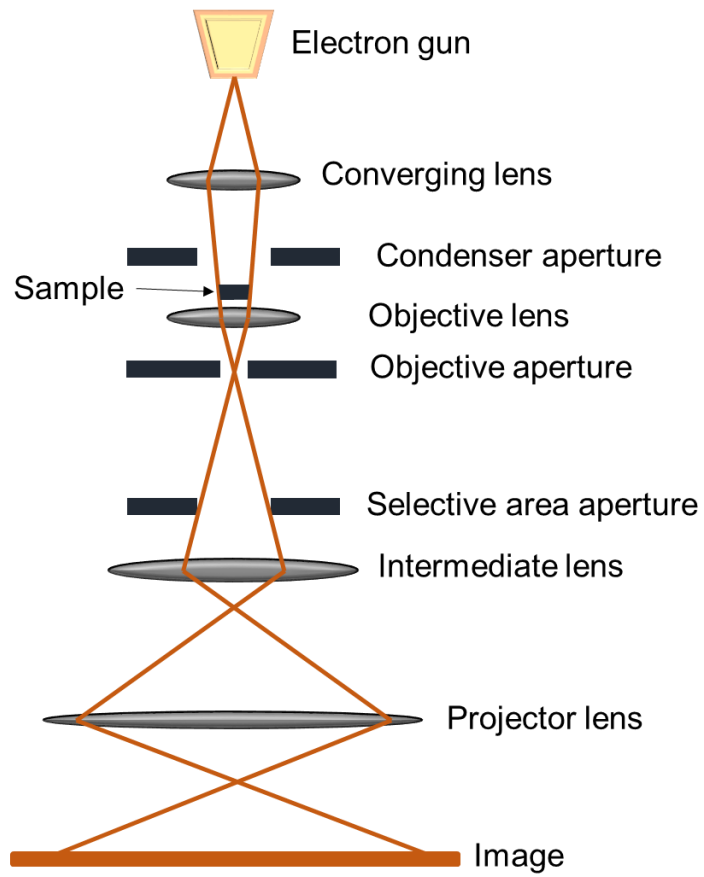


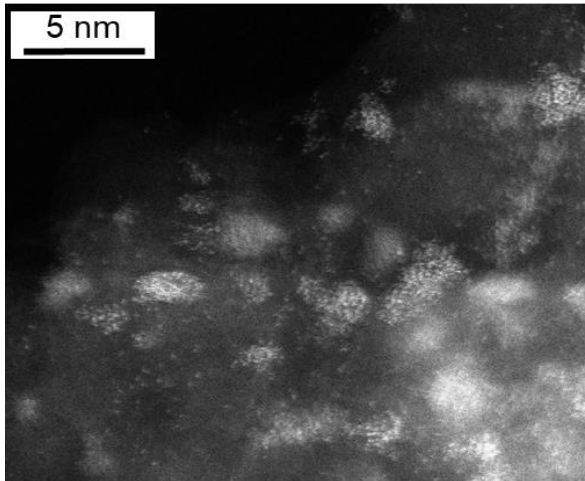
Fig. 2-9 a) Electron beam interaction with the material,

(cont.)

b)



c)



d)

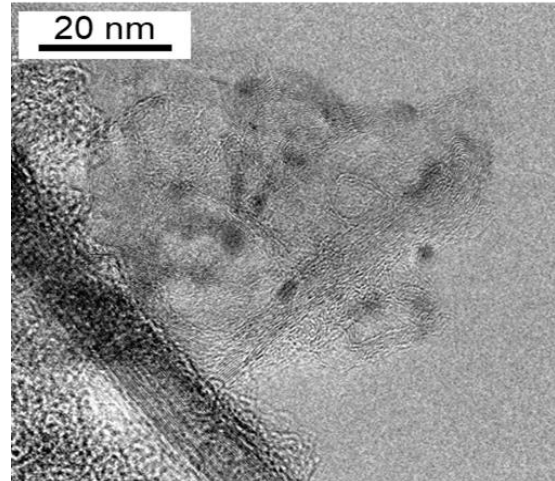


Fig. 2-9 b) Principle and working of the TEM, c) TEM image of SnO₂-graphene composite, and d) HRTEM image of the SnO₂-graphene composite.

2.3.5 X-ray diffraction (XRD)

X-rays are the form of electromagnetic radiation of wavelength ranging from 0.01 to 10 nm. X-rays can be generated by accelerating electrons at a high speed towards the target material and colliding them with the target material. Upon collision of high-speed electrons and target material, the electrons give up their energy after interacting with orbital electrons or nucleus of the target material's atom, the energy given up by electrons after collision/interaction is in the form of photons and heat. The X-ray photons can be categorized as Bremsstrahlung or characteristic X-rays. The characteristic X-rays can be used to identify the particular element. The wavelength of the characteristic X-rays is related to the structure of the electron orbit of the target material's atom.

In the powder diffraction, the characteristic X-rays is utilized. A crystal is made up of a periodic arrangement of the atomic groups with spatial lattices at an interval of several angstroms. Upon incident X-rays with the same wavelength on the crystal, the scattering of X-rays in a specific direction occurs, this phenomenon is known as diffraction of X-rays. The diffraction is atomic arrangement dependant thus the atomic arrangement can be studied on the basis of the diffraction pattern. In absence of atomic order arrangement, such as amorphous materials, the broad scattering peaks appear. As shown in Fig. 2-10 (a), the X-rays of wavelength λ incidents at atomic arrangement plane at an angle θ with respect to atomic arrangement plane with interplanar spacing d . In this, the X-rays are called as incident X-rays and the angle is called as an incident angle. Upon incidence X-ray waves, the part of X-rays get reflected and part of getting transmitted, here, if an angle of incident is equal to the angle of reflectance then it establishes the constructive interference and remains in the phase as the difference between the paths of the waves is equal to the integer multiple of the wavelength of incident X-rays. The path difference between the two waves can be given by $2d\sin\theta$. The Bragg's law gives for constructive interference.

$$2d \sin\theta = n \lambda \quad \dots (2.3)$$

here, n is an integer, the condition is called as Bragg's condition, if followed then diffraction occurs in specific relation and if $\lambda \leq 2d$ then diffraction doesn't occur.

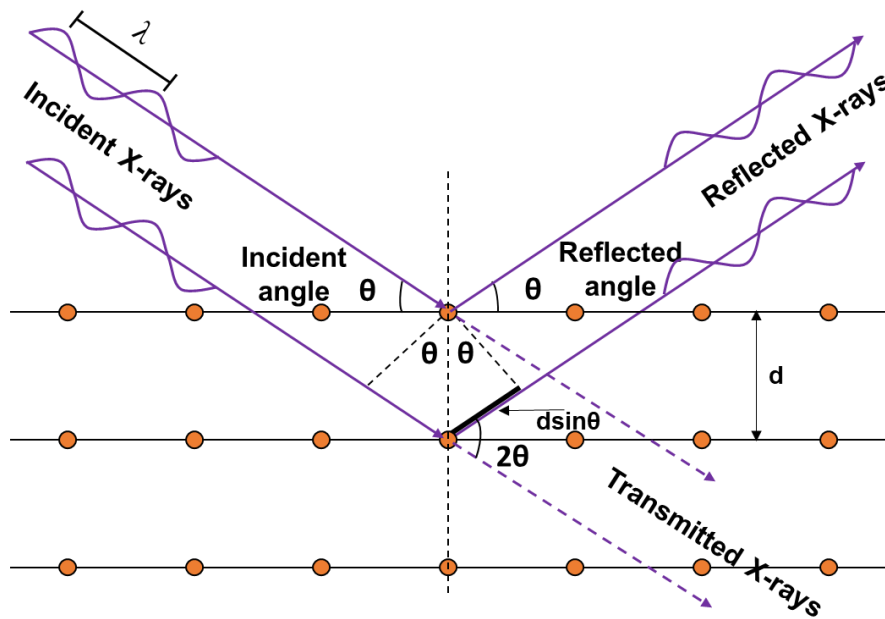
A vast crystallographic data can be generated from the diffraction spectra obtained from the XRD, crystallographic structure analysis and unit cell calculations, quantitative determination of phases by whole-pattern refinement, determination of crystallite size from peak broadening, determination of crystallite shape from peak symmetry to name a few. Phase identification is done by comparing acquired XRD data (peak position and peak intensity) with a data set provided by a Joint Committee on Powder Diffraction Standards (JCPDS)/International Centre for Diffraction Data (ICDD). Crystallite size measurement is carried out on the basis of Scherrer's equation, this equation gives the relationship between the spread of the diffraction line width and the crystallite diameter. Crystallite sizes smaller than 100 nm creates broad diffraction peaks. The Scherrer's equation is given by,

$$D = \frac{(k \cdot \lambda)}{(\beta \cdot \cos \theta)} \quad \dots (2.4)$$

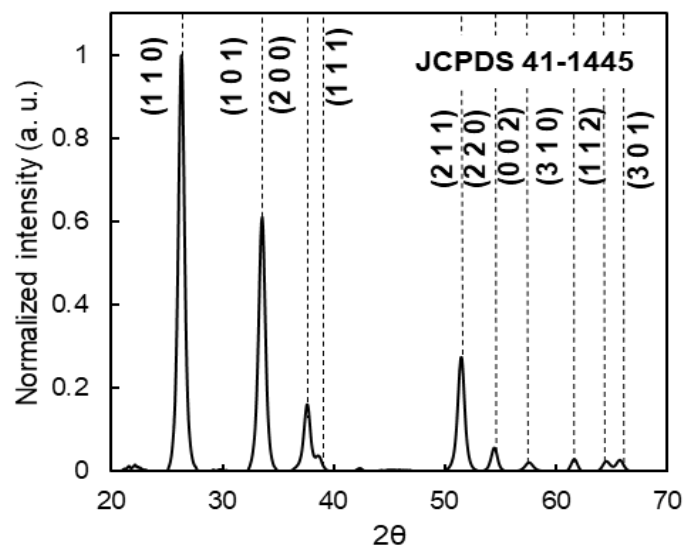
here, D is crystallite size, k is Scherrer's constant, λ is wavelength, β is half the width of diffracted X-ray and θ is Bragg angle.

Figure 2-10 (b) shows the XRD pattern of the SnO₂ obtained by R-AXIS7 FR-E (Rigaku Corporation, Japan) instrument operating at 45 kV and 45 mA using CuK line ($k = 1.54 \text{ \AA}$). The camera length is 70 mm. A mark tube with 0.5 mm outer diameter and 0.01 mm inner diameter was used as a sample holder.

a)



b)

Fig. 2-10 a) Bragg's condition, and b) XRD pattern of SnO_2 .

2.3.6 X-ray photoelectron spectroscopy (XPS)

Considering the future application development based on materials studied in this work, the surface properties of materials were of deep interest. In order to understand the physical and chemical interactions at the material surface, the XPS analysis was carried out. The XPS analysis was used to identify elemental composition, chemical states and electronic states of the elements in the materials.

The principle of the XPS is an effect of the photoemission process (Fig, 2-11 (a)). When an X-ray photon of energy $h\nu$ is bombarded on the atom or molecule, the absorption of X-ray photon takes place, as a result of absorption, a photoelectron gets ejected. The kinetic energy (K.E.) of the ejected photoelectron depends on the energy of the absorbed photon ($h\nu$) and the binding energy of the electron (B. E). The K.E. measurements of ejected photoelectron can reveal elemental composition, their chemical state, and B.E. of the electrons. The B. E. of electron also called as Fermi level in the case of solids depends on several aspects such as kind of element which ejected the electron, the orbital from which electron ejected and the chemical environment (chemical state) of the atom which ejected an electron. During measurement, XPS spectra are obtained by measuring K. E. and number of electrons ejected from zero to ten nanometers of the material surface upon X-ray irradiation. The B.E. of the electrons can be calculated based on measured K.E., the work function ϕ_s as its constant has to be determined beforehand by calibration. Following equation gives the relation between B. E. and K, E. of the electron, known as conservation of energy equation.

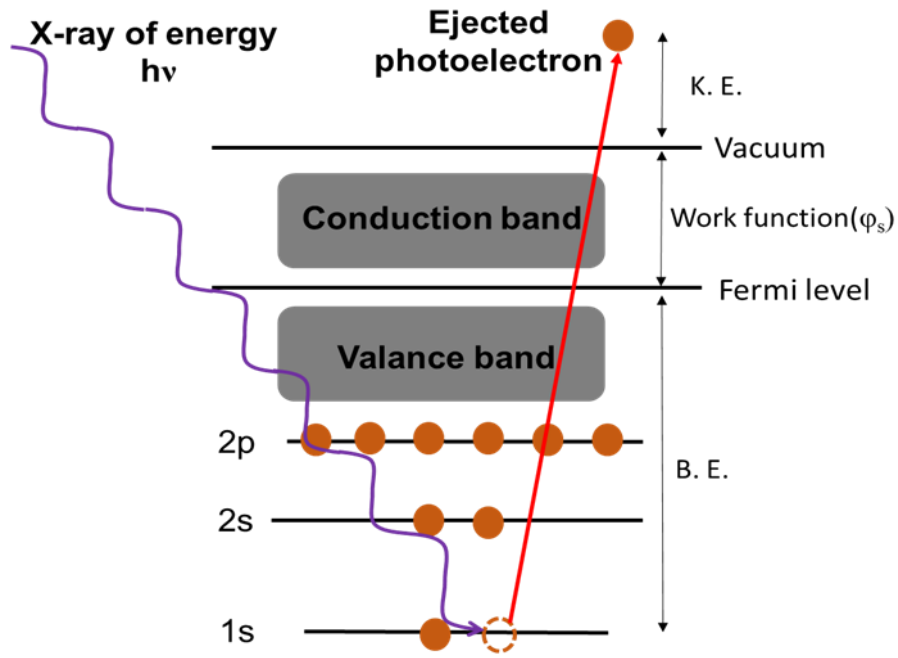
$$\text{B.E.} = h\nu - \text{K. E.} - \phi_s \quad \dots (2.5)$$

There are standard data available in tabular format B. E. values of elements and orbits, it's possible to identify the elements by comparing experimental results with standard data easily. The choice of X-ray sources is based on the energy resolution of the spectrum as X-ray line width directly affects the resolution. Al $K\alpha$ (1486.58 eV) and Mg $K\alpha$ (1253.56 eV) are commonly used.

The XPS studies were performed using Escalab 220i apparatus by VG Scientific and Al $K\alpha$ radiation (photon energy: 1486.6 eV). The angle of out-coming photo-electrons from

the surface was 90 degrees. Spectral data were fitted by an assumption of a peak-line shape of Gaussian-Lorentzian functions with Shirley background subtraction. Figure 2-11 (b) shows XPS spectra of the carbon film. For C 1s peaks, fitted peaks were assigned to O-C=O (288.5 eV), C-O-C (286 eV), C-C (sp^3) (284.8 eV) and C=C (sp^2) (284 eV) bonds.²⁵⁾ Peak positions of C-C (sp^3), C-O-C and O-C=C were fixed by using a position of C-C (sp^3) as standard. After fitting, binding energies of whole spectra were aligned by the shift at correspondence with 284 eV for a fitted position of C=C (sp^2). The C 1s spectrum of carbon film having a high concentration of sp^2 carbon usually have broad and asymmetric tail towards higher B.E along with possible satellite features and in the case of high concentration of sp^3 bonded carbons, C 1s has a symmetric shape with a shift towards higher B. E.

a)



b)

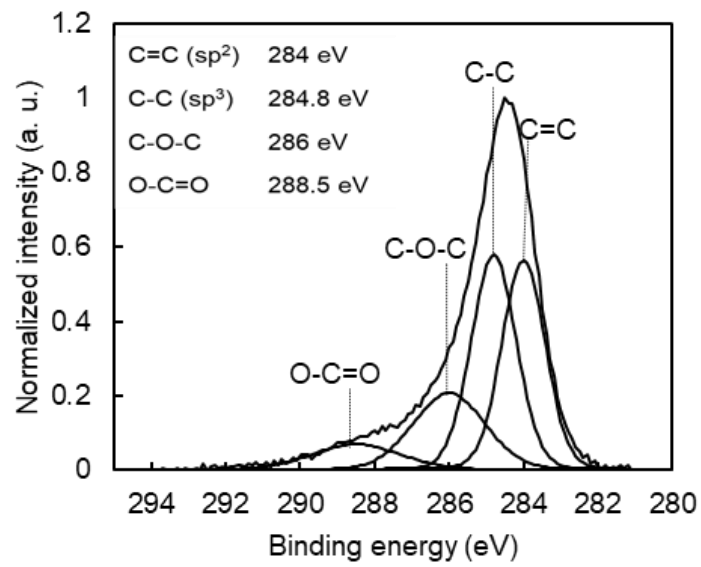


Fig. 2-11 a) The photoemission process (principle of XPS), and b) XPS spectra of the carbon film.

2.3.7 Near-edge X-ray absorption fine structure spectroscopy (NEXAFS)

The NEXAFS offers element specific spectroscopic studies to detect exact bonds in the molecules. The NEXAFS principle is related to the X-ray absorption coefficient depending on the photon energy at a fixed angle of illumination in the photoemission process. When X-rays incident on a material surface, the part of X-rays gets absorbed, the amount of absorption with increasing X-ray energy can reveal edge structures as absorption increases at edge structures. In this case, X-rays need to have enough energy as B. E. of the electron for the excitation of an electron within the material. The small oscillations can be observed overlaid on the edge step. These oscillations get reduced with an increase in the X-ray energy. The oscillations, which occur relatively close to the edge (within about 40 eV) are known as NEXAFS.

In the present study, the carbon films were analyzed using NEXAFS measurement, to quantify the sp^2 -C bonding fraction. The NEXAFS experiments were carried out at the Aichi Synchrotron Radiation Center, Japan, on the beamline 7U with an energy resolution of 0.1eV at the carbon K edge. The NEXAFS spectra were corrected in the total electron yield (TEY) mode, with an energy step of 0.5 eV. The intensity of the incident photon beam (I_0) was measured using a Si photodiode. The absorption signal was given by the ratio of I_s/I_0 , where I_s was the out-coming electron intensity from the sample. Highly oriented pyrolytic graphite (HOPG) was used as a reference sample of 100% sp^2 -C. All the spectra were measured at an incident angle of 54.7° from the sample surface, which is known to be a magic angle to suppress the effects of X-ray polarization. The typical carbon NEXAFS spectra show 2 prominent peaks, centered at 284.8 eV and at 288.4 eV. The peak at 285.0 eV is originated due to the $1s \rightarrow \pi^*$ transition of sp^2 bonded carbon and the peak at 289.0 eV is originated due to the $1s \rightarrow \sigma^*$ transitions of sp^3 bonded carbon.²⁶⁾ (Fig. 2-12). For calculation of percentage (%) of the sp^2 fraction, an estimation was made by the following equation.²³⁾ Spectral intensities A for sample and G for graphite, which was assumed 100% sp^2 carbons, were obtained by integral over an energy range from 280 to 320 eV.

$$sp^2(\%) = \frac{A_{\pi^*}}{A_{\pi^*+\sigma^*}} \div \frac{G_{\pi^*}}{G_{\pi^*+\sigma^*}} \dots (2.6)$$

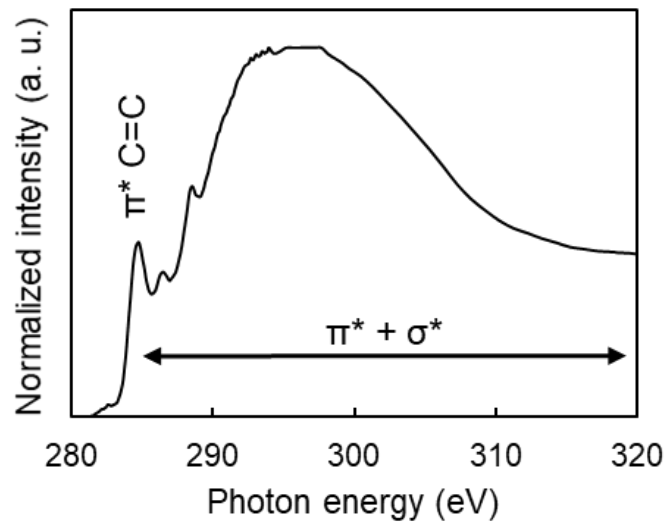


Fig. 2-12 NEXAFS spectra of the carbon film.

2.3.8 Fourier transform infrared spectroscopy (FTIR)

Infrared spectroscopy is the study of interactions between matter and electromagnetic fields in the IR region. IR spectroscopy is a very powerful technique which provides fingerprint information on the chemical composition of the sample. The FTIR spectrometer operates on a principle called Fourier transform.

In the FTIR spectra, the peak position is exploited for qualitative identification as each chemical functional group displays peaks at a unique set of characteristic frequencies. In the present study, the FTIR spectroscopy was probed to study chemical compositions of SnO₂-PANI, SnO₂-graphene composites. Mutual presence of absorbance bands of component materials in an FTIR spectrum was taken as an indication of the formation of the composite. For the measurement of the FTIR spectra, since all the samples in the present study were in the powder form, a KBr method was chosen. Alkali halides become plastic and form a transparent sheet in IR region when subject to pressure. 0.5% sample was mixed in 40 mg fine KBr powder and crushed for about 10 minutes to get a fine powder of mixture and put into die set for pellet formation. A pressure of 22 MPa was applied for 5 minutes to form transparent pellets. The background measurement was carried out using a KBr pellet only.

Figure 2-13 shows the FTIR spectra of SnO₂-graphene composite, a mutual absorbance bands related to SnO₂ and graphene were observed in the composite FTIR spectra.

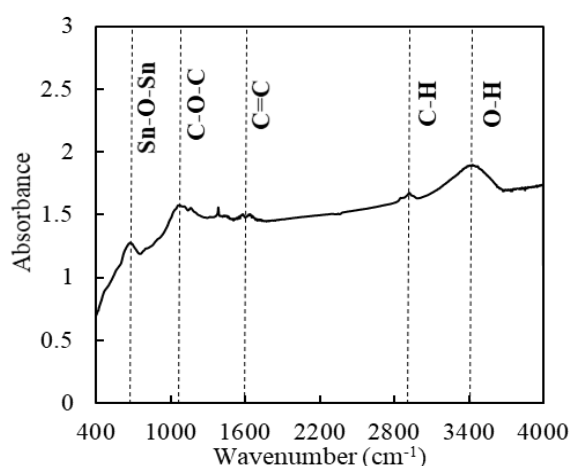


Fig. 2-13 The FTIR spectra of SnO₂-graphene composite.

2.3.9 Raman spectroscopy

In the present research, Raman spectroscopy has been employed for microstructural analysis of carbon materials and composites. Raman spectroscopy is a spectroscopic technique based on Raman effect. Raman effect of Raman scattering is an inelastic scattering of the photon by molecules which are excited to higher vibrational or rotational energy levels. When a monochromatic light (laser) is irradiated on the substance, the laser interacts with molecular vibrations, phonons or other excitations in the system resulting into the shift of energy of laser photons either up or down. In this interaction, Raman scattering has a wavelength different than irradiated monochromatic light. The wavelength difference is associated with the energy content of the molecular vibrations of the substance, Raman scattering with different wavelengths can be obtained from substances with different molecular structures.

Raman spectroscopy is equipped with a light source (laser source), spectrometer and detector. The Raman spectrum consists of a Raman shift (wavenumbers) on the horizontal axis and an intensity on the vertical axis. The Raman shift is a shift in wavenumbers from the excitation wavelength. The peak position, peak intensity, and peak FWHM provide key information about the crystallinity, stress to name a few. Raman spectroscopy is a non-destructive characterization tool with easy sample preparation, however, Raman analysis is a surface analysis tool thus it's important to pay attention towards surface contamination of the samples.

Raman spectroscopy can be used effectively for the microstructural analysis of the crystalline, nanocrystalline and amorphous carbons. The main Raman features of different carbon structures appear in the range 1000 and 1700 cm^{-1} .²⁷⁾ The Raman spectrum is considered to depend on the clustering of the sp^2 phase, bond disorder, presence of sp^2 rings or chains, and the sp^2/sp^3 ratio.²⁸⁾ Raman spectrum of carbon films consisting of three peaks, namely D (1350 cm^{-1}) and G ($\sim 1540 \text{ cm}^{-1}$) and an additional peak around 1188 cm^{-1} . D peak arises due to graphitic disorder and G peak represents the graphitic band.²⁷⁾ The peak around 1188 cm^{-1} can be assigned to mixed $\text{sp}^2 - \text{sp}^3$ bonds. In the case of graphene, the most prominent Raman bands of graphene are the G-band and 2D-band ones appearing at 1580 cm^{-1} and 2700

cm^{-1} respectively. The G-band peak is an indication of a six-membered ring structure in the graphene sheets. The 2D-band peak is also a characteristic peak of the graphene.²⁹⁾ The peaks at 1337 cm^{-1} and 1605.3 cm^{-1} are referred to as D-band and D'-band, respectively. An occurrence of these peaks is due to the structural disorder of six-membered rings. This disorder is mainly from the imperfections in the edge region of the graphene. It has been reported that nanographene domain size can be calculated from the peak parameters of the G band peak and D band peak. The formula for the calculation is stated below.³⁰⁾

$$L_{\alpha} = (2.4 \times 10^{-10}) \lambda_l^4 \left(\frac{I_D}{I_G} \right)^{-1} \dots (2.7)$$

where, λ_l is laser wavelength and I_D and I_G are the integrated intensities of the D band peak and G band peak.

The Raman spectrum of the graphene has been shown in Fig. 2-14. The Raman spectra were acquired using a Renishaw inVia Raman microscope equipped with a 532 nm laser source. The laser was focused on a sample surface with a spot size of around $1 \mu\text{m}$ with the power of 0.5 mW. Spectra were calibrated using reference Si spectra measured at room temperature with a Raman shift of 520.3 cm^{-1} . Detailed study of microstructure was carried out by comparing the Raman spectrum on the basis of intensity, position, and width of the peaks. A curve fitting on the basis of these parameters was carried out.

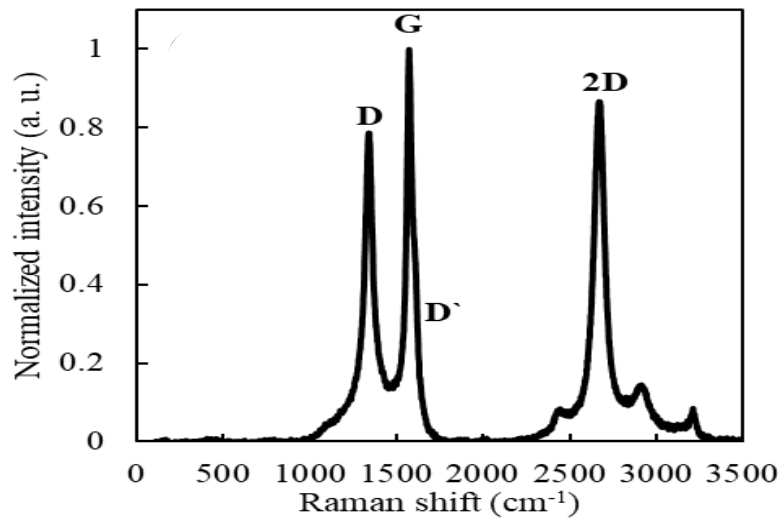


Fig. 2-14 Raman spectra of graphene.

2.3.10 Optical spectrophotometry

A spectrophotometer is a photometer for the measurement of optical properties of the materials as a function of light source wavelength. When exposed to an ultraviolet light source, an energy transition in the molecules occur as a result of absorption of energy. The relation between absorption and wavelength of the light source can distinguish special features and compositions of the materials. In the present study, a spectrophotometer operating in the energy range 200 ~2500 nm was used to study the optical band gap of the materials. For the sample preparation for powder materials, about 1 mg of powders were dispersed using homogenizer for 20 minutes in 8 ml ethanol. The measurement of absorbance was carried out then using formula stated below the absorption coefficient was calculated,

$$A = \log_{10} \frac{I_0}{I} = 0.43\alpha \cdot L \quad \dots (2.8)$$

here, A is the absorbance, α is the absorption coefficient, I_0 is the intensity of the incident light, I is the intensity of transmitted light and L is the path length. The optical band gap was calculated from the absorption coefficient (α). the Tauc gap is an intercept E_g derived from a Tauc plot, which has the quantity $h\nu$ (the energy of the incident light) on the horizontal axis and the quantity $(\alpha h\nu)^{1/2}$ on the vertical axis.

$$\sqrt{\alpha h\nu} = C(h\nu - E_g) \quad \dots (2.9)$$

Figure 2-15 shows the Tauc plot showing $(\alpha h\nu)^{1/2}$ vs. energy, the extrapolation of the straight line to $(\alpha h\nu)^{1/2} = 0$ axis gave the value of band gap of the SnO₂ in the present study.

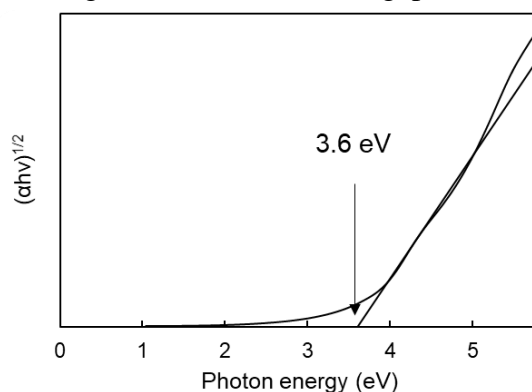


Fig. 2-15 The Tauc plot and the optical band gap of the SnO₂.

2.4 Gas sensing measurements

2.4.1 Sample preparation

An inexpensive approach for the sample preparation for gas sensing measurement was explained as follows. The sample was prepared in the form of pellets to check the response of the materials to the gases.

The synthesized materials (SnO_2 and PANI) were mixed together by grinding using pestle for 20 min. to get as much as uniform mixing of the materials. After the grinding, a free-flowing powder (200 mg) was transferred to stainless steel die set for pellet formation. The powder was placed between two punches in the die set. A pressure of 22 MPa applied for 5 minutes using hydraulic press machine. The inner diameter of pellet die set was 12 mm. The diameter of the pellet formed was 12 mm and thickness was 1.6 mm. These pellets were further used for gas sensing measurements. Figure 2-16 shows the pellets formed by the above method for sensing measurements.

In the case of pellets, there was no control over the surface structure formation as well as the composition of the components on the surface. However, due to cost-effectiveness pellets were utilized for gas sensing measurements.

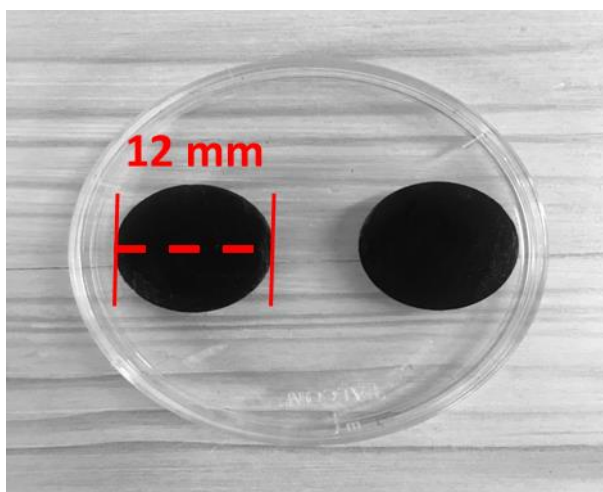


Fig. 2-16 Pellet formation for gas sensing measurement.

2.4.2 Gas sensing set-up

The vast research has been done in the field of gas sensors focusing various aspects and aiming better sensing characteristics, the focus of this has been on three main parts, materials for sensing, the fabrication of sensing devices and sensing principles. Different sensing principles and gas detection methods based on those sensing principles are proposed and developed. Sensors can be classified on the basis of their gas sensing principles/operating method. Out of various gas sensing methods, such as calorimetric methods, acoustic methods, optic methods, methods based on electric variation, methods based on electric variation are the most used methods for gas detection.

In the methods based on electric variations, a change in electrical properties of gas sensing materials is recorded as a response to gas analytes. These methods are simple and require the inexpensive fabrication and set up. In this methods, a sensing material is placed between conducting electrodes to which voltage is applied and the change in electrical properties monitored (resistance, capacitance or conductivity). For this method, metal oxide semiconductors, conducting polymers, nano carbons and moisture absorbing materials are ideal materials for better gas sensing characteristics as the electric properties are very much sensitive to the chemically/physically adsorbed materials on their surfaces.³¹⁾

Since the materials under study in this work are conducting polymer, metal oxide and nanocarbon and their composites, the method based on electric resistance variation as a gas response were utilized. Fig. 2-17 (a) shows the gas sensing set up used in this study. The gas response of the Sn-PANI composite was studied in the controlled atmosphere putting sample (Sn-PANI composite pellet) inside the gas chamber. The gas set up consist of gas measuring chamber made up of glass, a multimeter (Keithley 2000) along with computer, stainless steel base plate providing housings for gas inlet, exhaust system and probes, a pumping system for exhaust and controlling pressure inside chamber, and gas inlet system to purge measurand gas into the gas measuring chamber. The Teflon insulator was used wherever needed, and the silicon rubber gasket was fitted on the base plate to avoid gas leakage. The known volume of measurand gas was purged into the chamber. The gas concentration was calculated from the

known volume of chamber and volume of gas inserted into the chamber. The pellet was mounted on the base and electrodes were connected to the pellet and further connected to the multimeter. The multimeter was interfaced to a computer through RS-232 port and controlled by software provided by Keithley Instruments.

The response of the materials was evaluated on the basis following parameters.

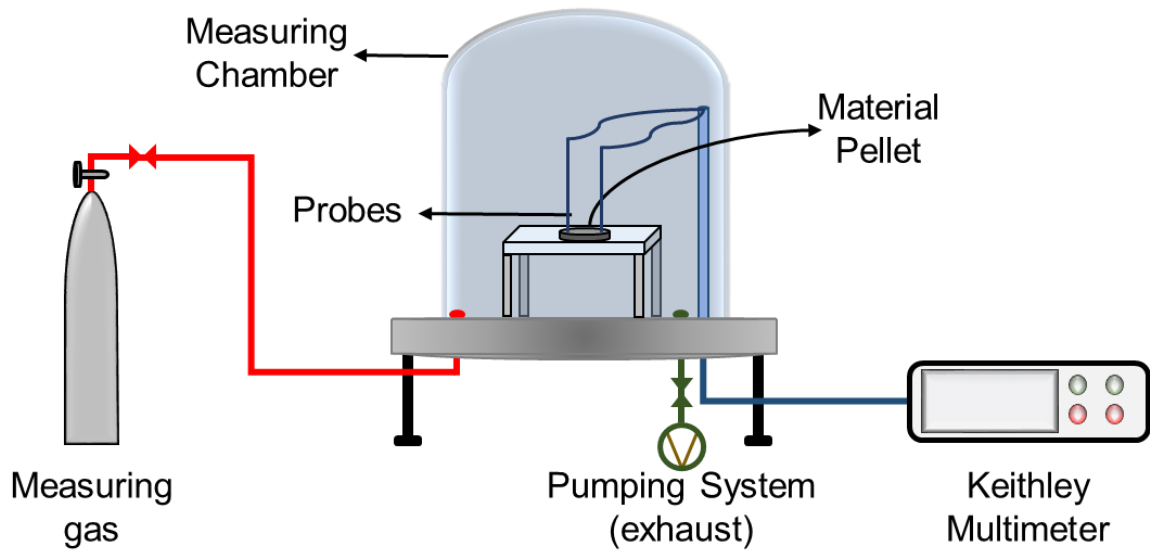
- a) Sensor response (S): The response of gas sensing material can be defined as the measure of change in the output (resistance) with respect to the change in the input (ammonia concentration). In the present work, a sensor response (S) was calculated as the ratio of total resistance change to the initial resistance,

$$\text{Sensor response } (S) = \frac{(R_g - R_a)}{R_a} \quad \dots (2.10)$$

here, R_a is the resistance of the material in the air (absence of gas), R_g is the resistance of the material in presence of gas.

- b) Response time: The response time was taken as a time taken by a sensor to reach to the 90% of saturation value of electrical resistance in presence of analyte gas (ammonia).
- c) Recovery time: The recovery time was calculated as the time taken by the sensor to revert back 90% of the reference value of electrical resistance (resistance in the absence of ammonia). (Fig. 2-17 (b))

a)



b)

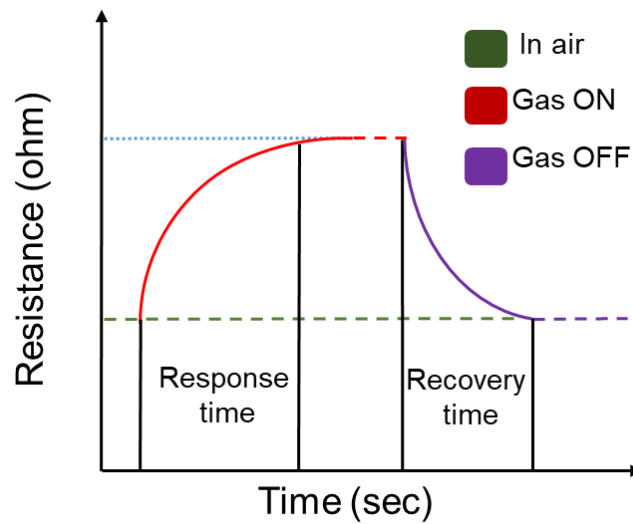


Fig. 2-17 a) The gas sensing measurement set-up in the present study, and b) an illustration for gas sensing parameters.

References

- 1) J. Zhang and L. Gao, *J. Solid State Chem.* **177**, 1425 (2004).
- 2) M. Marikkannan, V. Vishnukanthan, A. Vijayshankar, and J. Mayandi, *AIP Adv.* **5**, 027122 (2015).
- 3) AC. Pierre, *Introduction to Sol-Gel Processing*. New York, Springer (2002).
- 4) S. Thiagarajan, A. Sanmugam and D. Vikraman, *Facile Methodology of Sol-Gel Synthesis for Metal Oxide Nanostructures, Recent Applications in Sol-Gel Synthesis*, IntechOpen (2017)
- 5) L. Xu, X. Li, Y. Chen, and F. Xu, *Appl. Surf. Sci.* **257**, 4031 (2011)
- 6) H. Higashimura, and S. Kobayashi. *Encyclopedia of Polymer Science and Technology, Oxidative Polymerization*, Wiley, 740 (2004).
- 7) I.Yu. Sapurina, and M.A. Shishov, *Oxidative Polymerization of Aniline: Molecular Synthesis of Polyaniline and the Formation of Supramolecular Structures*, *New Polymers for Special Applications*, IntechOpen (2012).
- 8) N. Gospodinova, and L. Terlemezyan, *Prog. Polym. Sci.* **23**, 1443 (1998).
- 9) Y. Wei, X. Tang, Y. Sun, and W. Focke, *J. Polym. Sci., Part A: Polym. Chem.* **27**, 2385 (1989)
- 10) H. Myung, Y. Park, M. Jung, B. Hong, and J. Han, *Mater. Lett.* **58**, 1513 (2004).
- 11) J. Han, *J. Phys. D: Appl. Phys.* **42**, 43001 (2009).
- 12) R.D. Arnell, and P.J. Kelly, *Surf. Coatings Technol.* **112**, 170 (1999).
- 13) D. Monaghan, D. Teer, K. Laing, I. Efeoglu, and R. Arnell, *Surf. Coat. Technol.* **59**, 21 (1993)
- 14) M. Iwasaki, H. Inui, Y. Matsudaira, H. Kano, N. Yoshida, M. Ito, and M. Hori, *Appl. Phys. Lett.* **92**, 081503 (2008).
- 15) S. Takashima, M. Hori, T. Goto, A. Kono, M. Ito, and K. Yoneda, *Appl. Phys. Lett.* **75**, 3929 (1999).
- 16) R. H. Stark and K. H. Schoenbach, *J. Appl. Phys.* **85**, 2075 (1999).

- 17) T. Hagino, H. Kondo, K. Ishikawa, M. Sekine, and M. Hori, *Appl. Phys. Lett.* **5**, 35101 (2012).
- 18) T. Amano, H. Kondo, K. Takeda, K. Ishikawa, M. Hiramatsu, M. Sekine, and M. Hori, *J. Appl. Phys.* **57**, 045101 (2018).
- 19) M. Iwasaki, H. Inui, Y. Matsudaira, H. Kano, N. Yoshida, M. Ito, and M. Hori, *Appl. Phys. Lett.* **92**, 081503 (2008).
- 20) P. J. Bruggeman, M. J. Kushner, B. R. Locke, J. G. E. Gardeniers, W. G. Graham, D. B. Graves, R. C. H. M. Hofman-Caris, D. Maric, J. P. Reid, E. Ceriani, D. Fernandez Rivas, J. E. Foster, S. C. Garrick, Y. Gorbanev, S. Hamaguchi, F. Iza, H. Jablonowski, E. Klimova, J. Kolb, F. Krcma, P. Lukes, Z. Machala, I. Marinov, D. Mariotti, S. Mededovic Thagard, D. Minakata, E. C. Neyts, J. Pawlat, Z. Lj. Petrovic, R. Pflieger, S. Reuter, D. C. Schram, S. Schröter, M. Shiraiwa, B. Tarabová, P. A. Tsai, J. R. R. Verlet, T. von Woedtke, K. R. Wilson, K. Yasui, and G. Zvereva, *Plasma Sources Sci. Technol.* **25**, 53002 (2016).
- 21) R. Smith, D. Wei, and D. Apelian, *Plasma Chem. Plasma Process.* **9**, 1355 (1989).
- 22) H. Conrads, and M. Schmidt, *Plasma Sources Sci. Technol.* **9**, 441 (2000).
- 23) M. Kumar, A. Jawed, and J. Han, *Langmuir* **33**, 2514 (2017).
- 24) K. Shih, and B. R. Locke, *Plasma Process. Polym.* **6**, 729 (2009).
- 25) J. Diaz, G. Paolicelli, S. Ferrer, and F. Comin, *Phys. Rev. B* **54**, 8064 (1996).
- 26) M. Jaouen, G. Tourillon, J. Delafond, N. Junqua, G. Hug, *Diamond Relat. Mater.* **4**, 200-206 (1995).
- 27) J. Schwan, S. Ulrich, V. Batori, and H. Ehrhardt, *J. Appl. Phys.* **80**, 1 (1996).
- 28) A. C. Ferrari and J. Robertson, *Phys. Rev. B* **61**, 14095 (2000).
- 29) A. C. Ferrari, *Solid State Commun.* **143**, 47 (2007).
- 30) M. Pimenta, G. Dresselhaus, M. Dresselhaus, L. Cancado, A. Jorio, and R. Saito, *Phys. Chem. Chem. Phys.* **9**, 1276 (2007).
- 31) X. Liu, S. Cheng, H. Liu, S. Hu, D. Zhang, and H. Ning, *Sensors* **12**, 9635 (2012).

Chapter 3

***Ex-situ* binding of Sn-PANI composites – Synthesis and gas sensing properties**

3.1 Introduction

SnO₂ being most promising gas sensing material for most of the pollutant gases has been studied widely. ¹⁻³⁾ SnO₂ is n-type semiconducting material with direct and wide band-gap of 3.6 eV and possess various physical and chemical properties contributing to its captivating gas sensing characteristics. ⁴⁾ The gas sensors based on SnO₂ required elevated temperature for operations because of easy adsorption of oxygen species on the surface resulting into a decrease in charge carriers at ambient temperature, to avoid this high temperature is needed. ⁵⁾ Due to this, SnO₂ based sensing devices need additional heating assembly for operation and power, increasing operating cost. In addition, the sensor operation at elevated temperatures causes gradual alterations in the SnO₂ properties, which diverge gas sensing properties of the device based on SnO₂ with a period. Therefore, it's really essential to develop a gas sensing device operating at room temperature but having analogous gas sensing properties with SnO₂. ⁶⁾

Gas sensors based on conducting polymers such as PANI is a good alternative to the gas sensing devices based on the SnO₂. ⁷⁾ PANI possesses excellent electrical and electrochemical properties and has been a material of interest for gas sensing application. Polyaniline attracted more researchers due to its high sensitivity, short response time, low cost of fabrication, simple and portable structure and low energy consumption. However, PANI shows some drawbacks also, such as long-time instability, irreversibility, and poor selectivity.

To make use of excellent properties of PANI, its necessary to overcome the drawbacks of PANI based sensors by possible solutions such as doping, or composite formation. ⁸⁾

To overcome the drawbacks of the materials. In the present study, the author focused on the composite formation of SnO₂ and PANI considering the synergetic effect due to composite formation. The composite formation of SnO₂ and PANI has been studied previously by few researchers with various techniques such as incorporating SnO₂ precursors during polymerization of aniline monomer, here called an *in-situ* method or controlled growth of SnO₂ on PANI deposited films to name a few, and have shown excellent gas sensing characteristic to various gases due to synergetic effect and formation of p-n junction between n-type SnO₂ and p-type PANI. ⁹⁻¹³⁾

The author has focused on the *ex-situ* method (mixing of presynthesized SnO₂ and PANI) for the composite formation of SnO₂ and PANI in order to check the applicability of *ex-situ* methods for gas sensing applications (Fig. 3-1). A high concentration of ammonia is dangerous to human health. the sensing of higher concentration of ammonia in the environment is a major concern for preventing hazardous results. ¹⁴⁾ The measurement of humidity and moisture control are some of the leading factors in the case of manufacturing practices, considering this the gas sensing response of Sn-PANI to ammonia and humidity was studied. ¹⁵⁾

In the present study, sol-gel synthesized SnO₂ and PANI were blended together to form composite Sn-PANI by *ex-situ* method. Various analyses were carried out in order to study structural, chemical and morphological properties of component materials and Sn-PANI composite.



Fig. 3-1 *Ex-situ* binding method for composite formation.

3.2 Experimental

3.2.1 Synthesis of PANI

PANI was synthesized by chemical oxidative polymerization of aniline. Acid dopant plays a vital role in altering physical and chemical properties of PANI such as conductivity, solubility, and crystallinity, H₂SO₄ doped PANI synthesized here using ammonium peroxydisulfate (APS) as an oxidizing agent.¹⁶⁾

In the synthesis process, a 0.5M solution of double distilled aniline was made in a distilled water solvent, 1M H₂SO₄ as a dopant was added to the solution and placed in an ice cavity. 0.5 M APS as an oxidizing agent was also added drop by drop to above solution till a black-green turbid solution was obtained. The whole procedure was carried out under constant magnetic stirring for 6 hours at a low temperature, as this reaction was highly exothermic. The precipitate was filtered using gravity filtration method, washed several times with distilled water and then dried at 60° C for 12 hours to obtain a dark green powder. The dark green color of synthesized material is an indicator of the formation of emeraldine salt (ES) form of PANI, which is a conducting in nature.

3.2.2 Synthesis of SnO₂

SnO₂ was synthesized by a sol-gel method.¹⁷⁾ A 0.1M solution of SnCl₂·2H₂O was prepared using a distilled water. The solution was heated at 60°C and stirred for 15 min. With continued stirring, 1M NaOH was added to the solution dropwise until the solution turned the pH of 9. Persistent stirring of the solution with 400 rotation-per-minute (rpm) was carried out at 60°C for another 2 hours. After 2 hours of stirring, the solution changed its color from white to gray indicating the formation of SnO₂. The final product was cleaned several times with water and ethanol to remove impurities and then filtered to obtain a precipitate. The precipitate was air-dried and later, annealed at 400°C for 6 hours.

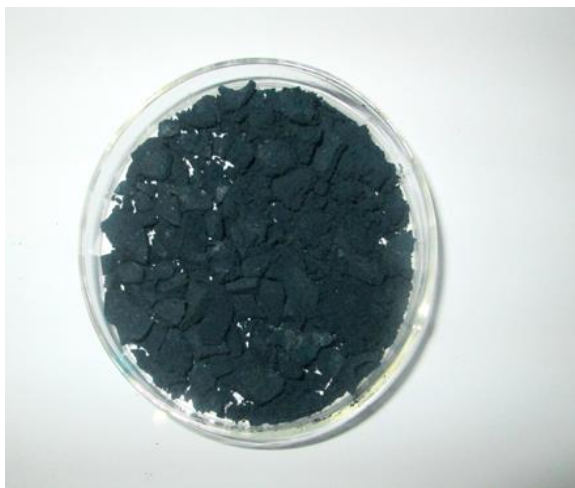
3.2.3 Synthesis of Sn-PANI composite

The composite of SnO₂ and PANI was synthesized by simple blending method, *ex-situ* binding method. A fine powder of SnO₂ and PANI were mixed together in 50:2 weight ratio and ground for 15 minutes with a pestle to get mixture fine mixture of SnO₂ and PANI, further used an Sn-PANI composite.

3.2.4 Pellet preparation

The Sn-PANI composite was used in a pellet form to study the gas sensing response of the Sn-PANI composite. 200 mg composite powder was developed in the form of 12 mm diameter pellet of thickness around 1.5 mm. For the pellet formation, a pressure of 22 MPa applied for 5 minutes using hydraulic press machine.

a)



b)



Fig. 3-2 Actual pictures of as-synthesized materials a) synthesized dark green colored PANI powder, b) tin oxide powder,

(cont.)

c)

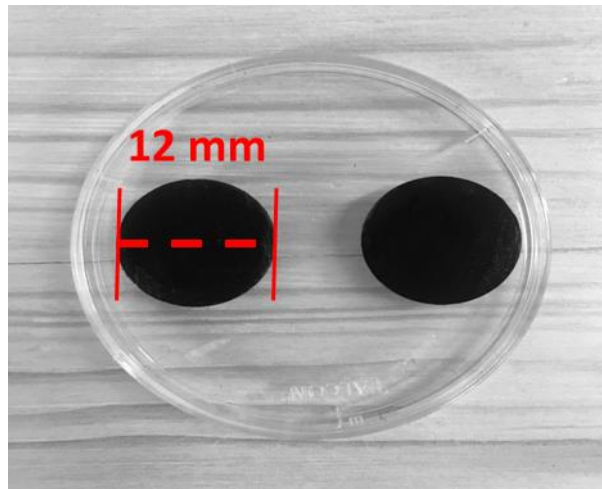


Fig. 3-2 Actual pictures of as-synthesized materials c) pellets of the composite.

3.3 Results and discussion

3.3.1 Surface morphology

Figure 3-3 shows SEM images of the as-synthesized PANI (Fig. 3-3 (a)), SnO₂ (Fig. 3-3 (b)), and composite (Fig. 3-3 (c)). The SEM image of SnO₂ shows irregularly shaped particles with irregular size distribution. The SEM image of PANI shows tubular shaped PANI. In the case of composite surface morphology from Fig. 3-3 (c), well distributed SnO₂ particles in the PANI matrix were observed.

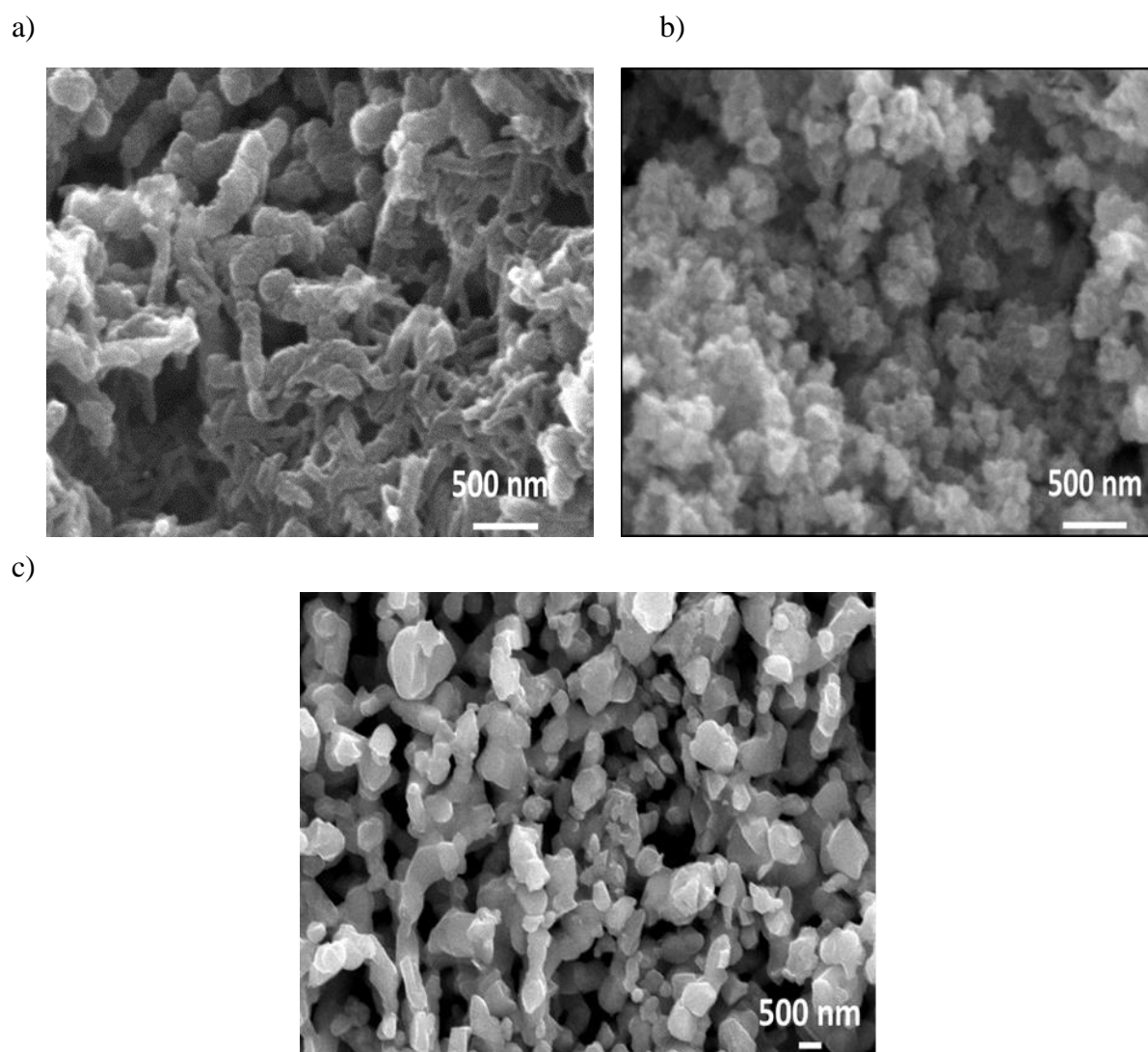


Fig. 3-3 Surface morphology of materials a) PANI, b) SnO₂, and c) composite.

3.3.2 Chemical composition

Figure 3-4 shows FTIR spectra of the composite. The FTIR spectra of Sn-PANI composite consists of characteristic transmittance bands of SnO₂ and PANI. In the FTIR spectra, the band around 668 cm⁻¹ is due to the antisymmetric Sn-O-Sn mode in SnO₂ which confirms the presence of SnO₂ in the composite.¹⁸⁾ The band at 1018 cm⁻¹ is due to C-O stretch, the C=C band appeared at 1461 cm⁻¹ and the transmittance band due to C=N appeared at 1580 cm⁻¹, these are due to the quinoid and benzenoid rings. The peaks at wavenumbers 2853 cm⁻¹ and 2924 cm⁻¹ are due to the C-H mode. These are the characteristic bands of the PANI as reported in the literature.¹⁹⁾ The co-existence of characteristic peaks of SnO₂ and PANI indicated the presence of these materials in the SN-PANI composite.

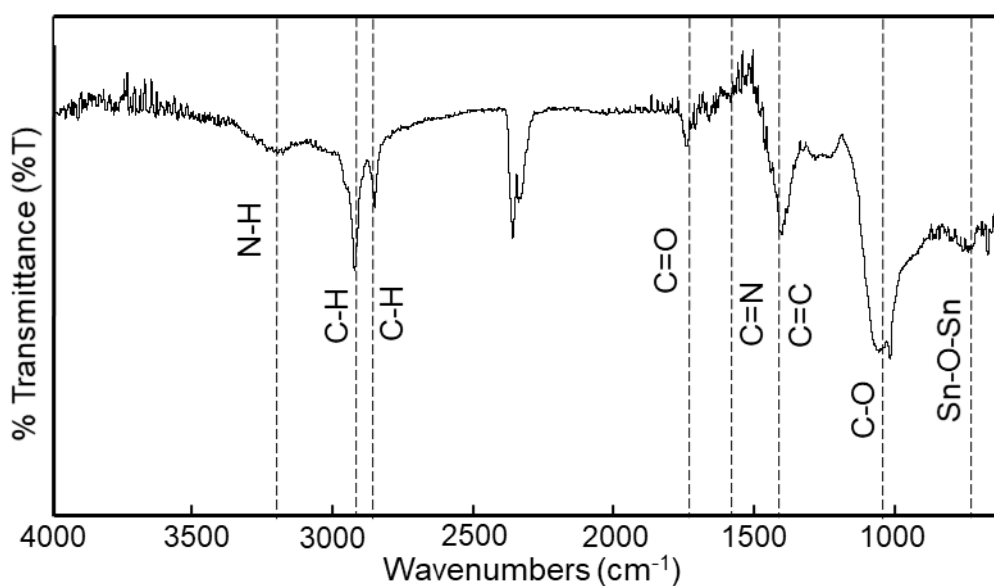


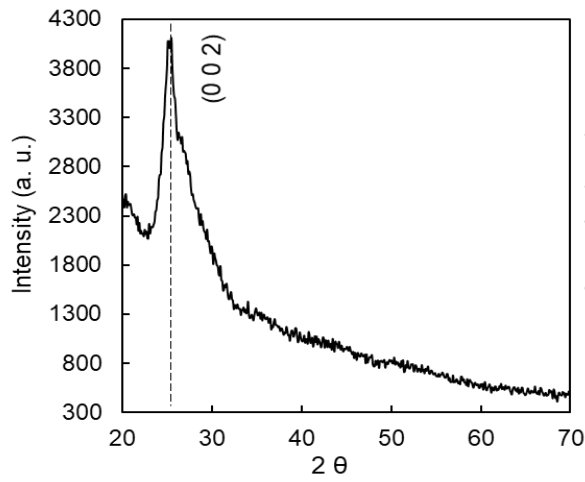
Fig.3-4 FTIR spectra of the Sn-PANI composite.

3.3.3 Crystal structure analysis

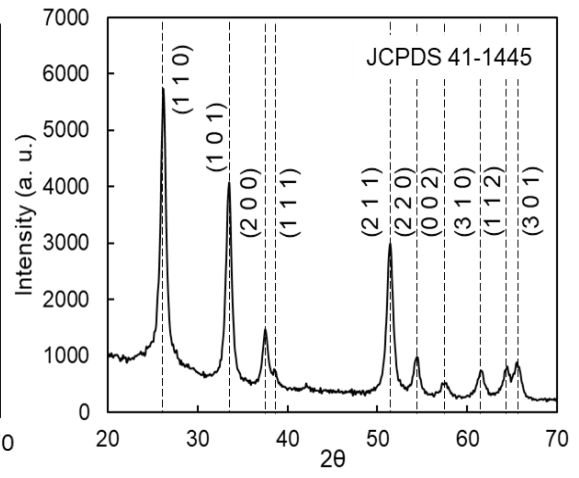
Figure 3-5 shows the XRD spectrum of the PANI (Fig. 3-5 (a)), SnO₂ (Fig. 3-5 (b)) and Sn-PANI composite (Fig. 3-5 (c)). For PANI, the characteristic peak appeared at 26° corresponding to (200) crystal plane. In SnO₂ and Sn-PANI XRD spectra, the peaks associated with tetragonal SnO₂ appeared and matched with those peaks along (1 1 0), (1 0 1), (2 0 0), (2 1 1), (2 2 0), (3 1 0) and (2 0 2) crystal planes, position matched well with (JCPDS File 41-1445).

On comparing the SnO₂ and composite XRD spectra, in the case of the composite, peaks were slightly shifted from their respective standard positions and a diffraction peak representing PANI didn't appear. The crystallite size of SnO₂ found to be 23.75 nm determined by Scherrer's equation, which was also similar in the case of Sn-PANI composite suggesting no crystallographic changes in the materials as a result of *ex-situ* binding of SnO₂ and PANI.

a)



b)



c)

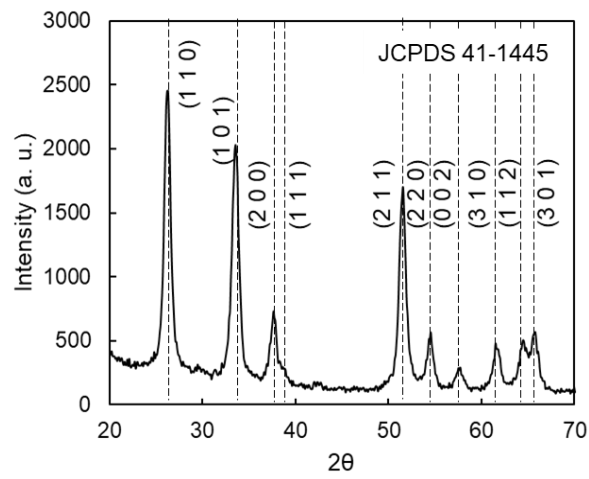


Fig. 3-5 XRD spectra of a) PANI, b) SnO_2 , and c) Sn-PANI composite.

3.3.4 Ammonia sensing properties of Sn-PANI composite

The response of Sn-PANI to the ammonia gas was studied on the basis of change in electrical resistance of the Sn-PANI composite pellet when exposed to ammonia with a period of time. For the gas sensing measurements, the pellet of the composite was placed in measuring chamber, 100 ppm ammonia gas was introduced in the chamber to check the deviation in electrical resistance of the pellet with two probe method. The several gas-sensing cycles were recorded in order to examine the response of Sn-PANI composite to the ammonia at room temperature.

The significant change in the electrical resistance of Sn-PANI composite was recorded using two probe method when it was exposed to ammonia gas as shown in Fig. 3-6. For the first cycle, the initial resistance of Sn-PANI composite was 43 k Ω . When 100 ppm ammonia gas was exposed to the pellet, the resistance of pellet was recorded as 228 k Ω and when pellet was exposed to air, the resistance decreased to 63 k Ω . On repeating sensing cycles with a constant ammonia concentration, it was observed that the initial resistance for each cycle went on increasing and response resistance went on decreasing. The initial resistance could not come back to an initial value (43 k Ω). This could be due to the trapping of ammonia molecules on the surface of the composite. The sensor response of Sn-PANI was observed as 4.32. The response time was about 1.5 minutes and the recovery time was about 15 minutes, the sensor response, response time and recovery times were calculated as described in section 2.4.2. The author thinks the response time and recovery time are not adequate but better than sensors based on PANI.

In another study of ammonia sensing response of H₂SO₄ doped PANI was observed as 0.498 which is less from the sensing response of Sn-PANI composite. In the same study response, time and recovery time were also reported.²⁰⁾ SnO₂ doesn't show any gas sensing response at room temperature. In comparison, Sn-PANI composite has shown better gas sensing characteristics reported data of ammonia sensors based on PANI. The PANI has an important role in the sensing mechanism of the Sn-PANI composite. Due to the synergetic

effect caused by SnO₂ and PANI blending, relatively good sensitivity than reported data of ammonia sensors based on PANI and SnO₂ alone was observed.

The sensing mechanism Sn-PANI is governed by the protonation/deprotonation phenomena. The resistance of Sn-PANI composite increased because of the undoping or the reduction of charge carriers by adsorption of ammonia on the surface of the pellet.²¹⁾ Ammonia gas molecules withdraw protons from N⁺-H sites to form energetically more favorable NH⁴⁺ due to which PANI was changed from the emeraldine salt state to the emeraldine base state, leading to the reduced hole density in the PANI and thus an increased resistance.^{22, 23)}

When the pellet was exposed to air; the reversible nature was recorded. NH⁴⁺ decomposes to form NH₃ and resistance recovered. Due to the physisorption of NH₃ on the pellet surface, the initial resistance couldn't have recovered.^{24, 25)}

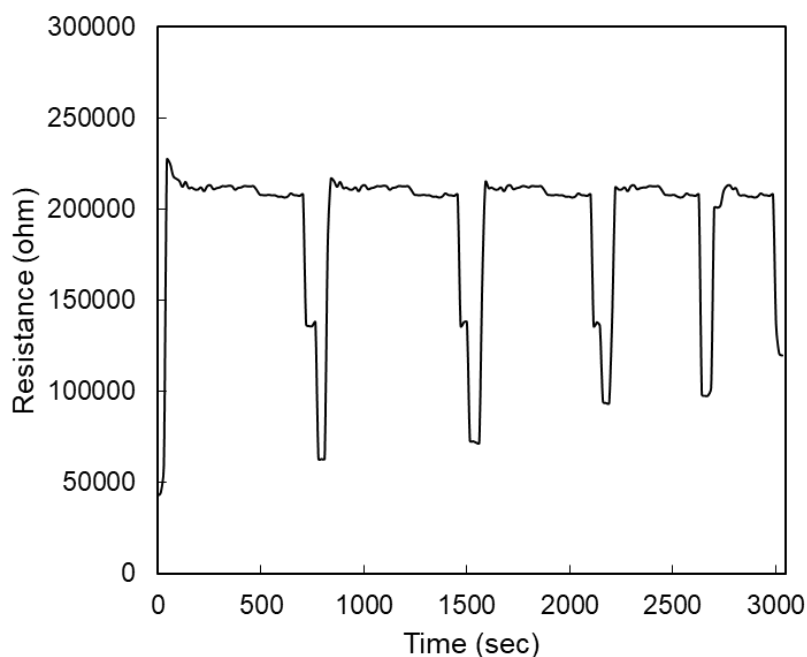


Fig. 3-6 Electrical response of Sn-PANI composite to 100 ppm ammonia.

3.3.5 Humidity sensing properties of Sn-PANI composite

The response of Sn-PANI composite to the humidity was determined as a function of the change in the electrical resistance of the Sn-PANI composite with respect to percent humidity in the measuring chamber. The same procedure as ammonia sensing was followed to check the humidity response of the Sn-PANI pellet. As shown in Fig. 3-7, the significant change in the electric resistance of the Sn-PANI composite was observed.

The humidity response of Sn-PANI is a result of chemo/physisorption of water vapor. The resistance of Sn-PANI pellet decreased as a result of increased humidity and increased with decreasing humidity. This is due to chemically adsorbed water molecules on the surface of Sn-PANI pellet with the formation of hydroxyl groups. These hydroxyl groups are adsorbed on metal cations on the surface and have high charge carrier density and strong electrostatic fields, thus providing protons. Due to movement and the reaction with surface oxygen, protons form another hydroxyl group on the surface.²⁶⁻²⁸⁾ Next, the physical adsorption of the second layer happens to lead to the multilayer formation on the surface of the pellet. Singly bonded water vapor molecules become mobile and form continuous dipoles and electrolyte layers, resulting in a decreased resistance.²⁹⁾ Upon decreasing humidity, the exact reverse effect (increase in resistance) was observed.

The initial resistance of composite was 1.2 M Ω and when the humidity reached its maximum value (90%) the resistance was recorded 51 k Ω . In the case of decreased humidity when humidity was 20% the resistance was recorded 1.1 M Ω . This decreased resistance for 20% humidity might be due to the trapping of water molecules on the surface of composite material.

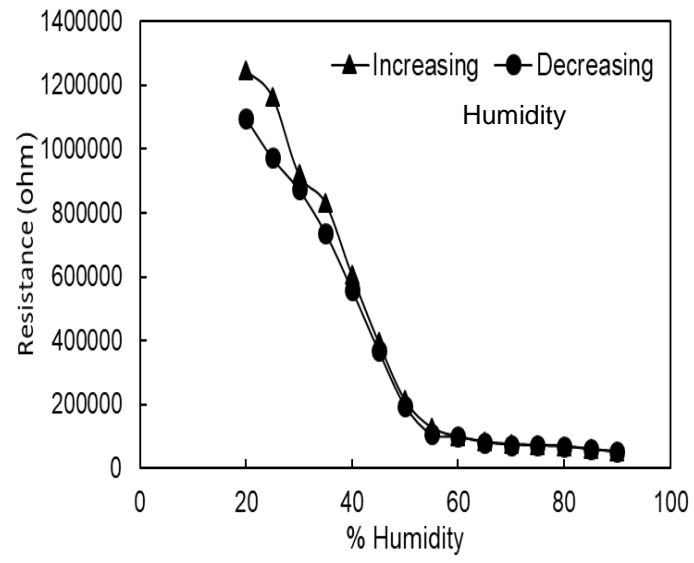


Fig. 3-7 The electrical response of Sn-PANI composite to humidity.

3.4 Conclusion

The *ex-situ* approach for SnO₂-Polyaniline composite formation was used to make Sn-PANI composite. The *ex-situ* approach for Sn-PANI composite found to be an easy method for the composite formation.

The surface morphology of the SnO₂, PANI and Sn-PANI was observed through SEM. The SnO₂ surface contained grains with irregular size and shape, in the case of PANI, tubular shape of PANI was observed. The surface morphology as observed from SEM of Sn-PANI showed distributed SnO₂ in PANI. The crystallographic properties were studied from the XRD. In the Sn-PANI spectra, the peaks related to SnO₂ were slightly shifted from their respective standard positions and a diffraction peak representing PANI didn't appear. The crystallite size of SnO₂ found to be 23.75 nm which was also similar in the case of Sn-PANI composite suggesting no crystallographic changes in the materials as a result of *ex-situ* binding of SnO₂ and PANI. From the FTIR, the mutual existence of SnO₂ and PANI in the Sn-PANI was detected.

Next, the gas sensing responses of Sn-PANI composite to 100 ppm ammonia and humidity were studied. The responses of Sn-PANI to the ammonia gas and humidity were studied on the basis of change in electrical resistance of the Sn-PANI composite pellet when exposed to ammonia and humidity. The Sn-PANI composite showed an excellent response (4.32) to 100 ppm ammonia at room temperature due to the synergetic effect of SnO₂ *ex-situ* binding. However, the author thinks that the response time and recovery time were not suitable for ideal sensor operation. In addition to this, the recovery of the sensor found to worsen with multiple cycles. In the case of humidity response of Sn-PANI composite, it showed a very good response to the low levels (up to 45%) of humidity but for the higher level humidity, the composite showed a low response. The author believes that the adsorption of water molecules on the pellet surface caused a low response to the higher level of humidity. The simple method of *ex-situ* binding method for Sn-PANI composite formation can be used effectively to achieve the higher sensor response but need to improve other parameters.

References:

- 1) J. McAleer, P. Moseley, J. Norris, D. Williams, and B. Tofield, *J. Chem. Soc. Faraday Trans.* **84**, 441 (1988).
- 2) B. Yulianto, G. Gumilar, and N. Septiani, *Adv. Mater. Sci. Eng.* **2015**, 694823 (2015).
- 3) Y. Choe, *Sensors Actuators B Chem.* **77**, 200 (2001).
- 4) E. Tan, G. Ho, A. Wong, S. Kawi, and A. Wee, *Nanotechnology* **19**, 255706 (2018).
- 5) C. Wang, L. Yin, L. Zhang, D. Xiang, and R. Gao, *Sensors* **10**, 2088 (2010).
- 6) N. Deshpande, Y. Gudage, R. Sharma, J. Vyas, J. Kim, and Y. Lee, *Sensors Actuators B Chem.* **138**, 76 (2009).
- 7) I. Fratoddi, I. Venditti, C. Cametti, and M. Russo, *Sensors Actuators B Chem.* **220**, 534 (2015).
- 8) H. Bai, and G. Shi, *Sensors* **7**, 267 (2007).
- 9) C. Rao, M. Vijayan, S. Anwar, D. Jeyakumar, *J. Appl. Polym. Sci.* **124**, 4819 (2012).
- 10) Y. Li, H. Ban, M. Jiao and M. Yang, *RSC Adv.* **6**, 74944 (2016).
- 11) Y. Wang, B. Lei, Y. Hou, W. Zhao, C. Liang, C. Su, and D. Kuang, *Inorg. Chem.* **49**, 1679 (2010)
- 12) F. Gu, S. F. Wang, M. K. Lu, G. J. Zhou, D. Xu, and D. R. Yuan, *J. Phys. Chem. B* **108**, 8119 (2004)
- 13) T. Xiang, Z. Lin, and Y. Qu, *J. Nanosci. Nanotechnol.* **15**, 4493 (2015).
- 14) B. Timmer, W. Olthuis, and A. van den Berg, *Sensors Actuators B Chem.* **107**, 666 (2005).
- 15) Y. Sakai, Y. Sadaoka, and M. Matsuguschi, *Sensors Actuators B Chem.* **35**, 85 (1996).
- 16) A. Fattoum, M. Arous, F. Gmati, W. Dhaoui, and A. Belhadj Mohamed, *J. Phys. D: Appl. Phys.* **40**, 4347 (2007).

- 17) S. Arote, and V. Tabhane, *Indian J. Pure Appl. Phys.* **56**, 7 (2018).
- 18) R. Abruzzi, B. Deavid, and M. Pires, *Cerâmica* **61**, 328 (2015).
- 19) M. Trchová, and J. Stejskal, *Pure Appl. Chem.* **83**, 1803 (2011)
- 20) N. Deshpande, Synthesis and characterization of conducting polyaniline and their derivatives for sensing application of pollutant gases, Doctoral dissertation, S. P. Phule Pune University, India (2016).
- 21) S. Kondawar, S. Agrawal, S. Nimkar, H. Sharma and P. Patil, *Adv. Mat. Lett.* **3**, 393 (2012).
- 22) J. Yue, Synthesis and structure-property relationship of ring-sulfonated polyaniline, Doctoral dissertation, The Ohio State University, US (1991).
- 23) Z. Jin, X. Su, X. Duan, *Sens. Actuators B*, **72**, 75 (2001).
- 24) M. E. Nicho, M. Trejo, A. Garcia-Valenzuela, J. M. Saniger, J. Palacios, and H. Hu, *Sens. Actuators B* **76**, 18 (2001).
- 25) A. Khan, and M. Khalid, *J. Appl. Polym.* **117**, 1601 (2010).
- 26) H. Farahani, R. Wagiram, and M. Hamidon, *Sensors* **14**, 7881 (2014).
- 27) T. Morimoto, M. Nagao, F. Tokuda, *J. Phys. Chem.* **73**, 243 (1969).
- 28) T. Nitta, S. Hayakawa, *IEEE Trans. Components Hybrids Manuf. Technol.* **3**, 237 (1980).
- 29) O. Alhartomy, *Sensors Rev.* **35**, 366 (2015).

Chapter 4

Surface and bulk modifications of magnetron-sputtered carbon films by post treatments of atmospheric pressure plasma

4.1 Introduction

Carbon materials are low cost, abundant in nature and versatile materials. They possess a rich diversity of their structural forms such as i) crystalline form (diamond, graphite, fullerene, ii) amorphous carbon films, iii) carbon nanoparticles, iv) engineering carbons with more or less disordered microstructures based on that of graphite.¹⁾

The diversity of unique properties and versatility of structures in carbon materials arise from their bonding structure as carbon is able to exist in three hybridizations, sp^3 (diamond), sp^2 (graphite) and sp .^{1, 2)} In addition to the ratio of sp^2 (graphite-like) to sp^3 (diamond-like), degree of clustering of sp^2 phase also plays a vital role in the case of physical properties of the carbons.³⁾ Thus, in order to utilize carbon materials for various applications efficiently, to control structural properties of carbon materials by controlling sp^2/sp^3 ratio and degree of clustering of sp^2 phase desirably and effectively needs to control an optical band gap and electrical conductivity for photovoltaic solar cells and gas sensing applications.⁴⁾ The ratio of sp^2 and sp^3 in the carbon film is governed by deposition techniques and on the process parameters during the deposition.⁵⁾ A range of deposition techniques has been developed to deposit carbon films. The most common industrial process is the magnetron sputtering enabling adaptable and precise control of the microstructure and properties of the film.⁶⁾ Film structures are strongly correlated with the plasma density of magnetron sputtering as plasma properties,

the degree of plasma confinement, ion energy, plasma density, plasma temperature, substrate temperature, and substrate position are the key parameters for controllable film deposition.⁷⁾ Furthermore, the structure control techniques such as heat treatment, reactive ion bombardment, polishing, low pressure/temperature plasma are proposed by many researchers. Atmospheric pressure plasma (APP) treatment can be employed to control/alter surface structural properties effectively.⁸⁾ Constituents of plasma (ions, radicals, UV light) play a very essential role in the modification of properties of the materials by changing surface morphology, microstructures, and compositions. The APP treatment was reported for its simplicity and the numerous advantages for modification of surface properties.^{9, 10)} For carbon materials, there are reported advantages such as adhesion improvement of glassy carbons, modifying hydrogen storage properties of carbon nanotubes, increasing the surface energy of carbon fibers.¹¹⁻¹³⁾ The author employed the Ar APP surface treatment to promote the chemical modification of materials.

The aim of this study to discuss in detail the structure control process of magnetron sputtered carbon films and the effect of structure control on optical and electrical properties of carbon films. The films were deposited by CFUBM process by varying power density and treated by post APP treatments. The effect of structure control on film's optical and electrical properties was analyzed by optical spectrophotometry and current-voltage (IV) measurements.

4.2 Deposition of carbon films

Amorphous carbon films were deposited on the substrate by the CFUBM magnetron sputtering process. The background pressure in the sputtering chamber was maintained at 3×10^{-5} Torr before introducing sputtering gas of Ar gas with a flow rate of 80 sccm (working pressure: 6×10^{-3} Torr). The glass substrate with a size of 20-mm²-squared shape was placed in a rotary sample holder at the center of the chamber (Fig. 4-1). The graphite targets with a total area of 80 cm² were applied by a radio-frequency (rf) power. The films were deposited with various discharge powers (1200, 1600 and 2000 W) for different power density values (15, 20, and 25 W/cm²). The film thickness was controlled at a constant of 120 nm by the deposition time. The glass substrates were cleaned ultrasonically in a mixture of acetone and alcohol prior to deposition.

The optical properties were measured using a spectrophotometer (V670, JASSO) in the ultraviolet-infrared spectral range, 200 - 2500 nm. Sheet resistances were measured at room temperature by 4 probe method using source-measure-units (Agilent B2901). The distance between each probe was set at 1 cm.

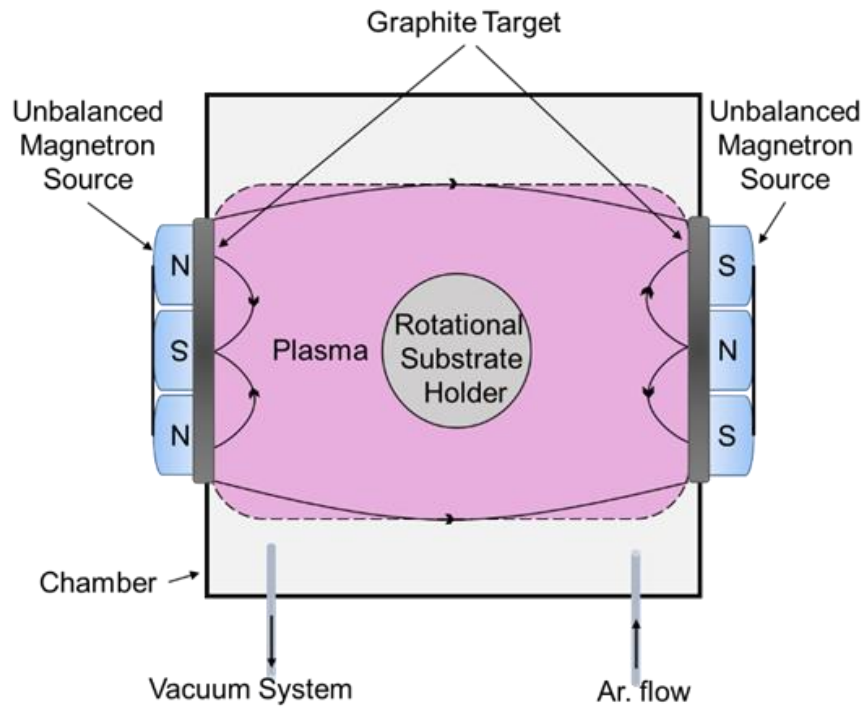


Fig. 4-1 The schematic of closed field unbalanced magnetron sputtering system.

4.3 Effect of power density variation on carbon films

4.3.1 Deposition rate

The effect of power density variation on the deposition rate is shown in Fig. 4-2. An increase in deposition rate with increasing power density was observed. The observed increase in deposition rate suggests the enhancement in Ar ion bombardment on the target resulting in increasing sputtered species with the rise in power density, which is characteristic of CFUBM magnetron sputtering process. The magnetic field lines between the magnetrons form a closed trap for electrons in the plasma. Few electrons, therefore, lost to the chamber walls and dense plasma is maintained in the substrate region, leading to high levels of ion bombardment.¹⁴⁾

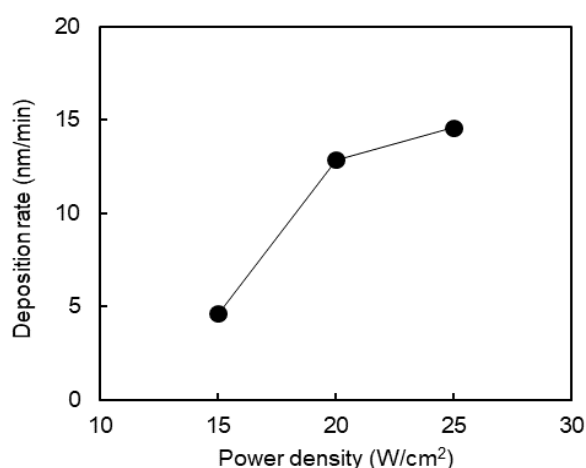


Fig. 4-2 A relation between the deposition rate of carbon films and power density during deposition.

4.3.2 Surface morphology

Surface morphology of as-deposited films with varying power density was observed by SEM. Figure 4-3 (a-c) represents SEM images of the films. No change in the surface morphology was observed as an effect of power density variation.

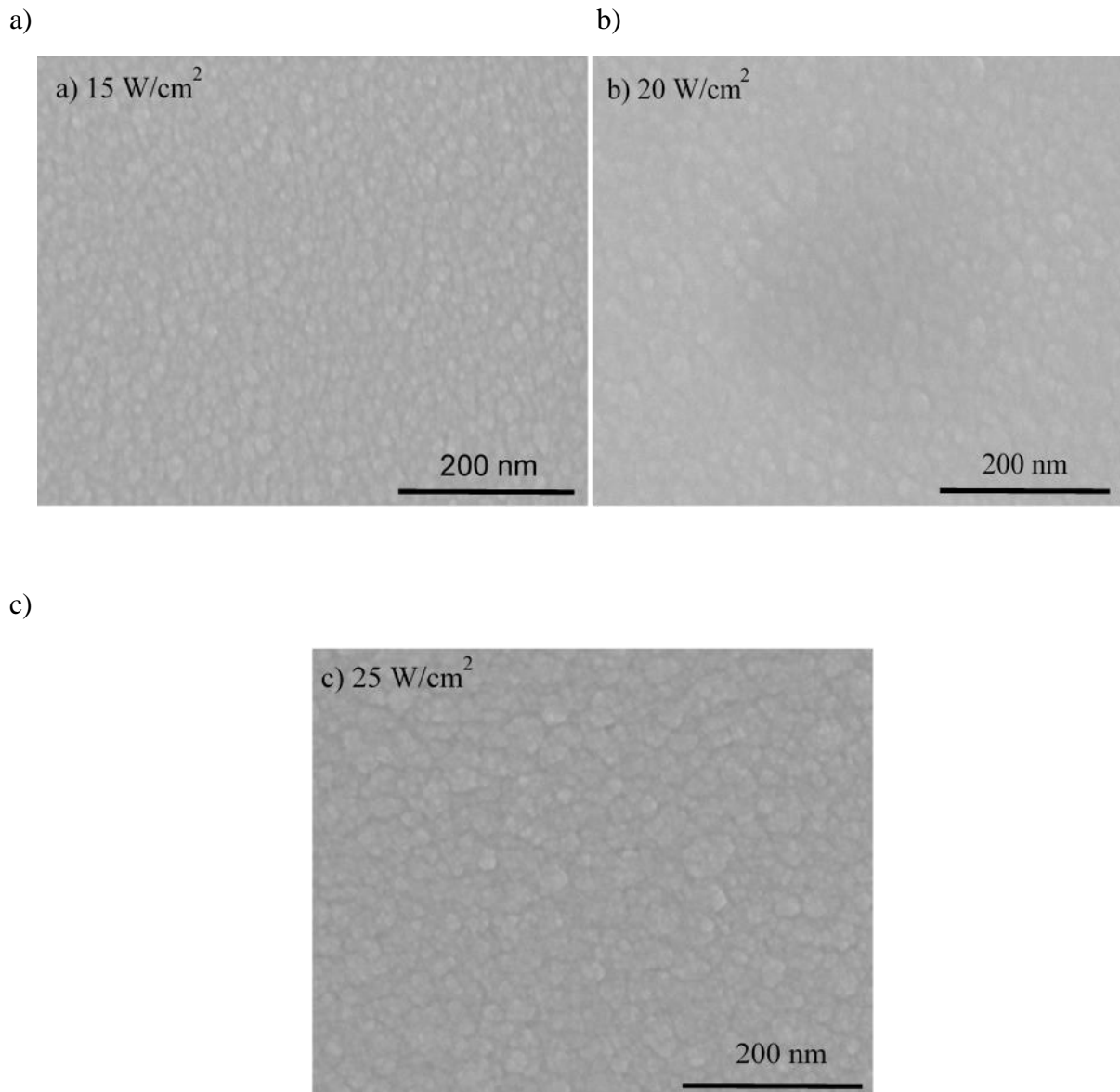


Fig. 4-3 The surface morphology (SEM image) of as-deposited films with varying power density. (a) 15 W/cm², (b) 20 W/cm², and (c) 25 W/cm².

4.3.3 Microstructure of carbon films

Raman spectrum was recorded to check the effect of power density variation on film's structural properties. Figure 4-4 (a) represents the recorded Raman spectrum for films deposited by varying power density.

Raman spectrum of carbon films consists of three peaks, namely D (1350 cm^{-1}) and G ($\sim 1540\text{ cm}^{-1}$) and an additional peak around 1188 cm^{-1} . D band peak arises due to graphitic disorder and G band peak represents the graphitic band.¹⁵⁾ The peak around 1188 cm^{-1} can be assigned to mixed $\text{sp}^2 - \text{sp}^3$ bonds.¹⁶⁾ The detailed study of Raman spectra based on peak intensity, position, area, and width can give insights of chemistry and structure of carbon films as these parameters are closely related to density, size, and structure of sp^2 clusters.¹⁷⁾ To determine two spectral components, a curve fitting on the basis of the above parameters was conducted and the results are shown in Fig. 4-4 (a). An upshift in position (Fig. 3-4 (b)) and a decrease in FWHM (Fig.4-4 (c)) of G band peak was observed with increasing power density, which is representing the crystallographic change. The increase in D band peak area was observed with increasing power density (Fig. 4-4 (d)). Increases in peak intensity ratio (I_D/I_G) and in peak area ratio (A_D/A_G) with increasing power density were also observed (Fig. 4-4 (e)). The G band peak intensity was constant with varying D band peak intensity. The changes in D band peak area, peak intensity area, and peak area ratio can be attributed to increase in number and clustering of sp^2 sites and further supported by the three-stage theoretical model proposed by Ferrari to interpret Raman studies of carbons. In stage 2 of this model, the upshift of G band peak position and increase in peak intensity ratio (I_D/I_G) was associated with ordering and increase of sp^2 sites.³⁾ Observed rise in sp^2 sites is the result of the dependence of the film deposition process on power density. In a CFUBM sputtering system, the high-density plasma can be generated by increasing power density.²¹⁾ The graphitic cluster formation in the high-density plasma resulted in the deposition of sp^2 cluster rich film.

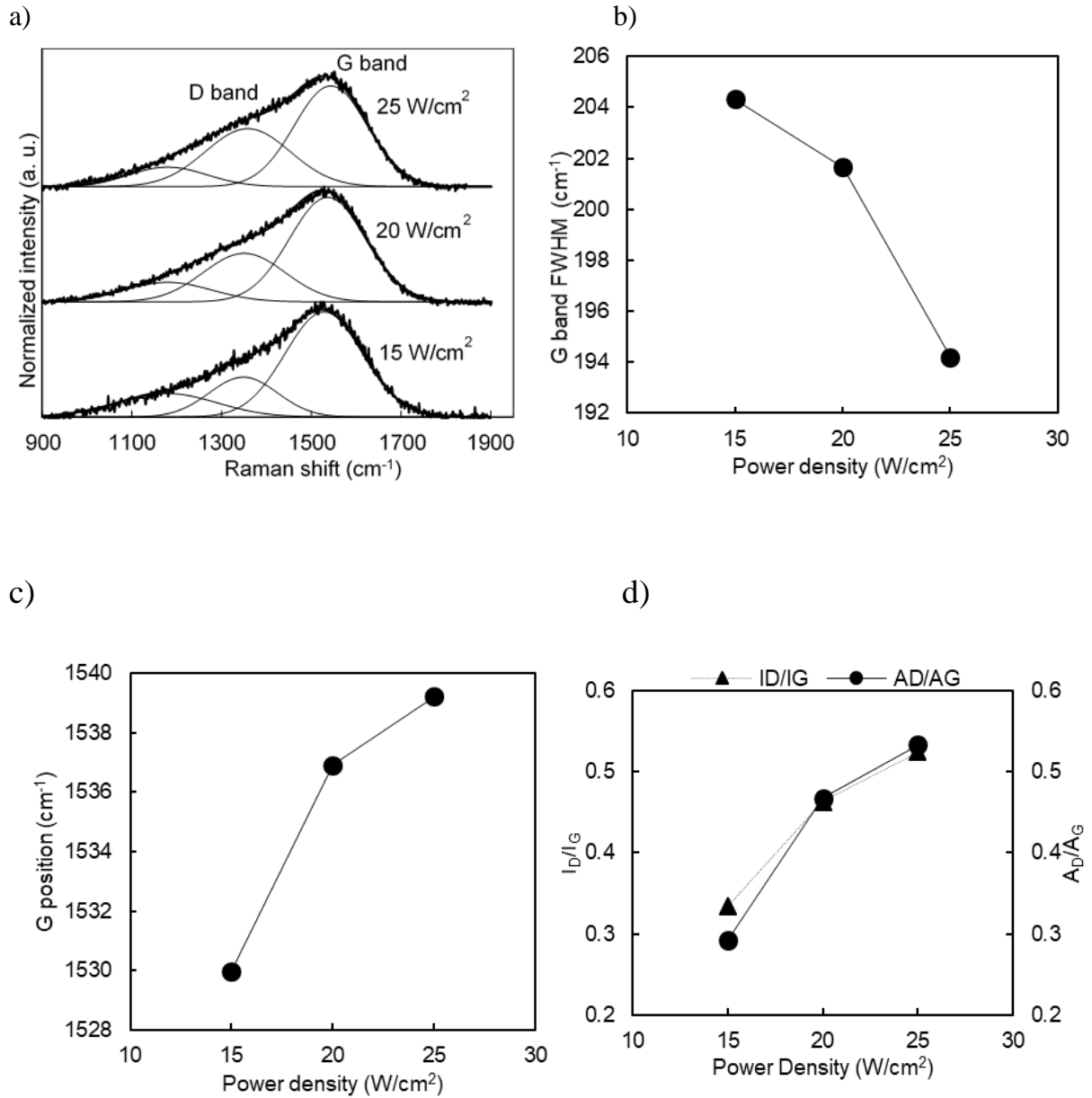


Fig. 4-4 Effect of power density variation on the microstructure of carbon films (a) Raman analysis spectrum, (b) FWHM of G band peak vs. power density. (c) The position of G band peak vs. power density. (d) Peak intensity & peak area ratio vs. power density,

(cont.)

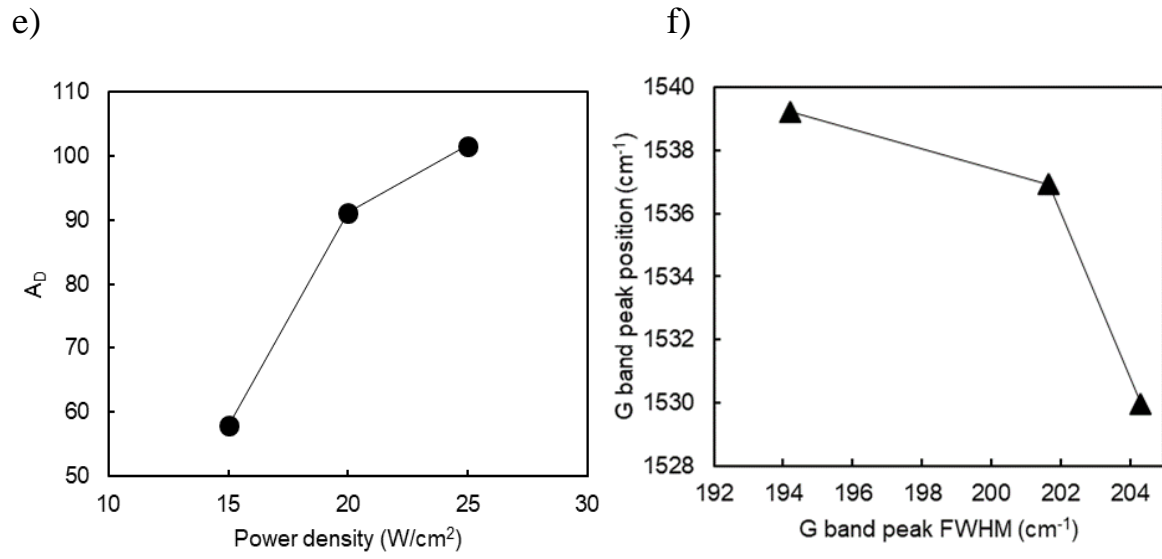


Fig. 4-4 Effect of power density variation on the microstructure of carbon films (e) Area under D band peak vs. power density, f) G band peak position vs. G band peak FWHM.

4.3.4 Optical and electrical properties of carbon films

An effect of structure control on film's optical and electrical properties was studied by evaluating the influence of power density variation on the optical band gap (E_g) and a sheet resistance of carbon films. The absorbance of films was recorded by using an optical spectrophotometer. Based on measured absorbance, the absorption coefficient was calculated. Figure 4-5 (a-c) plots a Tauc plot showing $(\alpha h\nu)^{1/2}$ vs. energy for the film deposited by power density 15, 20 and 25 W/cm² plotted using Tauc relationship respectively. Figure 4-5 (d) shows a decrease in optical band gap with increasing power density. In addition, electrical measurements of as-deposited films were performed using the four probe method. Sheet resistance was calculated from the measured data. Figure 4-5 (e) represents the sheet resistance of the as-deposited films with varying power density. The sheet resistance of the films decreased with increasing power density. Observed optical band-gap narrowing and a decrease in sheet resistance were closely associated with the graphitic nature of the film with high sp² clusters.

As confirmed from Raman analysis, increasing power density induced the formation of the sp² rich film resulting in a decrease in optical band gap and a sheet resistance of the films.

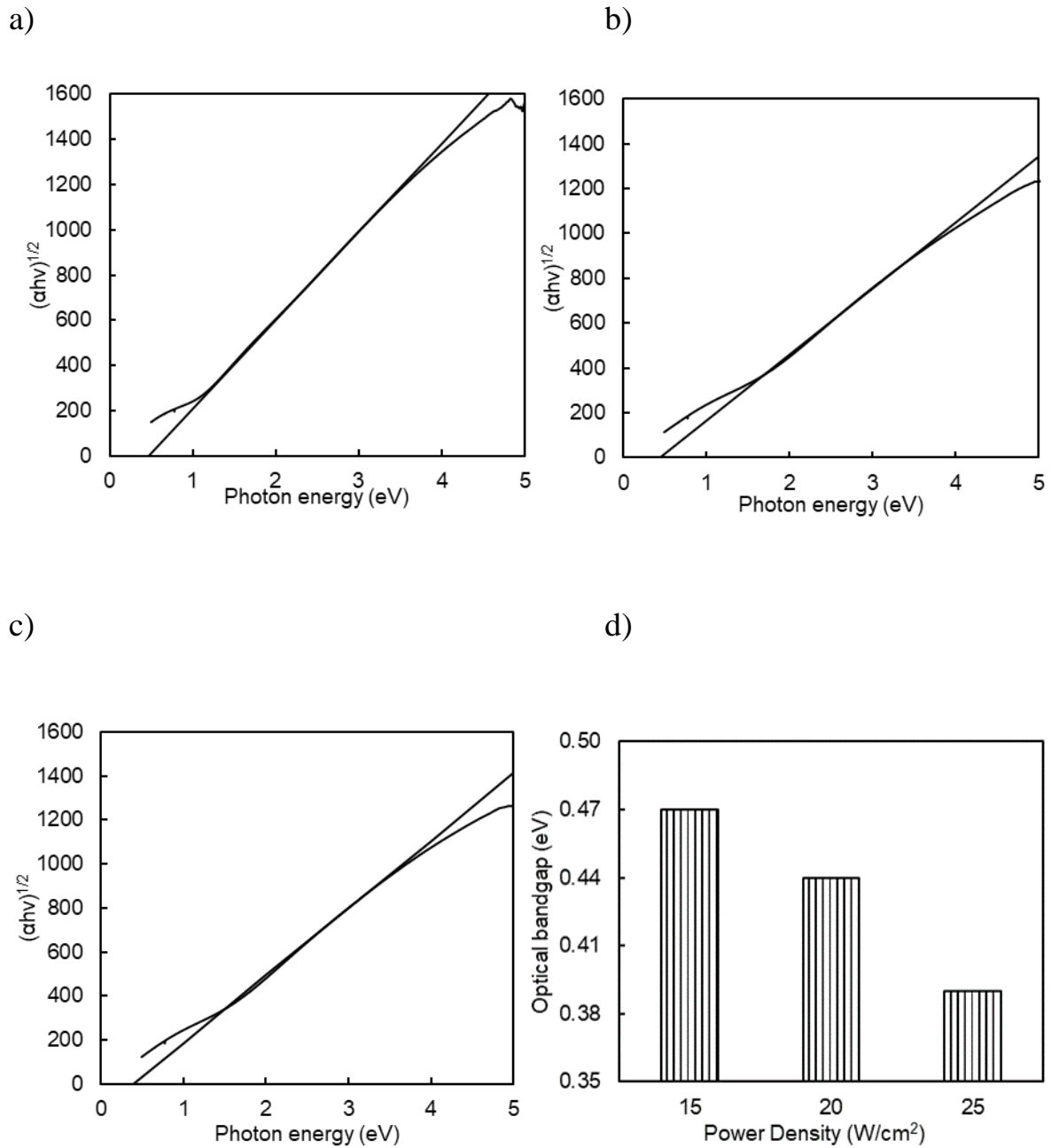


Fig. 4-5 a) Tauc plot of the film deposited by 15 W/cm^2 , b) Tauc plot of the film deposited by 20 W/cm^2 , c) Tauc plot of the film deposited by 25 W/cm^2 , d) Optical band gap vs. power density,

(cont.)

e)

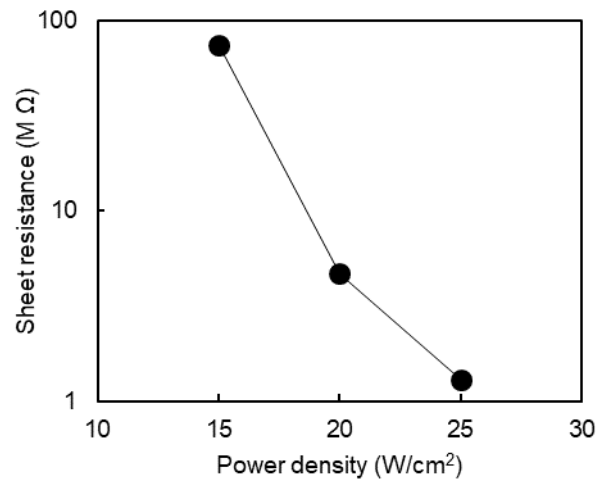


Fig. 4-5 e) Sheet resistance vs. power density.

4.4 APP post-treatments of as-deposited carbon films

As deposited films (power density: 25 W/cm^2 , thickness: 180 nm, size: 10 mm x 10 mm) were treated by the APP operated with Ar gas flow of 2 slm. The High voltage of 60-Hz alternative current was applied with a voltage of 9 kV to the APP source. The substrate to source distance was maintained at 3 mm (Fig.4-6). The plasma treatment was uniform for the entire film surface by scanning. The effect of plasma exposure time was studied by varying treatment time (1, 3, 4 and 5 minutes).

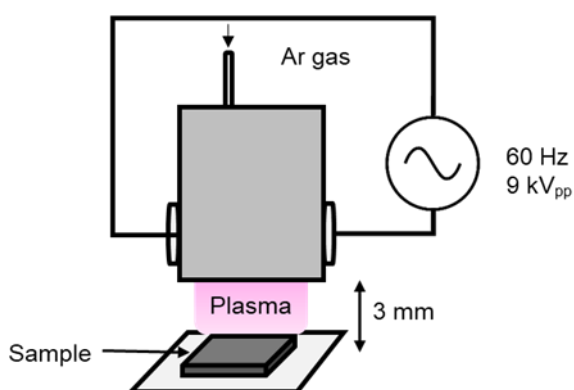


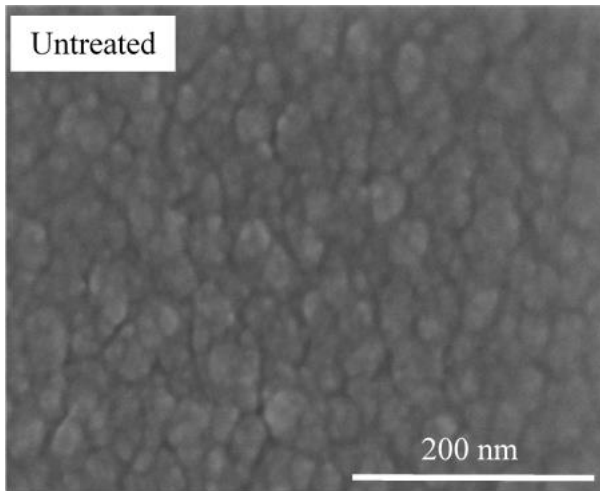
Fig. 4-6 Schematic of atmospheric pressure plasma treatment.

4.5 Effect of APP post-treatments on carbon films

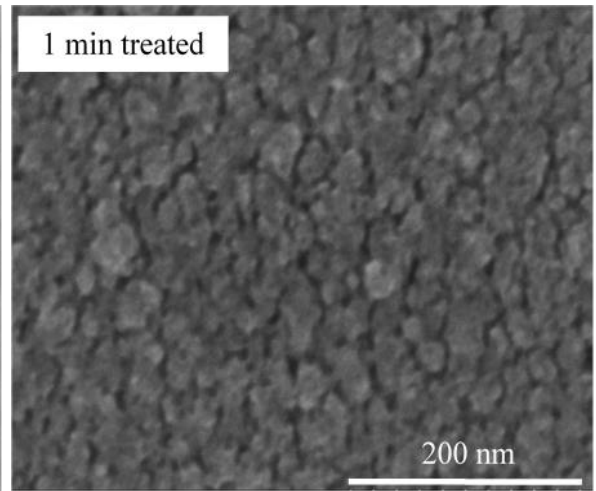
4.5.1 Surface morphology

An effect of post APP treatment on surface properties of carbon films was studied. Figure 4-7 shows the SEM image of plasma untreated film (Fig. 4-7 (a)) followed by plasma treated films with varying treatment time for 1, 4 and 5 minutes (Fig. 4-7(b-d)). APP caused a change in surface morphology of the films effectively. This is due to removing a part of the film by Ar APP treatments. Notably, cavities between neighboring grains were increased with the APP treatment time, resulting in a formation of ordered grains. Change in grain density was measured as a function of the APP treatment time by calculating a number of grains per unit area (200 nm x 200 nm) from the SEM micrographs. From Fig. 4-7 (e), the grain density was decreased with increasing treatment time. From these results, the author believes that due to the APP treatment, an etching of a disordered part around the well-ordered carbon grains took place.

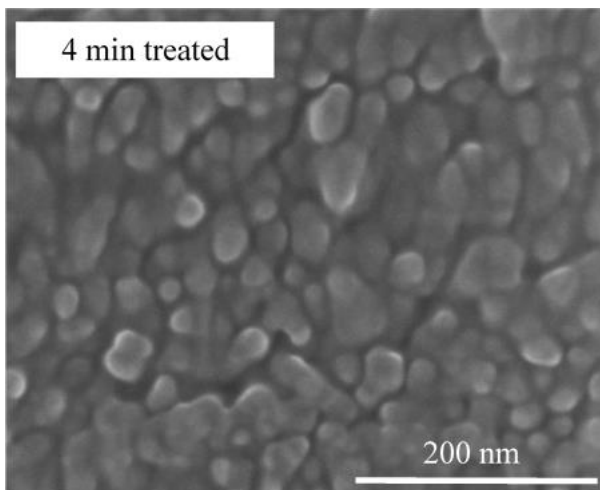
a)



b)



c)



d)

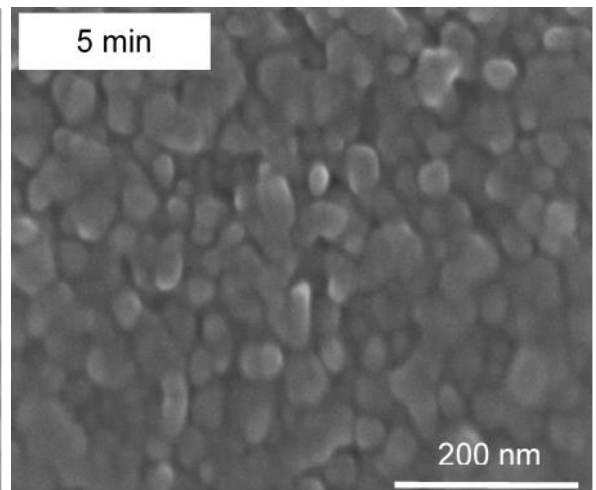


Fig. 4-7 Surface morphology of plasma treated films (a) untreated (b) 1 min. treated (c) 4 min. treated (d) 5 min. treated,

(cont.)

e)

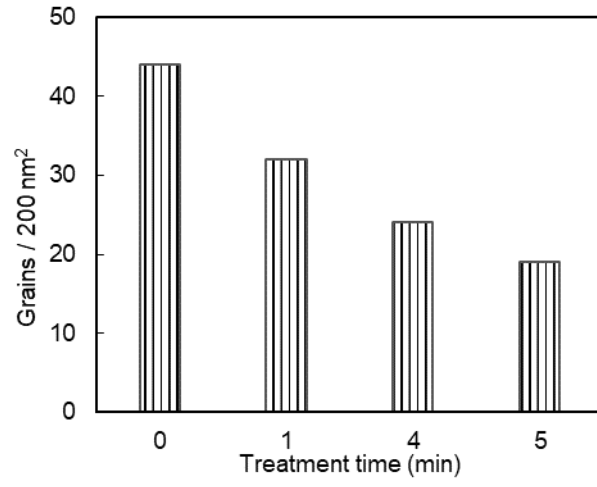
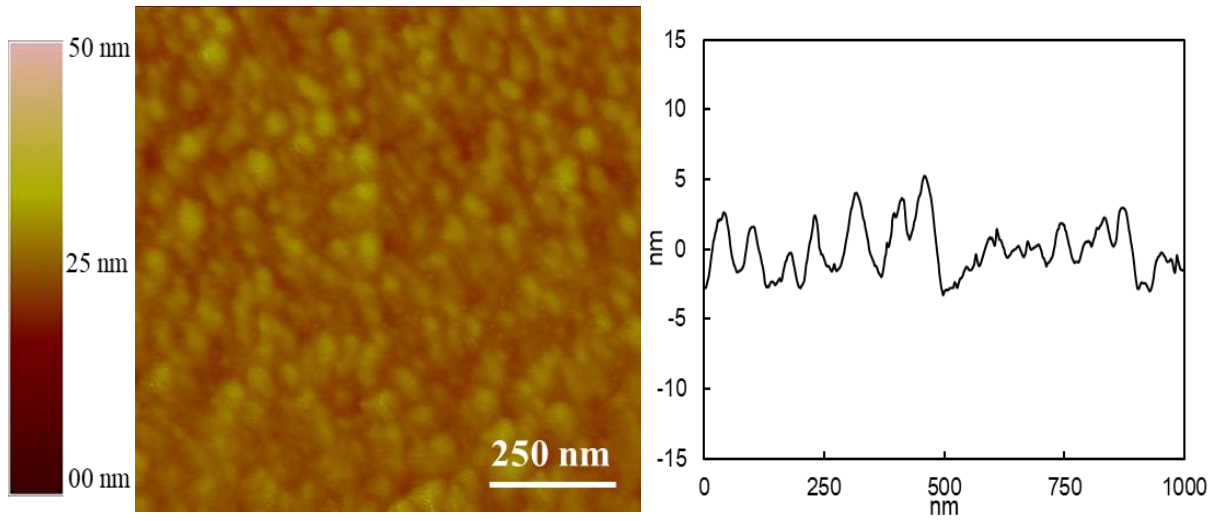


Fig. 4-7 (e) Grain density vs. treatment time.

4.5.2 Surface roughness

The effect of the APP treatment on the surface roughness of carbon films was observed by AFM in an area of $1\ \mu\text{m} \times 1\ \mu\text{m}$ and results are shown in Fig. 4-8. The root-mean-square (RMS) surface roughness is plotted as a function of the APP treatment time in Fig. 4-8 (d). An increase in the surface roughness of carbon films is observed as an effect of the APP treatment. An untreated film has RMS surface roughness 1.658 nm; it was increased to 3.091 nm after 3 min APP treatment. A similar observation of increasing surface roughness also observed in 5 min APP treated film. The surface roughness of the carbon film increased to 4.373 nm with 5 min APP treatment. The gradual increase with increasing APP treatment time indicates the tenacious destruction of chemical bonds, which contributed to the development of internal surface in carbon clusters, here the removal of sp^2 clusters has caused the surface roughness development.¹⁸⁾

a)



b)

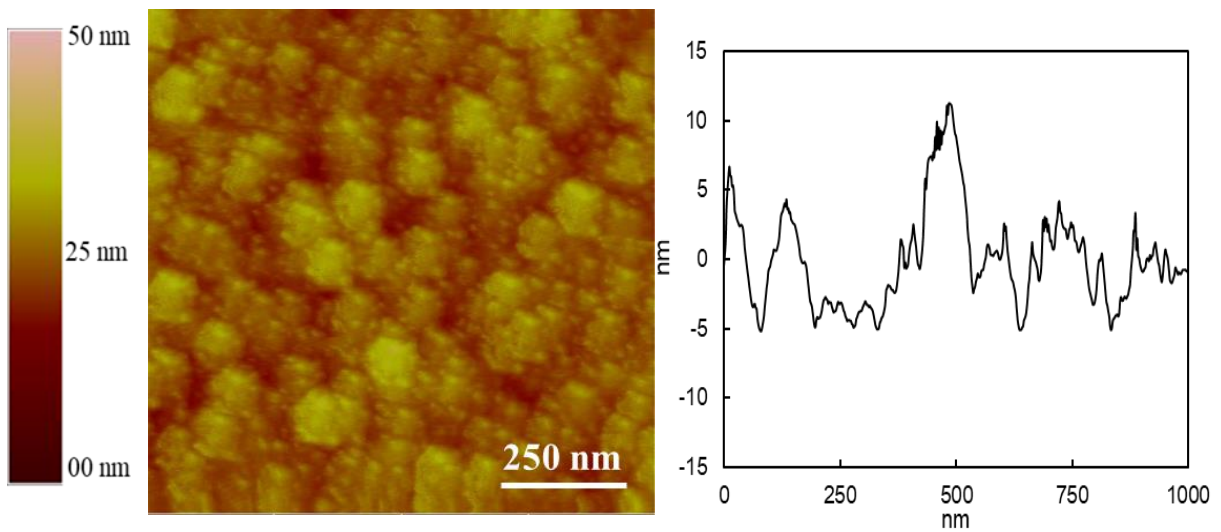
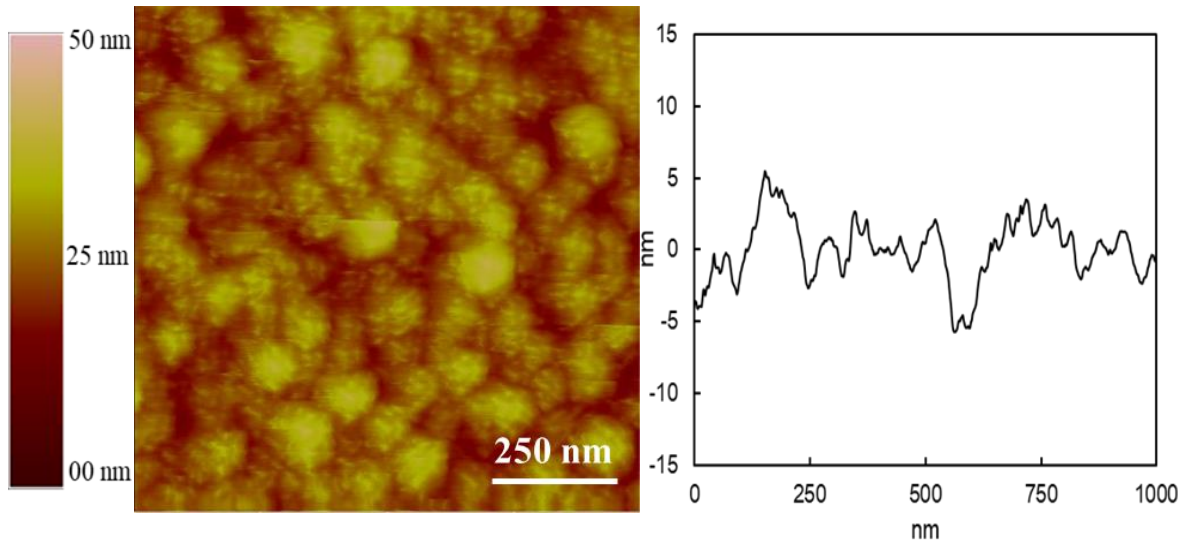


Fig. 4-8 a) AFM images of surface morphologies of untreated film b) AFM images of surface morphologies of 3 min treated film,

(cont.)

c)



d)

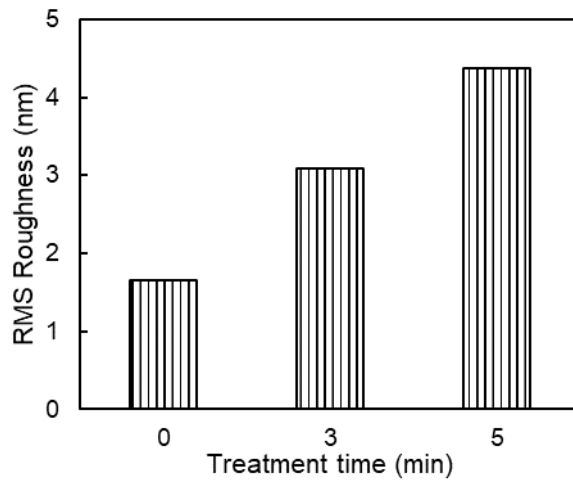


Fig. 4-8 c) AFM images of surface morphologies of 5 min treated film, d) RMS roughness changes as a function of the APP treatment.

4.5.3 Chemical structure

Figure 4-9 shows the NEXAFS analysis of untreated and APP treated carbon films. Observation of intense resonances near the X-ray absorption edge can indicate the type of bonding.¹⁹⁾ The typical NEXAFS spectra show 2 prominent peaks, centered at 284.8 eV and at 288.4 eV. The peak at 285.0 eV is originated due to the $1s \rightarrow \pi^*$ transition of sp^2 bonded carbon and the peak at 289.0 eV is originated due to the $1s \rightarrow \sigma^*$ transitions of sp^3 bonded carbon. The peak at 286.5 eV is arisen due to the absorbed oxygen.²⁰⁾ Figure 4-9 (a) shows NEXAFS analysis results for the untreated and 3-minute APP treated sample. Figure 4-9 (b) shows a graph of a decrease in sp^2 (%) with an increase in treatment time. For the 3, 4 and 5 minutes treated samples, sp^2 (%) decreased from 49 % to 46%, 45%, and 42% respectively. The APP treatment removed or modified sp^2 clusters with selectively sp^3 carbons. Namely, the removal or modification of graphitic sp^2 bonds is due to the APP surface treatment of carbon films.

Next, XPS studies of as-deposited and 3 min. plasma treated samples were made to find any evidence of change in the structural properties at the surface.²⁰⁾ Figure 4-9 (c and d) shows XPS spectra corresponding to the C 1s core peak of the as-deposited and plasma treated samples. A change in peak shape of the as-deposited and plasma treated samples were obtained. To find the cause behind the change in the peak line-shape, the peaks were decomposed into each spectral component for each chemical bonding in detail. Figure 4-9 (c-d) represents the C 1s peak decomposition of the as-deposited sample (Fig. 4-9(c)) and the plasma treated sample (Fig. 4-9(d)). The oxygen peaks in CFUBM sputtering deposited amorphous carbon films were also observed in similar work previously by other researchers.²¹⁾ The shape of the peak line was changed by the APP treatment. The ratio (O/C+O) increased when films were exposed to the APP treatment (Fig. 4-9(e)). Since the APP treatment, the species generated from the APP and oxygen-related species caused the oxidization of carbon at the sample surface. Overall, the removal or modification of sp^2 bonds and atmospheric oxidation due to the radicals/ions caused to modify its surface chemically.

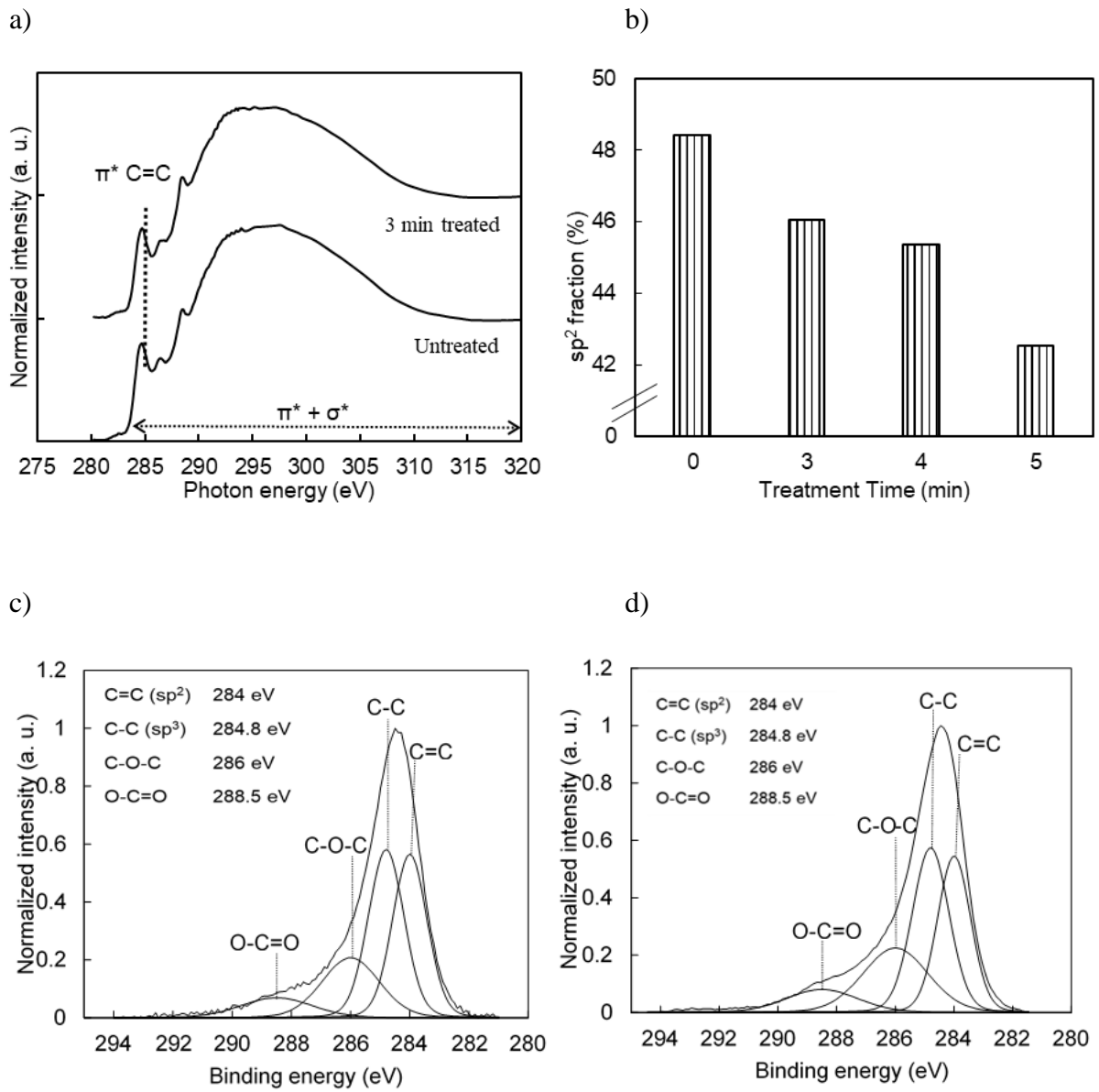


Fig. 4-9 a) (a) NEXAFS spectra of as-deposited and 3 minutes treated sample. (b) sp^2 (%) vs treatment time, c) XPS peak decomposition of C 1s spectra of as-deposited sample. (d) XPS Peak decomposition of C 1s spectra of 3 minute treated sample,

(cont.)

e)

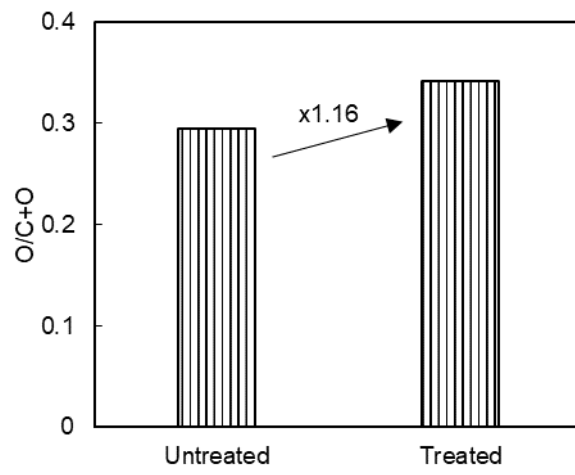


Fig. 4-9 (e) O/C+O ratio of as-deposited and 3 minutes treated sample from XPS.

4.5.4 Microstructure

Raman spectrum was recorded to check the effect of APP treatment on film's structural properties. Figure 4-10 (a) represents the recorded Raman spectrum for the plasma untreated and treated films. Raman spectrum of carbon films consisting of three peaks, namely D (1350 cm^{-1}) and G ($\sim 1540\text{ cm}^{-1}$) and an additional peak around 1188 cm^{-1} . D peak arises due to graphitic disorder and G peak represents the graphitic band.²²⁾ The peak around 1188 cm^{-1} can be assigned to mixed $\text{sp}^2 - \text{sp}^3$ bonds.¹⁶⁾

The detailed study of Raman spectra based on peak intensity, position, area, and width can give insights of chemistry and structure of carbon films as these parameters are closely related to density, size, and structure of sp^2 clusters.²³⁾ To determine two spectral components, a curve fitting on the basis of the above parameters was conducted. Analysis of this spectrum is shown in Fig. 4-10 (b-d) for the area under peak ratio, FWHM, and position of G band respectively. From Fig. 4-10 (b), the peak area ratio and D band peak area decreased as treatment time increased. This decrease is due to the decrease in size and number of graphite-like sp^2 clusters.²⁴⁾ A decrease in D band peak area indicates an increase of sp^2 coordination.¹⁸⁾ A negligible increase in FWHM was observed. However, no shift in the position of G band peak was observed. Thus, unlike power density variation, no crystallographic changes in carbon films were caused by the APP treatments.

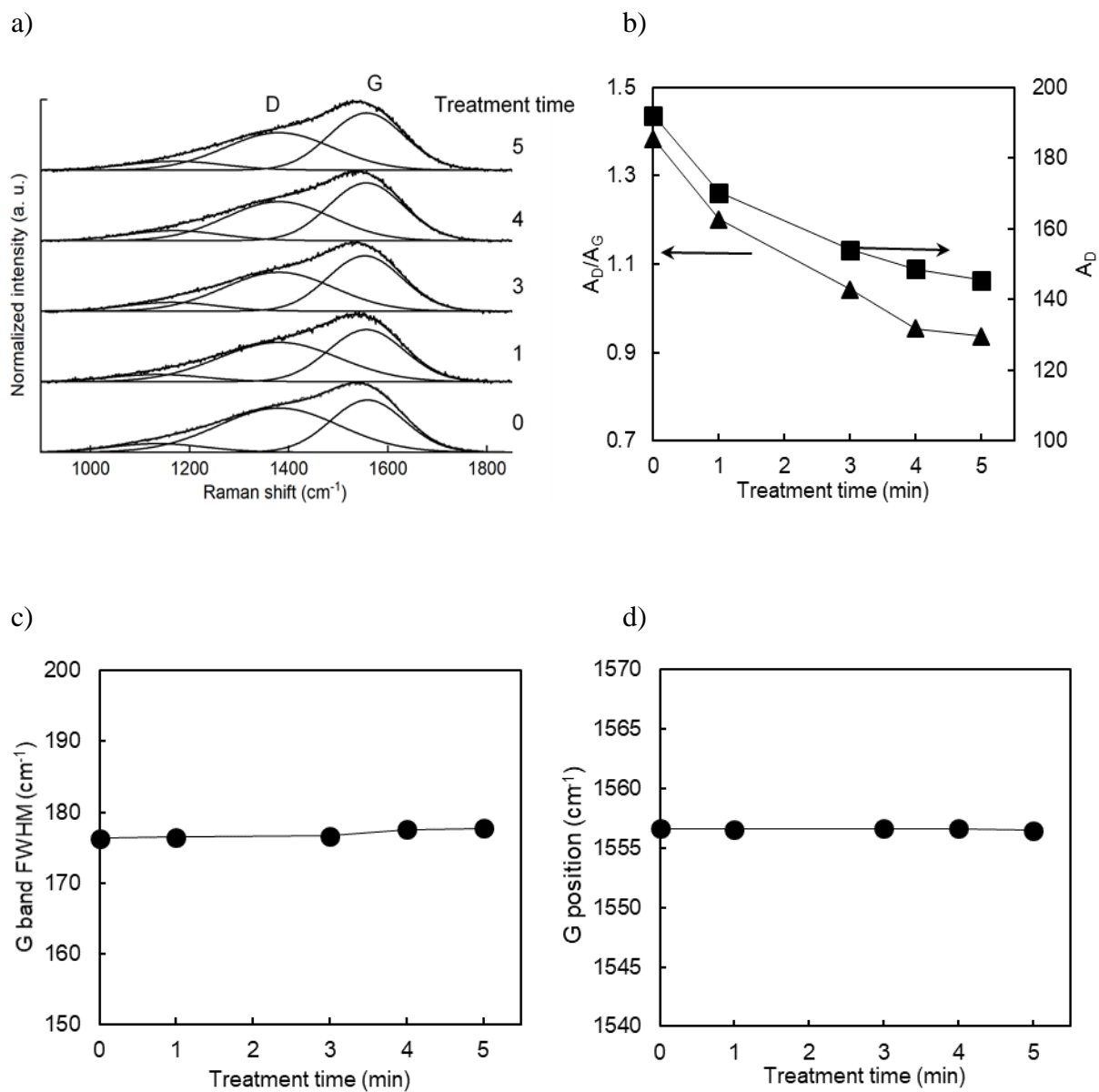


Fig. 4-10 a) Raman Spectra of plasma treated samples. (b) The area under peak ratio vs. treatment time. (c) FWHM of G band vs. treatment time. (d) The position of G band vs. treatment time.

4.5.5 Optical and electrical properties of APP treated carbon films

The effect of post plasma treatment on the optical and electrical properties by recording the optical band gap and the sheet resistance was also studied. Data acquisition and processing method were identical, as described previously. Increase in optical band gap was observed with increase in the APP treatment time due to the etching of sp^2 clusters (Fig. 4-11 (a)). A similar trend in the electrical properties of the APP-treated films appeared. The sheet resistance of the APP-treated films increased with treatment time (Fig. 4-11 (b)).

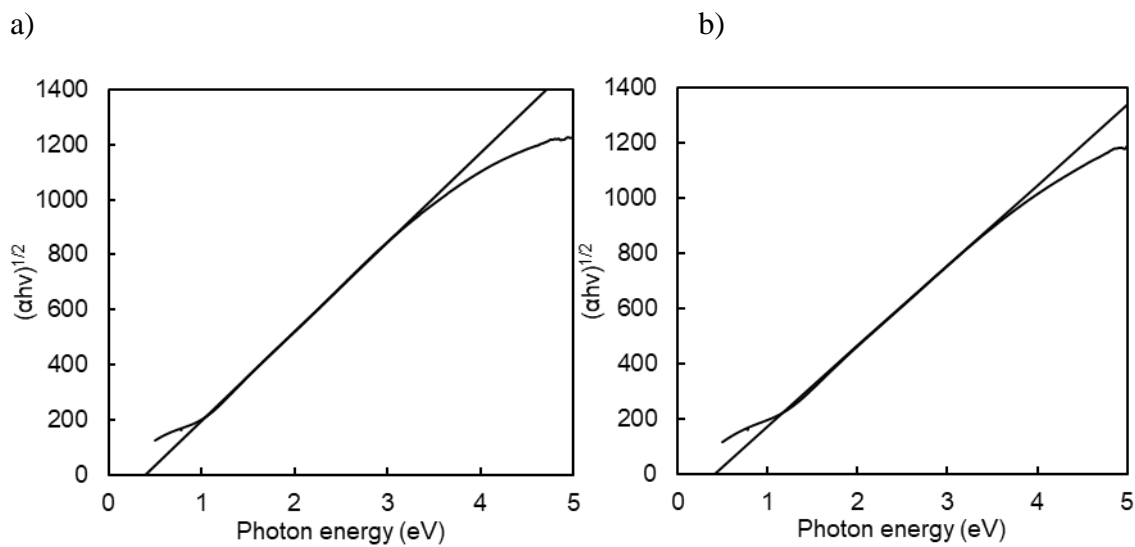


Fig. 4-11 a) Tauc plot of the untreated film, b) Tauc plot of the 1 min treated film,

(cont.)

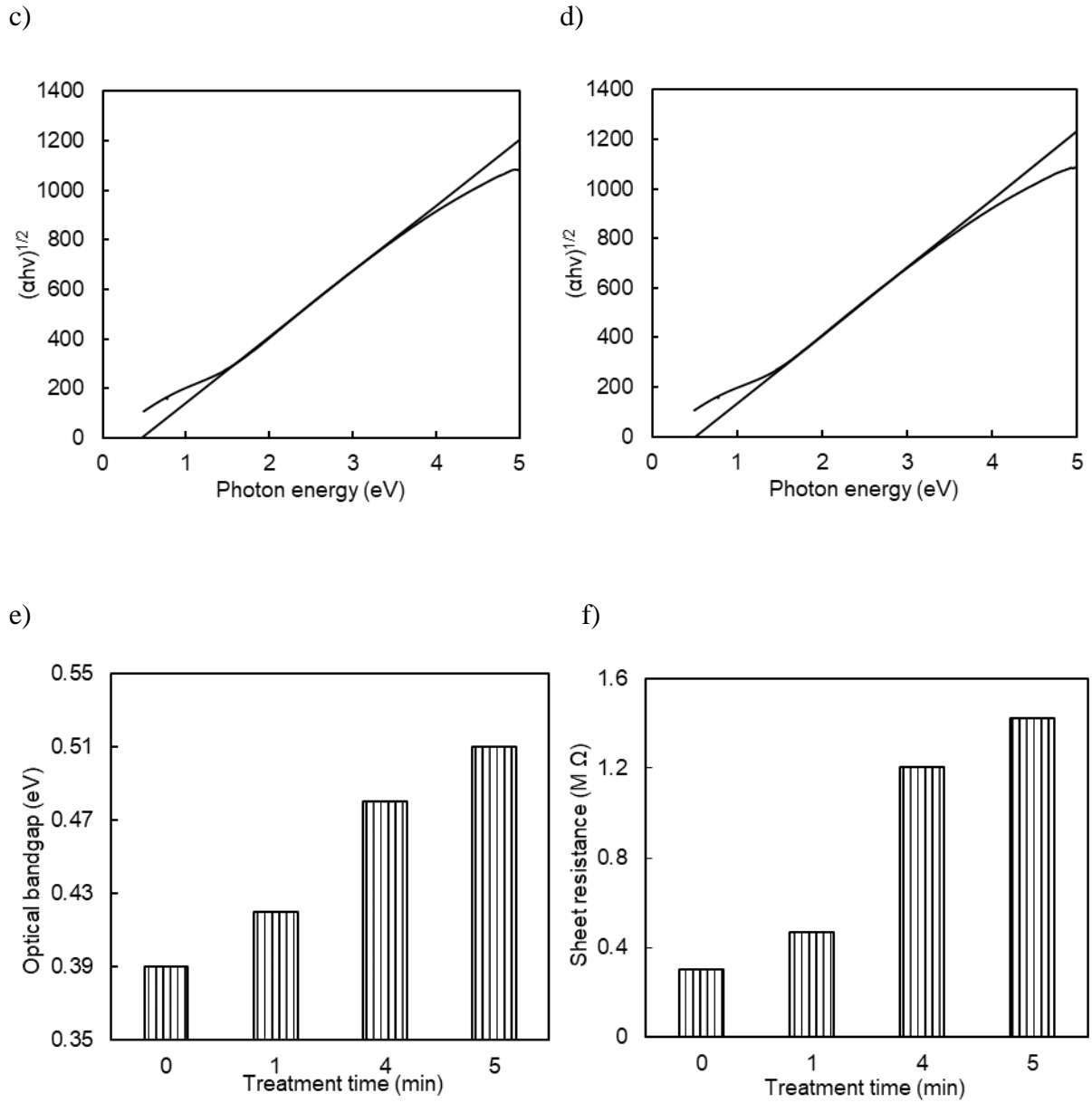


Fig. 4-11 c) Tauc plot of the 4 min treated film, d) Tauc plot of the 5 min treated film, e) Optical band gap vs. plasma treatment time, f) Sheet resistance vs. plasma treatment time.

4.6 Discussion

In conventional techniques in control of the film properties of carbon films, deposition parameters can be controlled with a wide range of structural and bonding characteristics for the bulk of the carbon films.^{4,5)} Meanwhile, surface characteristics are significantly attracted in attention for the controls. The author emphasizes that a surface bonding structure of the films played a vital role in the case of the APP-treated films. In our experimental results as discussed above, the author found that a decrease in sp^2 clusters and change in surface morphology upon the APP post-treatments. This is also caused a relative change in carbon film's optical and electrical properties. the author believes that the concave features as cavities produced between neighboring grains due to the APP post-treatments acted as a barrier for the flow of electrons thus increase in sheet resistance was observed.

From these observations, the optical and electrical properties of the carbon films can be changed with the APP post-treatment time. For simplification, Fig. 4-12 shows the schematic model of the effect of APP treatment on carbon films. The as-deposited carbon films consisted of pure carbons of a percentage of 71% with sp^2 content of approximately 48%. The surface morphology of the as-deposited carbon film appeared with the tightly filling of smaller grains. By the APP post-treatment, the surface was changed in morphology with the sparsely of larger grains. Meanwhile, the concentration of oxidized carbons increased and the sp^2 content decreased to 42%. Therefore, the author points out that the APP post-treatments etched off the sp^2 contents located at the grain boundaries, leading to the increase in the electrical resistance.

The author believes that the bulk and surface properties of the carbon films changed as an effect of power density variation and the APP treatment significantly.

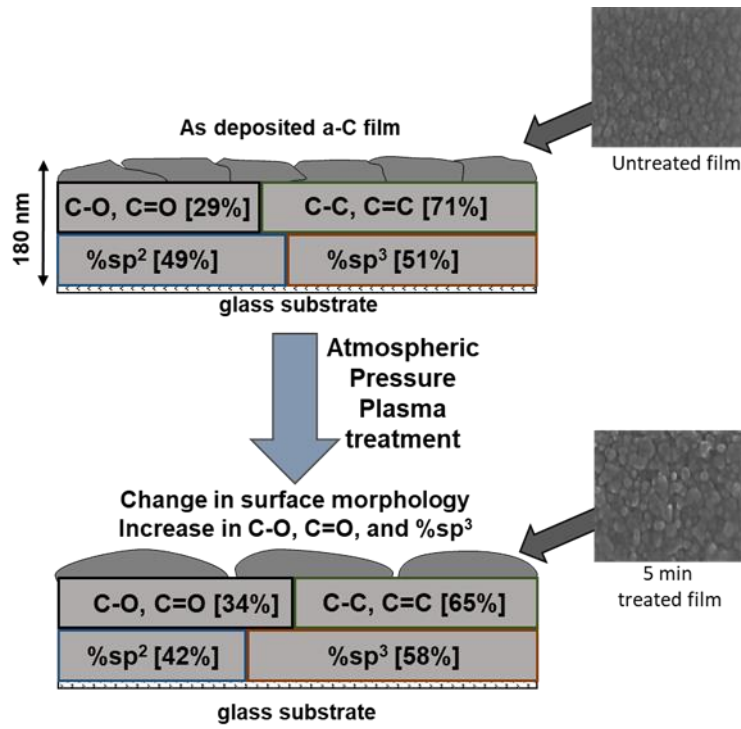


Fig. 4-12 Schematic model changes in film properties due to APP treatment.

4.7 Conclusion

A relationship between surface/bulk structures and optical/electrical properties of carbon films deposited by closed field unbalanced (CFUBM) magnetron sputtering process was studied. The carbon films were deposited with various discharge powers (1200, 1600 and 2000 W) for different power density values (15, 20, and 25 W/cm²). Due to the enhancement in Ar ion bombardment on the target resulting in increasing sputtered species with the rise in power density, the deposition rate was increased with increasing power density. As seen from SEM, the surface morphology of the carbon didn't change with varying power density. In the Raman analysis, an increase in peak intensity ratio (I_D/I_G) and peak area ratio (A_D/A_G) with increasing power density were observed along with the upshift in the G band peak position which confirms the ordering and increase of sp² sites with increasing power density. Graphitic cluster formation in the high-density plasma resulted into the deposition of sp² cluster rich film. This also has an effect on optical and electrical properties of the carbon films, as optical band-gap of carbon films narrowed and sheet resistance increased with increasing power density during deposition.

In the case of post-deposition atmospheric pressure plasma (APP) treatment, APP caused a change in surface morphology of the films effectively. This suggests due to removing a part of the film by Ar APP treatments. Notably, cavities between neighboring grains were increased with the APP treatment time, resulting in a formation of ordered grains and decrease in a number of grains per unit area. From the AFM observations for surface roughness, it was observed that the surface roughness of carbon films increased as an effect of the APP treatment. The APP treatment modified the film structure chemically, as confirmed from the NEXAFS analysis, the APP treatment removed or modified sp² clusters with selectively sp³ carbons as %sp² decreased with increasing APP treatment time. Further, the XPS results showed that the species generated from the APP and oxygen-related species caused the oxidization of carbon at the sample surface as O/C+O ratio increased with APP treatment. Overall, the removal or modification of sp² bonds and atmospheric oxidation due to the radicals/ions caused to modify its surface chemically.

In the case of optical and electrical properties of the APP treated carbon films, the APP treatment caused the increase in the sheet resistance as well as the optical band gap of the carbon films.

Consequently, the author developed a technique to control structural, optical and electrical properties for bulk and surface of the magnetron-sputtered carbon films, by controlling power density variation during deposition and the subsequent APP treatments.

References:

- 1) T. D. Burchell, *Carbon Materials for Advanced Technologies* (Elsevier, 1999) p. 1.
- 2) J. Robertson, *Adv. Phys.* **35**, 317 (1986)
- 3) A. C. Ferrari and J. Robertson, *Phys. Rev. B* **61**, 14095 (2000).
- 4) A. Ugale, R. Jagtap, D. Pawar, S. Datar, S. Kale, and P. Alegaonkar, *RSC Adv.* **6**, 97266 (2016).
- 5) W. Mróza, S. Burdyńska, A. Prokopiuka, M. Jedyńska, and B. Budner, *Acta Physica Polonica A* **116**, 120-122 (2009).
- 6) B. Window, *Surf. Coat. Technol.* **71**, 93 (1995).
- 7) J. Han, *J. Phys. D: Appl. Phys.* **42**, 43001 (2009).
- 8) J. M. Poate, G. Foti, and D. C. Jacobson, *Surface Modification and Alloying: by Laser, Ion, and Electron Beams* (Plenum Press, New York 1981)
- 9) D. Tashima, A. Sakamoto, M. Taniguchi, T. Sakoda, and M. Otsubo, *Vacuum* **83**, 695 (2009)
- 10) F. Ghamouss, E. Louis, C. Thobie-Gautier, P.-Y. Tessier, and M. Boujtit, *Electrochim. Acta* **54**, 3026 (2009).
- 11) Y. Kusano, H. Mortensen, B. Stenum, S. Goutianos, S. Mitra, A. Ghanbari-Siahkali, P. Kingshott, B.F. Sørensen, and H. Bindslev, *Int. J. Adhesion Adhesives* **27**, 402 (2007).
- 12) K. Han, H. Kim, M. Song, M. Park, S. Han, J. Lee, and J. Kang, *App. Phys. Lett.* **86**, 263105 (2005)
- 13) S. Park, Y. Chang, C. Moon, D. Suh, S. Im, and Y. Kim, *Bull. Korean Chem. Soc.* **31**, 335 (2010)
- 14) R. D. Arnell, and P. J. Kelly, *Surf. Coat. Technol.* **112**, 170 (1999).
- 15) J. Schwan, S. Ulrich, V. Batori, and H. Ehrhardt, *J. Appl. Phys.* **80**, 1 (1996).
- 16) B. Dippel, H. Janderb and J. Heintzenberga, *Phys. Chem. Chem. Phys.* **1**, 4707 (1999).
- 17) C. Casiraghi, A.C. Ferrari, and J. Robertson, *Phys. Rev. B* **72**, 085401 (2005).

Chapter 4

- 18) J. Wu, Y. Wang, C. Kuo, *J. Phys. Chem. Sol.* **69**, 505 (2008).
- 19) C. Brundle, C. Evans, and S. Wilson, *Encyclopedia of Materials Characterization* (Gulf Professional Publishing, 1992), p. 228
- 20) M. Jaouen, G. Tourillon, J. Delafond, N. Junqua, G. Hug, *Diamond Relat. Mater.* **4**, 200 (1995).
- 21) M. Kumar, A. Javid, J. Han, *Langmuir* **33**, 2514-2522 (2017).
- 22) J. Schwan, S. Ulrich, V. Batori, and H. Ehrhardt, *J. Appl. Phys.* **80**, 1 (1996).
- 23) C. Casiraghi, A.C. Ferrari, and J. Robertson, *Phys. Rev. B* **72**, 085401 (2005).
- 24) G. Irmer and A. Dorner-Reisel, *Adv. Eng. Mater.* **7**, 694 (2005).

Chapter 5

SnO₂ nanoparticle bound graphene composites - In-liquid plasma assisted synthesis using SnO₂ dispersed ethanol

5.1 Introduction

Graphene-based composites have been produced by incorporating materials in graphene.^{1,2)} The composite formation is categorized into two regimes, *ex-situ* and *in-situ* binding of two or more materials. The conventional graphene synthesis methods such as chemical vapor deposition, epitaxial growth are costly and, require lower pressure and high temperature, and possess low growth speed.^{3,4)} Thus, the composites are limited to realize only mixing that these incorporated materials are usually noble metals, conducting polymers, and metal oxides. This approach is the easiest approach for composite synthesis but low density and non-uniform distribution are major drawbacks, limiting performance. These methods are called as *ex-situ* binding, here. In contrast to the *ex-situ* binding, it is limited to introduce that *in-situ* binding involves two methods in the case of SnO₂. First, *in-situ* oxidation of tin takes place at reaction field existing precursor salt (SnCl₂/SnCl₄) in presence of pre-synthesized graphene. Second, *in-situ* reduction of graphene oxide takes place in presence of SnO₂ precursor salt. In both approaches, the main focus is on graphene synthesis and parameters related to graphene synthesis are crucial to deciding the applicability of synthesis approach. In the latter case of *in-situ* binding, it provides uniform distribution of SnO₂ in graphene, however, the low speed of synthesis is the major issue.⁵⁾

In chapter 4, the author described the importance of the non-equilibrium plasma for surface modification of carbon films, as an effect of the plasma treatment the optical and

electrical properties changed. Upon the plasma treatment, the electrical conductivity of the carbon films was decreased. In gas sensing application development perspective, the conductivity of the carbon films is crucial. Hence, the author studied graphene-based materials as graphene has the highest conductivity. Along with a utilization of the graphene, the author thinks that the non-equilibrium in-liquid plasma can play a vital role in the functionalization of materials.

Individual changes in the properties of component materials such as graphene and SnO₂ are important. Indeed, graphene and SnO₂ possess different optical properties, e.g., graphene has nearly zero bandgap and on the other hand, the SnO₂ has a wide band gap (3.62 eV). The zero and wide band gap of graphene and SnO₂ respectively limit their use in photovoltaic applications. In this regard, bandgap engineering of these materials is needed.^{3,6)} Therefore, it is required to study in the details for a realization of composite formation and effect of dispersion of SnO₂ in graphene.

The in liquid plasma method enables the high-speed graphene synthesis at room temperature and atmospheric pressure with the pure alcohol as a single precursor.⁷⁻⁹⁾ To extend the in liquid plasma graphene synthesis method, a facile single process has been developed for in situ binding of SnO₂-graphene composite with in-liquid plasma method without providing external heat.

In this study, the aim of this work is to develop a hybrid and novel approach for composite synthesis based on the in-liquid plasma assisted process at room temperature. Thus, the pre-synthesized SnO₂ was mixed in a graphene precursor (ethanol) followed by the in-liquid plasma treatment.

5.2 Experimental details

SnO₂ nanoparticles were synthesized by a sol-gel method.¹⁰⁾ A 0.1M solution of SnCl₂·2H₂O was prepared using a distilled water. The solution was heated at 60°C and stirred for 15 min. With continued stirring, 1M NaOH was added to the solution dropwise until the solution turned the pH of 8. Persistent stirring of the solution with 400 rotation-per-minute (rpm) was carried out at 60°C for another 2 hours. After 2 hours of stirring, the solution changed its color from white to gray indicating the formation of SnO₂. The final product was cleaned several times with water and ethanol to remove impurities and then filtered to obtain a precipitate. The precipitate was air-dried and later, annealed at 400°C for 2 hours. The schematic of the experimental procedure for SnO₂ synthesis by the sol-gel method is shown in Fig. 5-1 (a).

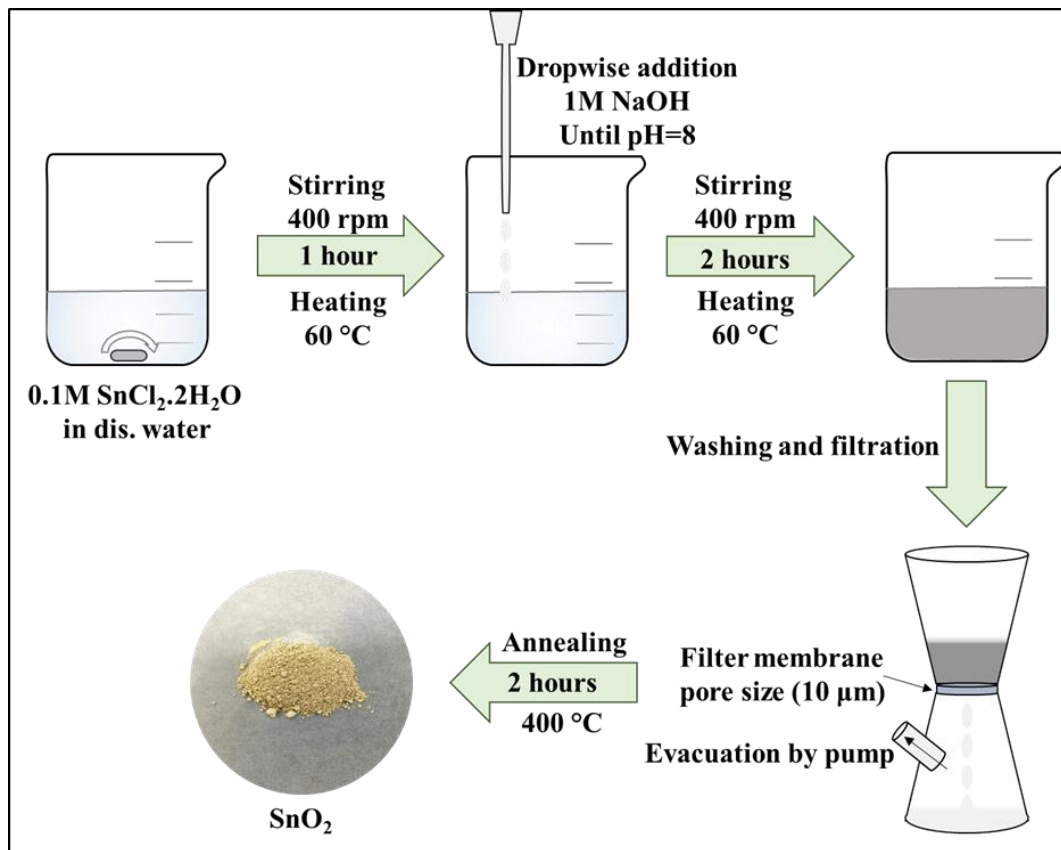
For the composite synthesis, the SnO₂ (8 mg) synthesized by a sol-gel method was dispersed in 100 ml ethanol for 15 min using homogenizer (Tomy Seiko UR-21P) as SnO₂ is insoluble in ethanol. This solution of SnO₂ and ethanol was then placed in a reactor. Ar gas was flown into the reactor at atmospheric pressure with a flow rate of 6 standard-liter-per-minute (slm) to fill the upper part of reactor above the liquid surface. Figure 5-1 (b) shows a schematic illustration of an experimental apparatus used in this study. The choice of electrodes and alcohol precursor was based on the previous studies related to synthesis rate and crystallinity of graphene in-liquid plasma assisted graphene synthesis. Combination of graphite electrodes and ethanol yields nanographene with high crystalline and rapid synthesis rate of graphene synthesis.⁸⁻⁹⁾ Graphite electrodes (3 mm diameter) were arranged as shown in Fig. 5-1 (b). An alternating current (9 kV at 60Hz) was applied to electrodes in order to generate high-density plasma between electrodes. A chronological discharge then was ensued between high-density plasma and electrode immersed in liquid through the gas-liquid interface. The solution changed its color to black within a few minutes of plasma discharge.

After 30 min of the discharge, the synthesized material was collected by filtering the black colored solution with the suction filtration using a membrane filter with pore size of 1

μm and dried at 60°C for 15 min. Similarly, graphene was also synthesized using this technique (without the addition of SnO_2 and keeping all conditions same) and further used to compare with the composite. Fig. 5-1 (c) shows the schematic of the experimental procedure for composite synthesis.

The optical properties were measured using a spectrophotometer (V670, JASSO) in the ultraviolet-infrared spectral range, 200 - 2500 nm. Optical band gap (E_g) was calculated as follows. An absorbance of material was recorded by the optical spectrophotometer. Based on measured absorbance, the absorption coefficient was calculated. As plotted with a Tauc plot showing $(\alpha h\nu)^{1/2}$ vs. energy, the extrapolation of straight line to $(\alpha h\nu)^{1/2} = 0$ axis gives the value of band gap.¹¹⁾ The optical emission from the in-liquid plasma was obtained in the gas phase region close to 3 mm above the liquid surface. The plasma emissions were measured using multi-channel Ocean optics HR-4000 spectrometer in the range between 200 and 900 nm.

a)



b)

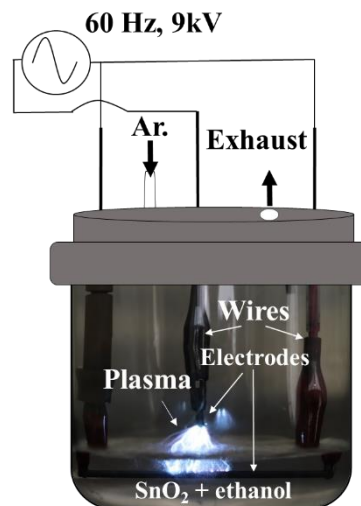


Fig. 5-1 a) Schematic of the experimental procedure for SnO_2 synthesis by sol-gel method. b)

In-liquid plasma apparatus for composite synthesis,

(cont.)

c)

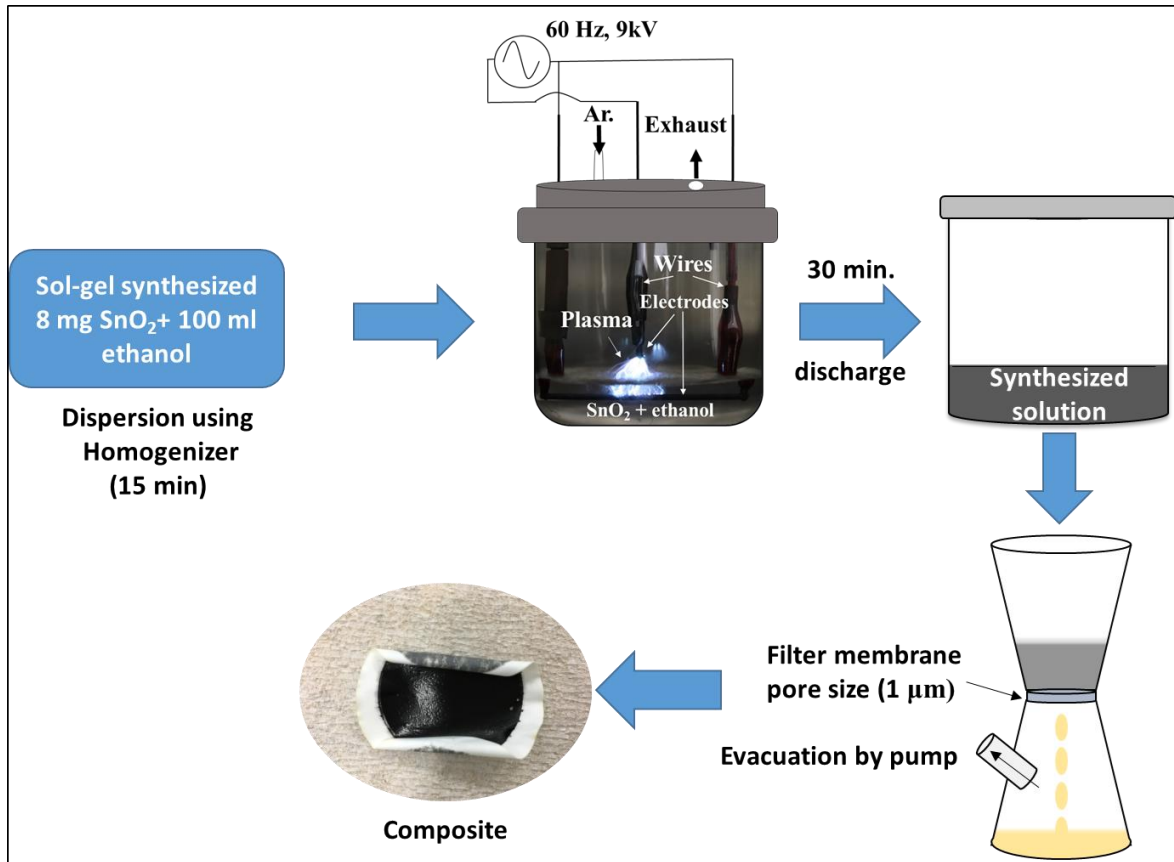


Fig. 5-1 c) Schematic of the experimental procedure for the composite synthesis.

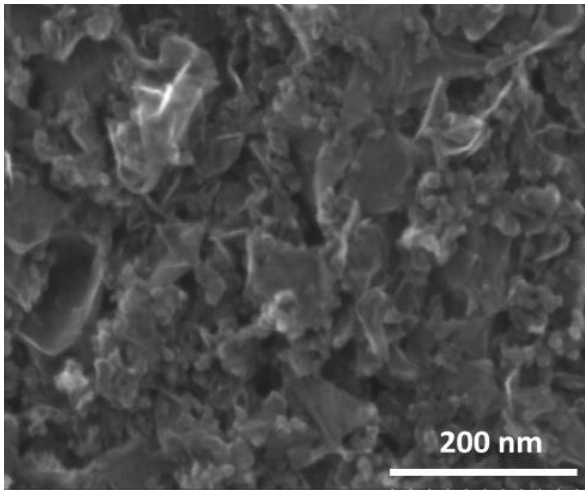
5.3 Results and discussion

5.3.1 Morphology and elemental distribution

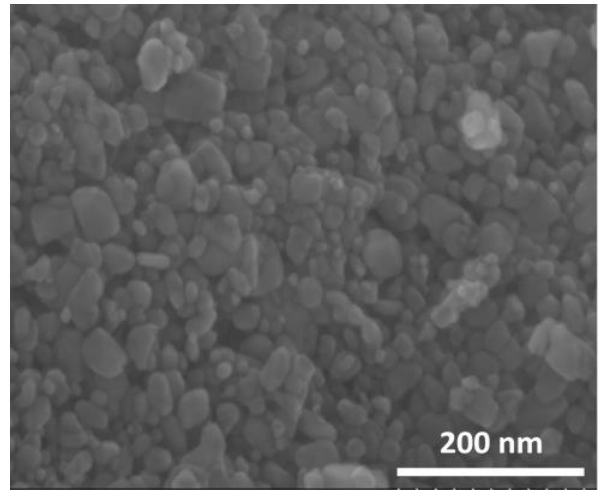
Figure 2 shows the SEM images of the as-synthesized graphene (Fig. 5-2 (a)), SnO₂ used for dispersion (Fig. 5-2 (b)) and composite (Fig. 5-2 (c)). The graphene's SEM image clearly indicated the formation of a sheet-like structure with an average sheet length in the range of hundred to few hundred nanometers (Fig. 5-2 (a)). The surface morphology study of sol-gel synthesized SnO₂ showed nanoparticles with the irregular size distribution (Fig. 5-2 (b)). In the SEM image of the composites, flaky graphene sheets and SnO₂ particles are clearly visible. A uniform distribution of SnO₂ nanoparticles on the flaky graphene sheets was observed. Figure 5-2 (d) is an EDS mapping of the composite. Through the EDS map, the presence of C and Sn and O was observed. In a composite EDS map, the uniform distribution of SnO₂ nanoparticles on graphene sheets was also confirmed. In EDS mapping for carbon and oxygen, appeared excessive carbon and oxygen is from the carbon tape used for measurement. The EDS results are in good agreement with SEM observations regarding SnO₂ distribution on graphene sheets.

To further identify the microscopic morphology, the composite was investigated by TEM-EDX analysis (Fig. 5-3). Similar observations as in SEM-EDS regarding the uniform distribution of SnO₂ particles in graphene observed from TEM images. The dispersion of SnO₂ in ethanol followed by the plasma treatment resulted in aggregation of SnO₂ particles, these aggregated nanoparticles were distributed uniformly on graphene (Fig. 5-3 (a)). As observed from TEM, the average size of SnO₂ nanoparticles is around 30 nm (Fig. 5-3 (b)). The EDX spectra were acquired at two different points (on aggregated SnO₂ nanoparticles and graphene sheet) on the composite. It confirmed the elemental confirmation of C, O, and Sn (Fig. 5-3 (c, d)). The occurrence of Cu is from the membrane used for the observation.

a)



b)



c)

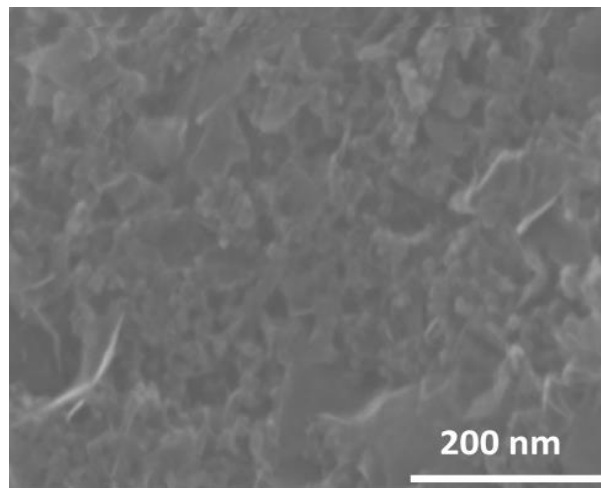


Fig. 5-2 Surface morphology (SEM images) of a) graphene, b) SnO₂, c) composite,

(cont.)

d)

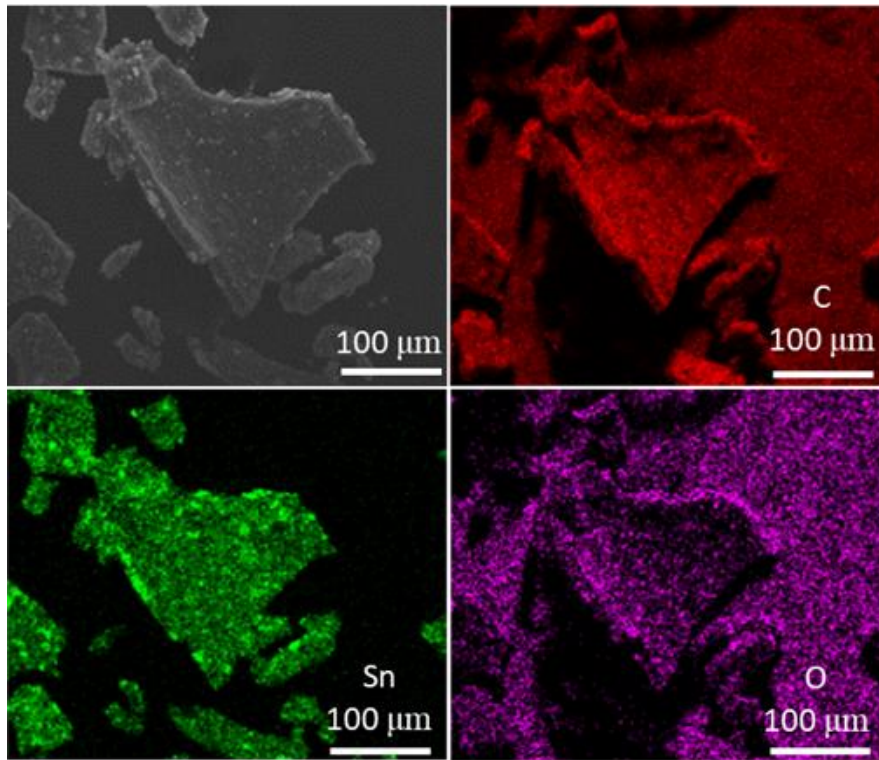


Fig. 5-2 d) EDS mapping of the composite.

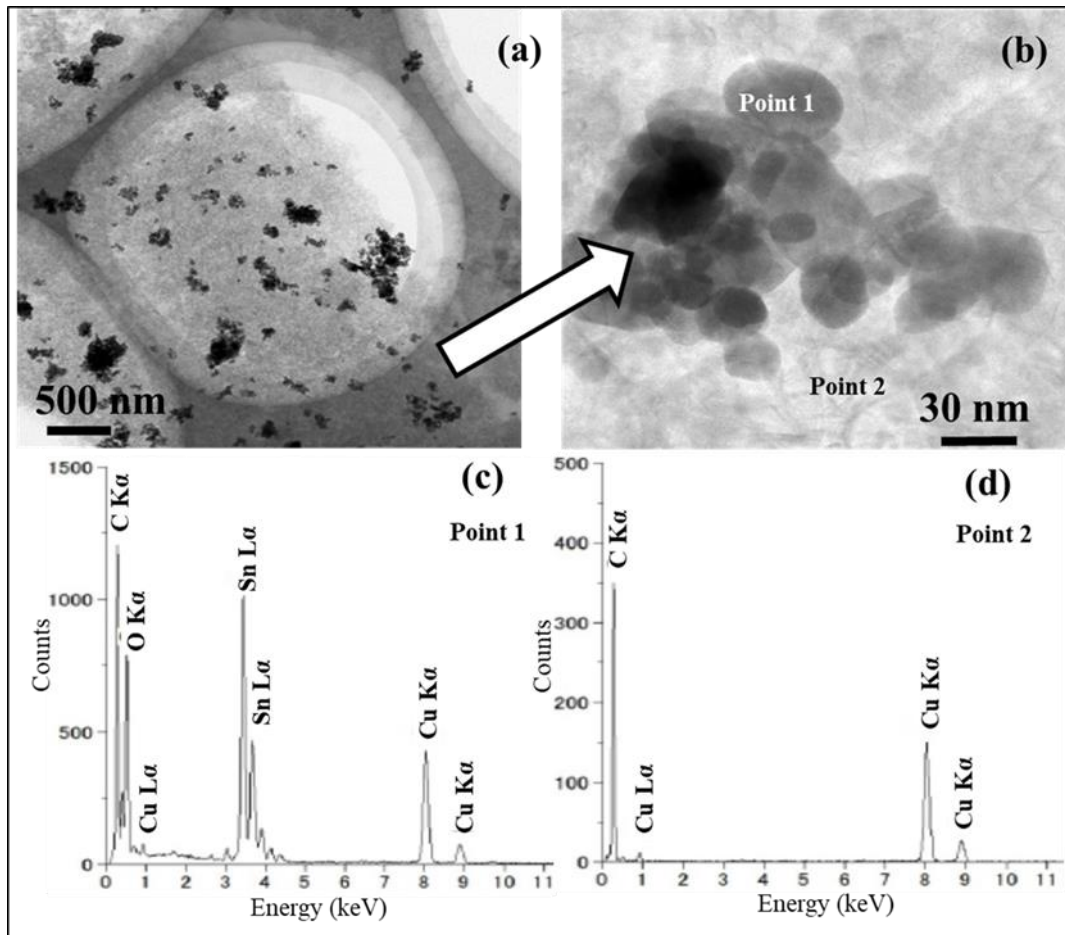


Fig. 5-3 TEM and EDS observations of composite a) low magnification image, b) high magnification image, c) elemental line profile based on the EDS results at point 1, d) elemental line profile based on the EDS results at point 2.

5.3.2 Chemical composition

The FTIR analysis of the composite was carried out in order to study functional groups of the composite. The recorded FTIR spectrum of the SnO₂ (a), graphene (b), and composite (c) is shown in Fig. 5-4. In the SnO₂ spectrum, an absorbance band centered at 673 cm⁻¹ represents stretch vibrations of tin and oxygen atoms.¹²⁾ In the graphene spectrum, the absorbance band at 1592 cm⁻¹ is due to the aromatic C=C stretching and 2921 cm⁻¹ arise due to the C-H stretch vibrations of the methylene group. A broad peak at 3420 cm⁻¹ is arising due to O-H stretch of the carboxylic functional group.

In an FTIR spectrum of the composite, all associated peaks of graphene and SnO₂ appeared. A peak at 1162 cm⁻¹ has occurred in the composite spectra. The occurrence of this peak is due to the emergence of oxygenated groups may be as a result of SnO₂ dispersion (C-O-C stretching), this indicated that the dispersed SnO₂ nanoparticles were interacted with graphene chemically.^{13, 14)} A presence of absorbance bands of SnO₂ and graphene indicates the formation of SnO₂-graphene composite.

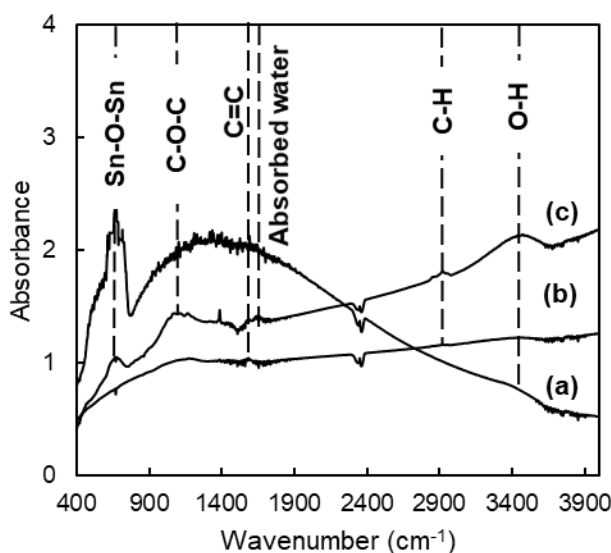


Fig. 5-4 FTIR spectra of a) SnO₂, b) graphene, and c) composite.

5.3.3 Microstructure analysis

Raman spectroscopy is a distinctive and non-destructive tool for the microstructure analysis of carbon materials. ¹⁵⁾ Figure 5-5 shows recorded Raman spectra of graphene (a), SnO₂ (b) and SnO₂-graphene composite (c). In the case of graphene, typical peaks at 1337 cm⁻¹, 1570.4 cm⁻¹, 1605.3 cm⁻¹ and 2667.7 cm⁻¹ were clearly found. The most prominent peaks of graphene are the G-band and 2D-band ones appearing at 1570.4 cm⁻¹ and 2667.7 cm⁻¹ respectively. The G-band peak is an indication of a six-membered ring structure in the graphene sheets. The 2D-band peak is also a characteristic peak of the graphene. ¹⁶⁾ The peaks at 1337 cm⁻¹ and 1605.3 cm⁻¹ are referred to as D-band and D'-band, respectively. An occurrence of these peaks is due to the structural disorder of six-membered rings. This disorder is mainly from the imperfections in the edge region of the graphene. ¹⁷⁾

In Fig. 5-5 (b), SnO₂ characteristic peaks are shown, peaks at 327 cm⁻¹, 632 cm⁻¹, and 724 cm⁻¹ are the A_{2g}, A_{1g}, and B_{2g} modes respectively, arising due to vibrations of tin and oxygen atoms. ¹⁸⁾ In Fig. 5-5 (c), the Raman spectrum of the composite consists of all the characteristic peaks of SnO₂ and graphene confirming the formation of SnO₂-graphene composite. Detailed study of microstructure on the basis of intensity, position, and width of the peaks is summarized in Tables 5-I and 5-II.

Raman G-band peak of the composite was broadened and its position was shifted to a higher frequency as compared with pure graphene synthesized by the in-liquid plasma method. An intensity of D band increased over SnO₂ dispersion leading to an increase in peak intensity ratio, which is an indicator of formation of less crystalline graphene with a minimal decrease a domain size. The changes in domain size of graphene upon SnO₂ dispersion are summarized in Table 5-I.

A 2D band peak in Raman spectra of graphene appears as a result of an absence of disorders or defects. ¹⁹⁾ Detailed analysis of 2D-band peak parameters of graphene and the composite are shown in Table 5-II. As a result of SnO₂ dispersion, an upshift in the position and the broadening of the 2D band peaks were observed. An intensity ratio of the 2D-band peak to the D band peak decreased in the case of Raman spectra of the composite was compared

to the pure graphene 2D band. These changes suggest a generation of defects in the graphene due to SnO₂ dispersion.²⁰⁾

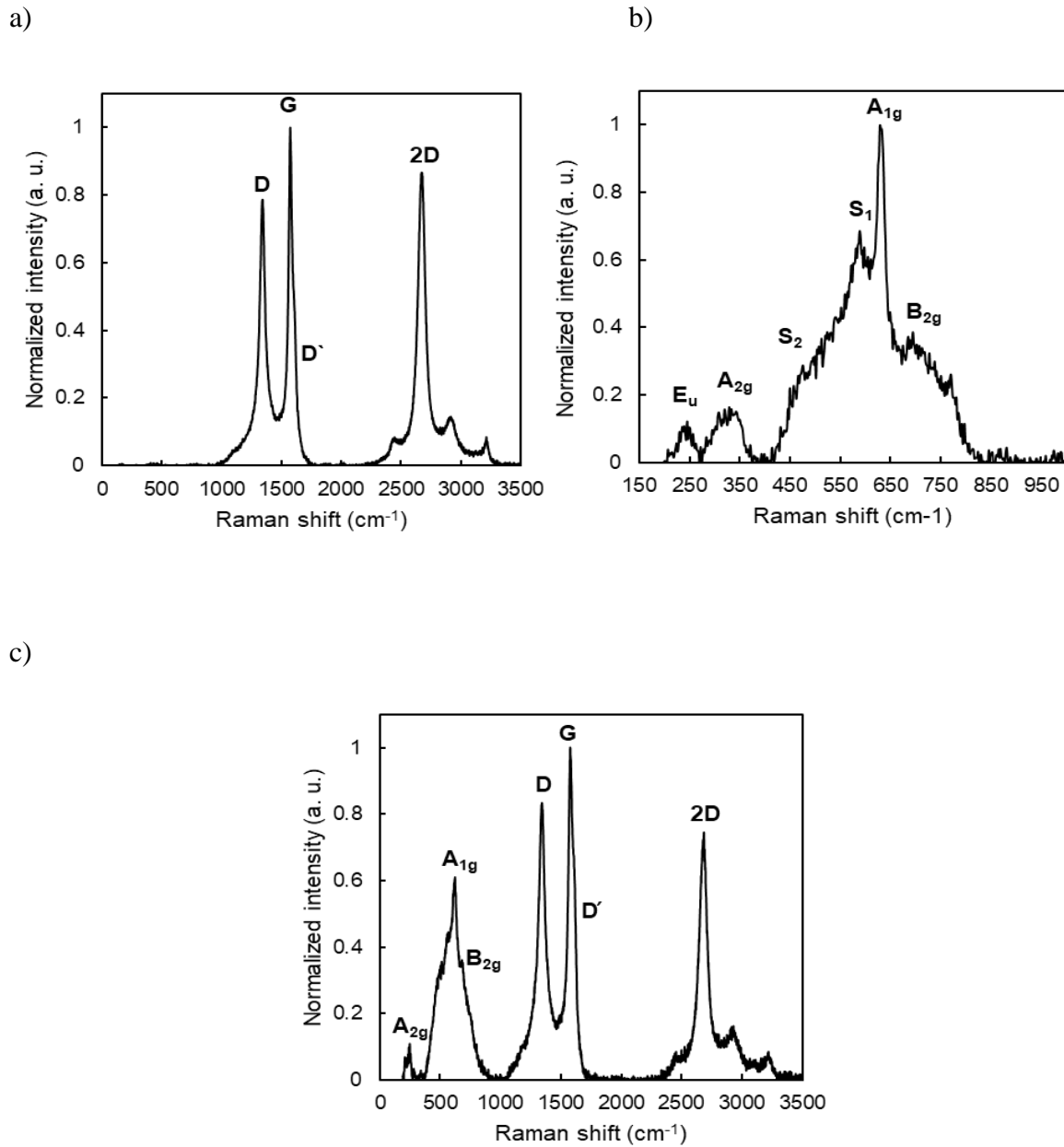


Fig. 5-5 Raman spectra of a) graphene, b) SnO₂, and c) composite.

Table 5-I Variation in G band and D band parameters.

	G band Position (cm^{-1})	G band FWHM (cm^{-1})	G band Intensity	D band Intensity	I_D/I_G	Domain Size (cm^{-1})
Graphene	1570.47	35.83	0.83	0.64	0.77	25
Composite	1575.98	42.19	0.83	0.68	0.82	24

Table 5-II Variation 2D band parameters.

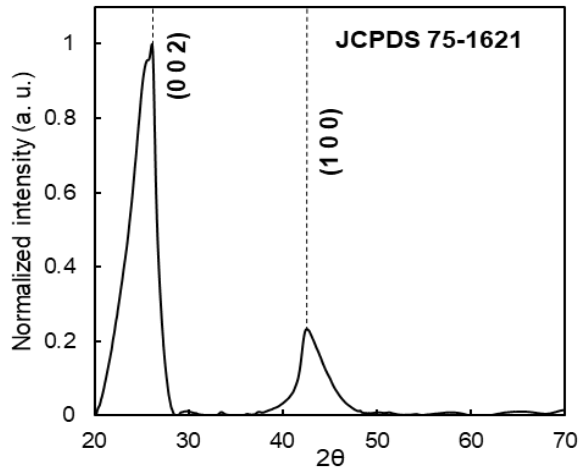
	Position (cm^{-1})	Intensity (a. u.)	FWHM (cm^{-1})	I_{2D}/I_D
Graphene	2667.78	0.84	75.88	1.31
Composite	2676.08	0.69	80.98	1.01

5.3.4 Crystal structure analysis

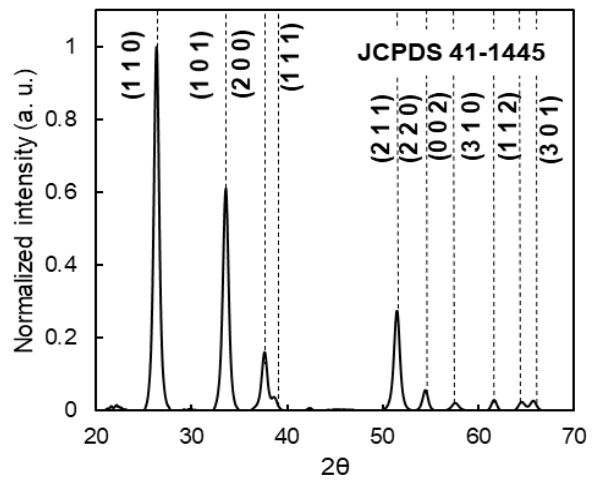
The crystal structure of as-synthesized materials was studied by powder XRD. Figure 5-6 represents recorded XRD patterns of graphene (Fig. 5-6(a)), SnO₂ (Fig. 5-6(b)), and composite (Fig. 5-6(c)). The XRD pattern of graphene consists of 2 peaks; an intense peak at 25.2° is due to the (0 0 2) plane of graphite, the position of this peak is slightly lower than the reported value (26.5°). The peak at 42.4° is due to (1 0 0) plane²¹⁾. Observed peak position in recorded XRD patterns corresponded well with the standard JCPDS data of graphene (No. 75-1621). In the case of SnO₂ XRD pattern, diffraction peaks are associated with the tetragonal SnO₂ structure and their position matches well with standard JCPDS data (No. 41-1445).²²⁾

For the composite XRD pattern, all the peaks of SnO₂ are clearly distinguishable in the pattern and their position is also similar to that of SnO₂ XRD pattern, however, in a composite XRD pattern, diffraction peaks representing graphene didn't appear. Table 5-III represents in detail analysis of XRD pattern of sol-gel synthesized SnO₂ and composite on the basis of position and FWHM of the diffraction peaks. The crystallite size was calculated using Scherrer's equation. The FWHM of diffraction peaks from SnO₂ in composite increased slightly compared to pure SnO₂, a similar change was observed in crystallite size as well. This indicates an increase in crystallinity of SnO₂ in graphene. These observed changes in crystallinity and size could be due to the plasma treatment. A high temperature in the plasma region may have caused the grain growth and grain boundary relaxation resulting change in a size of SnO₂ crystallites.²³⁾

a)



b)



c)

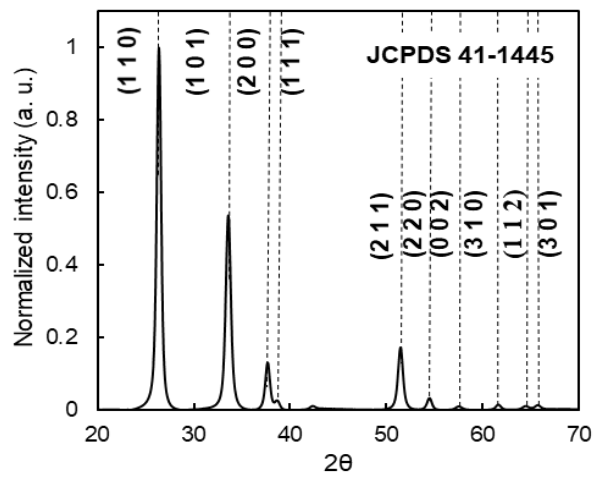
Fig. 5-6 XRD spectra of a) graphene, b) SnO₂, and c) composite.

Table 4-III Analysis of XRD spectra of SnO₂ and composite.

	(h k l)	Position (2θ)	FWHM (2θ)	Size (nm)
SnO ₂	(1 1 0)	26.32	0.686	12.43
	(1 0 1)	33.6	0.758	11.44
	(2 1 1)	51.52	0.792	11.65
Composite	(1 1 0)	26.32	0.560	15.22
	(1 0 1)	33.52	0.641	13.55
	(2 1 1)	51.44	0.563	16.45

5.3.5 Optical properties

Figure 5-7 plots a Tauc plot showing $(\alpha h\nu)^{1/2}$ vs. energy for the SnO₂ and SnO₂-graphene composite plotted using Tauc relationship (eq. 2). Though SnO₂ is a wide gap semiconducting metal oxide, dispersion of SnO₂ into graphene tailored its optical band gap effectively.

The band gap narrowing was observed in the case of the composite (3.4 eV) as compared to sol-gel synthesized SnO₂ (3.6 eV). The band gap narrowing could have resulted from electronic interaction between SnO₂ and graphene sheets.²⁴⁾

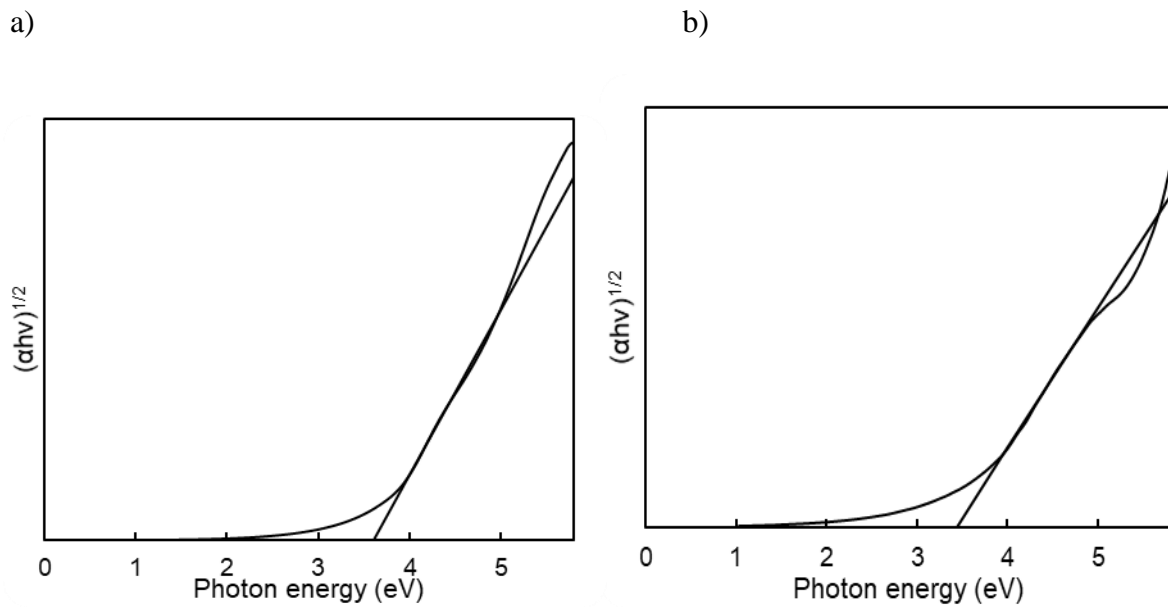


Fig. 5-7 Tauc plot of a) SnO₂ and b) composite,

(cont.)

c)

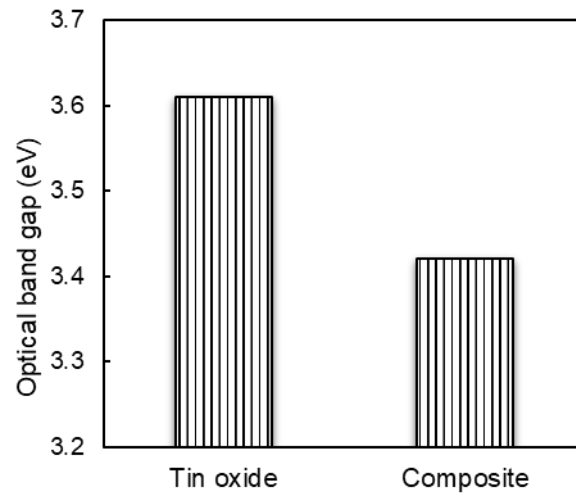


Fig. 5-7 c) Optical band gap of SnO₂ and composite.

5.3.6 Plasma diagnosis

Figure 5-8 shows OES spectra obtained when in-liquid plasma was induced in the ethanol in absence of dispersed SnO_2 nanoparticles (graphene) and in a presence of dispersed SnO_2 nanoparticles (composite) obtained in the range 200 to 900 nm.

For the plasma, emission of OH (310 nm), CH (430 nm), H (488 and 656 nm) and C_2 (474, 516 and 564 nm) were observed in both cases. The author didn't observe any change in the emission peaks as a result of SnO_2 dispersion.

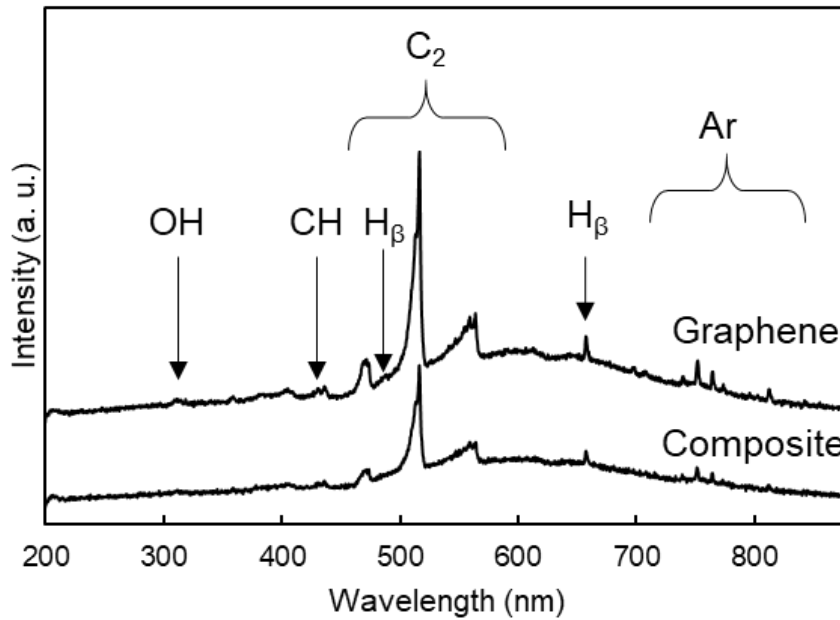


Fig. 5-8 OES in the range 200 to 900 nm of the in-liquid plasma synthesis of graphene and composite.

5.4 Formation mechanism

The mechanism of graphene formation by in-liquid plasma has been discussed previously by our group ^{8,9)}. Figure 5-9 shows schematic of SnO₂-graphene composite. As a result of dispersion of SnO₂ nanoparticles in graphene precursor, SnO₂ nanoparticles interacted with graphene sheets through physisorption/chemisorption, electrostatic binding or charge transfer interaction, thus, SnO₂ nanoparticles mixed well and are distributed uniformly in graphene, covering an almost entire surface of graphene sheets. ²⁵⁾ During the formation of graphene, the carboxyl groups at the edge of the graphene may have acted as anchor sites for SnO₂, as a result, C-O-C band appeared in the FTIR of the composite. The interfacial bonds between the SnO₂ and graphene lead to producing edge disorders in graphene, which was confirmed from Raman analysis. As shown in Fig. 5-9, the SnO₂ nanoparticle attached to graphene flake (around 100 nm long) and contributed towards preventing restacking of graphene, thus SnO₂ gave strong diffraction signals suppressing weaker diffraction from graphene, as a result, no diffraction peak of graphene appeared in XRD spectra of a composite. ²⁶⁾

In previous attempts of synthesizing SnO₂-graphene composite, main focuses were on oxidation of tin chloride in the presence of graphene or reduction of graphene oxide in presence of SnO₂. These approaches successfully synthesized SnO₂-graphene composite, however, it's complicated process was a major issue. In the first approach of tin chloride oxidation in presence of graphene, the graphene was synthesized in advance by traditional graphene synthesis methods by a top-down approach, having low growth speed and high crystallinity of graphene but high temperature for synthesis. Reduction of graphene oxide in presence of SnO₂ is a good technique to synthesize graphene at low temperature but a high amount of precursors and a low synthesis rate were the major issues. On the other hand, in-liquid plasma assisted synthesis method yields the disordered graphene structure in SnO₂-graphene composite easily with a homogeneous distribution of SnO₂ nanoparticles on the graphene surface. ^{5, 26, 27)}

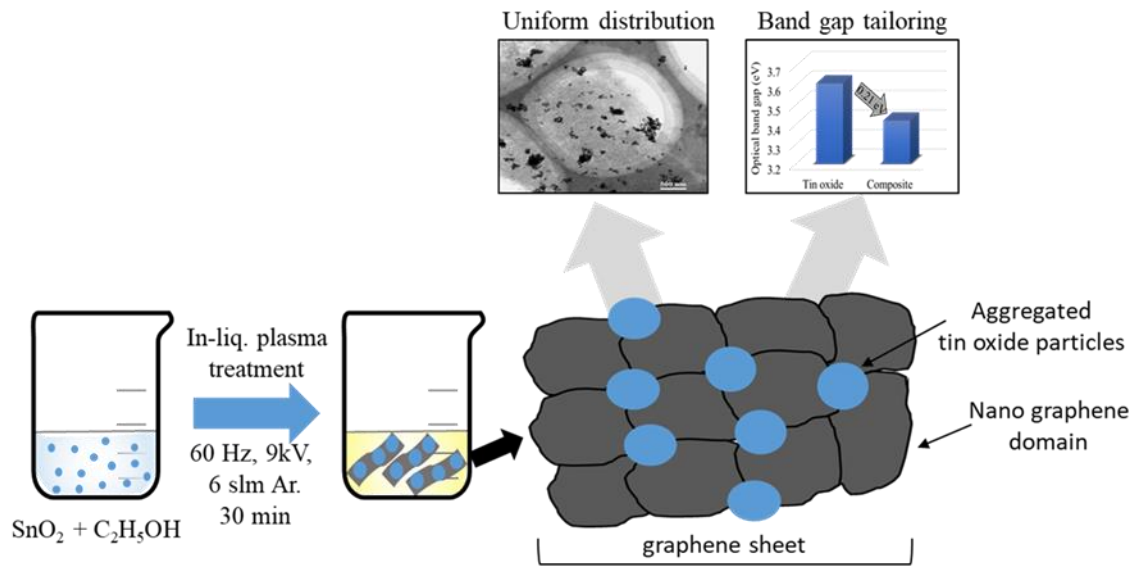


Fig. 5-9 Schematic illustration of the formation mechanism of the composite.

5.5 Post synthesis mixing of SnO₂ and graphene

5.5.1 Overview

Post synthesis mixing of presynthesized SnO₂ nanoparticles and graphene was carried out in order to differentiate the in-liquid plasma enabled hybrid approach of SnO₂-graphene composite synthesis from the *ex-situ* binding methods. In *ex-situ* binding methods for SnO₂-graphene composite formation, the composite formation was carried out by mixing of presynthesized SnO₂ and graphene.⁵⁾ Since, in the hybrid approach, presynthesized SnO₂ nanoparticles were dispersed in ethanol (graphene precursors), it's necessary to differentiate the hybrid approach from the *ex-situ* binding methods for the realization of simplicity and applicability of the hybrid approach for SnO₂-graphene composite synthesis.

5.5.2 Experimental

For the *ex-situ* binding method for composite synthesis, the SnO₂ (8 mg) nanoparticles synthesized by a sol-gel method were dispersed in an in-liquid plasma synthesized solution of graphene for 25 minutes using homogenizer (Tomy Seiko UR-21P), after dispersion the material was collected by filtering the black colored solution with the suction filtration using a membrane filter with pore size of 1 μm and dried at 60°C for 15 minutes (Fig. 5-10). The composite was further analyzed by SEM, XRD, and Raman analysis to investigate the difference between hybrid approach and *ex-situ* method.

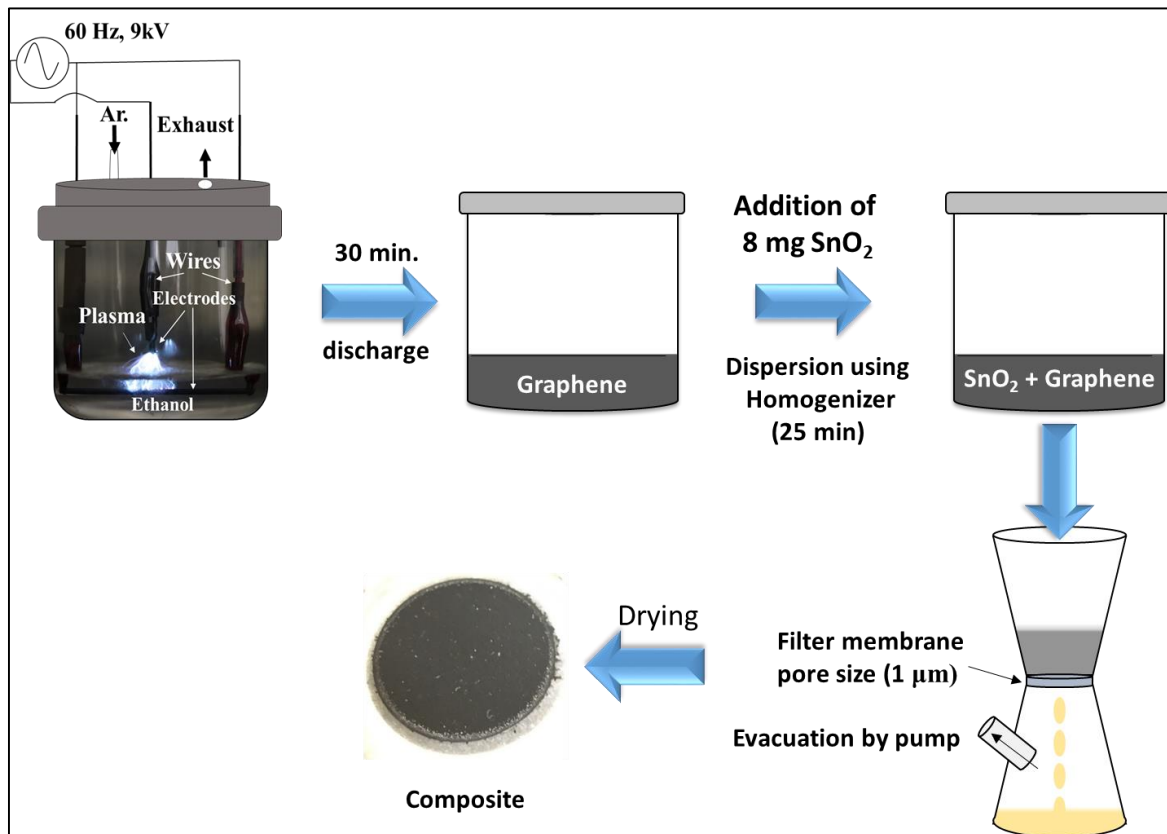


Fig. 5-10 Schematic of the experimental procedure for the composite synthesis by *ex-situ* method.

5.5.3 Surface morphology

The surface morphology of the composite fabricated by *ex-situ* method is shown in Fig. 5-11. The aggregated SnO₂ nanoparticles are clearly visible in the SEM image. Unlike, the composite fabricated by the hybrid method, the SnO₂ nanoparticles are poorly distributed on the graphene sheets. The surface morphology is clearly different than the composite fabricated by the hybrid method. The author believes that in the case of distribution of SnO₂ nanoparticles over graphene sheets, the hybrid approach provides better distribution as compared to *ex-situ* methods.

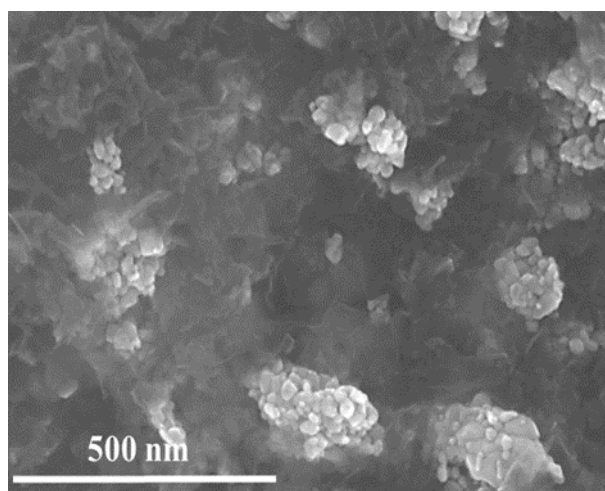


Fig. 5-11 SEM micrograph of the composite fabricated by *ex-situ* method.

5.5.4 Microstructure analysis

Figure 5-12 shows the recorded Raman spectrum of the composite fabricated by *ex-situ* binding method. The Raman spectrum consists of obvious peaks of the graphene and SnO₂ indicating the mutual presence of SnO₂ and graphene in the material. A detailed study of microstructure on the basis of intensity, position, and width of the Raman band peaks is summarized in Tables 5-IV.

We didn't observe any change in position, shape, and intensity of any peak when compared with graphene Raman spectra, summarized in Table 5-IV. Thus, unlike the hybrid method, the graphene in the composite fabricated by *ex-situ* method didn't undergo any microstructural changes. The peak parameters remain unchanged despite mixing with SnO₂ nanoparticles. These observations suggest no interaction between graphene and SnO₂ nanoparticles as an effect of *ex-situ* binding of SnO₂ nanoparticles to graphene.

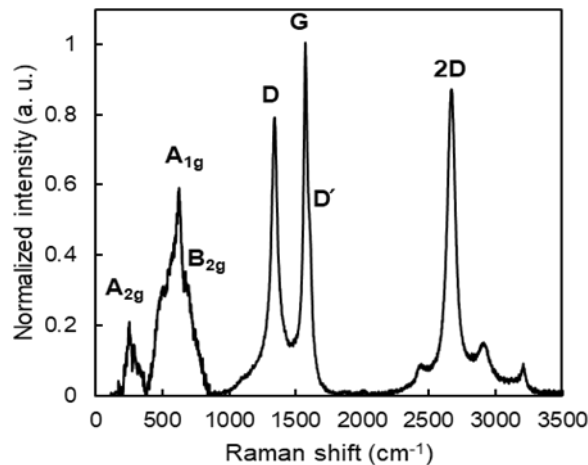


Fig. 5-12 Raman spectrum of the composite fabricated by *ex-situ* method.

Table 5-IV Comparison of Raman band peak parameters.

	G band position (cm ⁻¹)	G band FWHM (cm ⁻¹)	G band Intensity (a. u.)	D band Intensity (a. u.)	2D band Intensity (a. u.)
Graphene	1570.47	35.83	0.83	0.64	0.84
Composite Hybrid method	1575.98	42.19	0.83	0.68	0.69
Composite <i>ex-situ</i> method	1570.31	35.79	0.82	0.64	0.85

5.5.5 Crystal structure analysis

Figure 5-13 is an XRD pattern of the composite fabricated by *ex-situ* binding method. The XRD shows a similar pattern as observed for sol-gel synthesized SnO₂ nanoparticles. The detailed analysis for a position, calculated crystallite size, and comparison with composite fabricated by the hybrid approach and SnO₂ is shown in Table 5-V.

In the case of composite fabricated by a hybrid approach, dispersed SnO₂ nanoparticles undergone in-liquid plasma treatment resulted in the increase in crystallite size but in case of *ex-situ* approach absence of any treatment caused no change in the crystallite size of the SnO₂. However, the absence of diffraction peaks associated with graphene was similar in the case of composite fabricated by *ex-situ* method. This could be due to the aggregated SnO₂ nanoparticles, giving strong diffraction. Based on these observations, the author believes that the composite formation by SnO₂ nanoparticles dispersion in ethanol (graphene precursor) is clearly different from the post synthesise mixing of tin oxide and graphene.

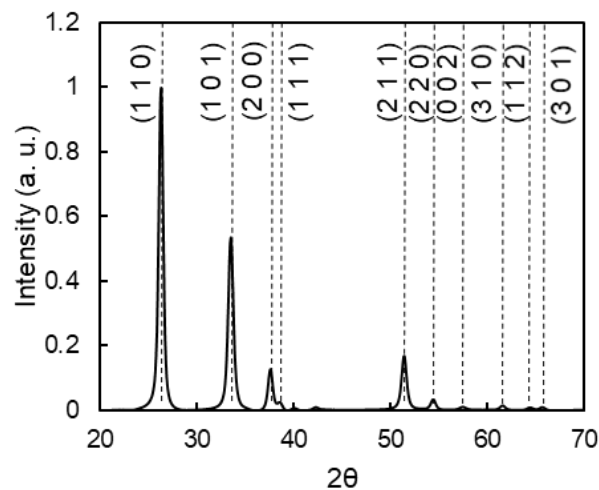


Fig. 5-13 XRD pattern of the composite fabricated by *ex-situ* method.

Table 5-V Comparison of XRD peak parameters.

	(h k l)	Position (2θ)	FWHM (2θ)	Size (nm)
Tin oxide	(1 1 0)	26.32	0.686	12.43
	(1 0 1)	33.6	0.758	11.44
	(2 1 1)	51.52	0.792	11.65
Composite Hybrid approach	(1 1 0)	26.32	0.560	15.22
	(1 0 1)	33.52	0.641	13.55
	(2 1 1)	51.44	0.563	16.45
Composite <i>Ex-situ</i> method	(1 1 0)	26.32	0.671	12.70
	(1 0 1)	33.59	0.743	11.67
	(2 1 1)	51.50	0.790	11.67

5.5.5 Optical properties

Figure 5-13 plots a Tauc plot showing $(\alpha h\nu)^{1/2}$ vs. energy for the SnO₂-graphene composite synthesized by *ex-situ* method plotted using Tauc relationship (eq. 2).

The author didn't observe any change in the optical band of SnO₂ and SnO₂-graphene composite synthesized by *ex-situ* method.

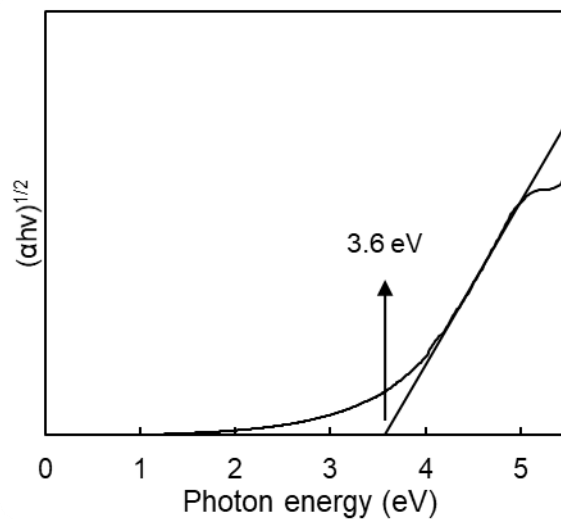


Fig. 5-14 Tauc plot of composite synthesized by *ex-situ* method.

5.6 Conclusion

A hybrid approach for the synthesis of SnO₂-graphene composite based on in-liquid plasma was developed by dispersing SnO₂ nanoparticles in ethanol, which was a single precursor for graphene. The surface morphology, as seen from the SEM and EDS, a uniform distribution of SnO₂ nanoparticles on the flaky graphene sheets was observed. As perceived from TEM, the average size of SnO₂ nanoparticles was around 30 nm, and from EDS, the elemental confirmation of C, O, and Sn was carried out.

The chemical composition of the composite as studied from FTIR showed a presence of absorbance bands of SnO₂ and graphene indicates the formation of SnO₂-graphene composite. As an effect of dispersion of SnO₂ nanoparticles in ethanol, the graphene underwent microstructural changes. As seen from the comparison between graphene and composite Raman spectra for microstructure evaluation, SnO₂ dispersion in ethanol lead to form less crystalline graphene. The composite XRD spectra showed sharp peaks associated with the SnO₂ tetragonal structure, suggesting the presence of well crystalline SnO₂ nanoparticles in the composite. The position of these peaks matched well with the standard JCPDS data of SnO₂. In the composite XRD spectra, the diffraction peaks related to graphene were absent, suggesting prevented restacking of graphene. The change in crystallite size was observed from XRD. The average crystallite size of SnO₂ increased from 12 nm to 16 nm as an effect of in-liquid plasma treatment. The band gap narrowing was observed in the case of the composite as compared to sol-gel synthesized SnO₂ due to electronic interaction between dispersed SnO₂ nanoparticles and graphene sheets.

Next, the difference between *ex-situ* binding methods and hybrid approach for SnO₂ – graphene composite synthesis was stated. The surface morphology of composite fabricated by *ex-situ* method showed poorly distributed and aggregated SnO₂ nanoparticles over graphene sheets. Composite synthesized by *ex-situ* method didn't show change in the optical band gap.

The synthesis approach in this study is simple, low cost, atmospheric pressure, and room temperature operation and can be easily scalable to fabricate devices based on the SnO₂-graphene composite.

References:

- 1) S. Gupta-Chatterjee, S. Chatterjee, A. Ray, and A. Chakraborty, *Sensors Actuators B* **221**, 1170 (2015).
- 2) T. Kuila, S. Bose, A. Mishra, P. Khanra, N. Kim, and J. Lee, *J. Prog. Mater. Sci.* **57**, 1061 (2012).
- 3) M. Ortila, C. Faugeras, P. Plochocka, P. Neugebauer, G. Martinez, D. K. Maude, A. L. Barra, M. Sprinkle, C. Berger, W. A. de Heer, and M. Potemski, *Phys. Rev. Lett.* **101**, 267601 (2008).
- 4) C.N. R. Rao, A. Sood, K. Subrahmanyam, and A. Govindaraj, *Angew. Chem. Int. Ed.* **48**, 7752 (2009).
- 5) M. Khan, M. Tahir, S. Adil, H. Khan, M. Siddiqui, A. Al-warthan, and W. Tremel, *J. Mater. Chem. A* **3**, 18753 (2015).
- 6) A. Genose, and D. Scanlon, *J. Mater. Chem. C* **4**, 1467 (2016).
- 7) T. Hagino, H. Kondo, K. Ishikawa, M. Sekine, and M. Hori, *Appl. Phys. Lett.* **5**, 35101 (2012).
- 8) A. Ando, K. Ishikawa, H. Kondo, T. Tsutsumi, K. Takeda, T. Ohta, M. Ito, M. Hiramatsu, M. Sekine, and M. Hori, *Jpn. J. Appl. Phys.* **57**, 026201 (2018).
- 9) T. Amano, H. Kondo, K. Takeda, K. Ishikawa, M. Hiramatsu, M. Sekine, and M. Hori, *J. Appl. Phys.* **57**, 045101 (2018).
- 10) S. Arote, and V. Tabhane, *Indian J. Pure Appl. Phys.* **56**, 7 (2018).
- 11) V. L. Bonch-Bruевич, *The Optical Properties of Solids* (Academic Press, New York, and London) (1966).
- 12) R. Abruzzi, B. Deavid, and M. Pires, *Cerâmica* **61**, 328 (2015).
- 13) Z. Li, Y. Wang, A. Kozbial, G. Shenoy, F. Zhou, R. McGinley, P. Ireland, B. Morganstein, A. Kunkel, S. Surwade, L. Li, and H. Liu, *Nat. Mater.* **12**, 925 (2013).
- 14) M. Naebe, J. Wang, A. Amini, H. Khayyam, N. Hameed, L. Li, Y. Chen, and B. Fox, *Sci. Rep.* **4**, 4375 (2014).

- 15) D. S. Knight, and W. B. White, *J. Mater. Res.* **4**, 385 (1989).
- 16) A. C. Ferrari, *Solid State Commun.* **143**, 47 (2007).
- 17) G. Bottari, M. Herranz, L. Wibmer, M. Volland, L. Rodriguez-Perez, D. M. Guldi, A. Hirsch, N. Martin, F. D'Souza, and T. Torres, *Chem. Soc. Rev.* **46**, 4464 (2017).
- 18) A. Diéguez, A. Romano-Rodríguez, A. Vilà, and J. R. Morante, *J. Appl. Phys.* **90**, 1550 (2001).
- 19) L. Malard, M. Pimenta, G. Dresselhaus, and M. Dresselhaus, *Phys. Rep.* **473**, 51 (2009).
- 20) A. Eckman, A. Felten, I. Verzhbitskiy, R. Davey, and C. Casiraghi, *Phys. Rev. B - Condens. Matter Mater. Phys.* **88**, 1 (2013).
- 21) B. Andonovic, A. Grozdanov, P. Paunović, and A. T. Dimitrov, *Micro Nano Lett.* **10**, 683 (2015).
- 22) J. Zhang, and L. Gao, *Solid State Chem.* **177**, 1425 (2004).
- 23) D. Bober, M. Kumar, and T. Rupert, *Acta Mater.* **86**, 43 (2015).
- 24) X. Pan, and Z. Yi, *Appl. Mater. Interfaces* **7**, 27167 (2015).
- 25) P. Lian, X. Zhu, S. Liang, Z. Li, W. Yang, and H. Wang, *Electrochim. Acta* **56**, 4532 (2011).
- 26) H. Kim, H. Na, Y. Kwon, S. Kang, M. Choi, J. Bang, P. Wu, and S. Kim, *ACS Appl. Mater. Interfaces* **9**, 31667 (2017).
- 27) Z. Abideen, J. Park, H. Kim, and S. Kim, *Nanotechnology* **28**, 35501 (2017).

Chapter 6

One-step, *in-situ* binding of tin oxide nanoparticles to graphene nanosheets by in-liquid plasma

6.1 Introduction

Different approaches have been proposed to fabricate tin oxide-graphene composite, they can be realized in two different methods: *in-situ* binding and *ex-situ* binding. ¹⁾ *Ex-situ* binding involves the mixing of presynthesized tin oxide (SnO₂) nanoparticles (SNp) and graphene nanosheets (GNs). The graphene used to bind with SnO₂ usually synthesized by traditional exfoliation require low pressure and yields the low amount of graphene. ^{2,3)} The chemical vapor deposition (CVD) method is a widely used method for high-quality graphene synthesis but requires a high temperature for deposition. ^{4,5)} Thus, these methods are not suitable for scaling up for application development. *Ex-situ* binding also limits at the distribution of SnO₂ on graphene. ⁶⁾

In-situ binding methods involve simultaneous reduction of graphite oxide or graphene oxide along and tin chloride (SnCl₂ or SnCl₄), offering good distribution of SnO₂ on graphene with a good rate of synthesis. However, the graphene produced in these methods has low crystallinity. ⁷⁾ Since this method has multi-steps involved in the reduction of graphite to get graphene with reducing agents, high amount of precursors is needed. The in-liquid plasma method for nanomaterial synthesis has emerged lately and can be used to synthesize metal nanoparticles, metal oxide nanostructures, carbon nanomaterials and semiconducting nanoparticles due to its unique features, such as non-equilibrium thermodynamics, high

electron densities, excimer generation, etc. ⁸⁾ In this process, energetic electrons (10 eV and above) with a high density in numbers can interact with molecular gases and other solid or liquid precursors to form reactive radical species capable of nucleating nanoparticles without external heating, thus in-liquid plasma method is low-temperature nanomaterial synthesis method than other conventional material synthesis methods. ^{9,10)} Recently, our research group has developed a novel synthesis method for graphene employing in-liquid plasma material synthesis route. ¹¹⁾ With this method, the production cost for graphene has been significantly reduced as this method operates at low temperature and atmospheric pressure and hence, does not require vacuum or heating devices. In-liquid plasma enables synthesis of high-quality graphene at the high rate of synthesis using an alcohol as the only precursor, reducing process complexity. ^{12,13)}

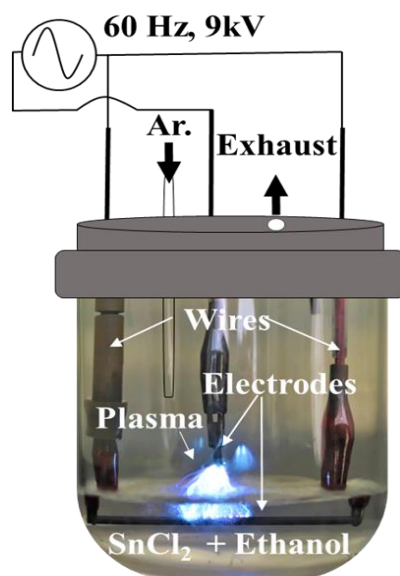
In this work, the aim is to develop a low-cost, *in-situ* process for SNp/GNs composite synthesis with well distributed SNp on high-quality graphene at low temperature and atmospheric pressure. Thus, the tin chloride ($\text{SnCl}_2 \cdot 2\text{H}_2\text{O}$) as a SnO_2 precursor was dissolved in ethanol (graphene precursor) followed by in-liquid plasma treatment to get single step processed SNp/GNs composite in the non-equilibrium field for material synthesis.

6.2 Experimental details

The synthesis approach in this study is a one-step process, as mentioned previously. An 11 mg of tin chloride ($\text{SnCl}_2 \cdot 2\text{H}_2\text{O}$) was dispersed in 100 ml ethanol by a homogenizer (Tomy Seiko UR-21P) in a glass reactor until $\text{SnCl}_2 \cdot 2\text{H}_2\text{O}$ dissolve completely (~ 5 min). Ar gas was introduced into the reactor at the atmospheric pressure with a flow rate of 6 standard-liter-per-minute (slm) to fill the upper part of reactor above the liquid surface. An alternating current (9 kV at 60Hz) was applied to electrodes (3 mm diameter) made of graphite. A sequential discharge occurred between the electrode above the liquid surface and electrode immersed in the liquid through the gas-liquid interface. As shown in Fig. 6-1 (a) A colorless solution was changed to black within a few minutes of plasma discharge.

After a 30 min of the discharge, the synthesized material was collected by filtering the black colored solution with the suction filtration by a membrane filter with pore size of 0.45 μm and dried at 60°C for 10 min. Schematic of an experimental process has been shown in Fig. 6-2 (b). The experimental apparatus and the choice of electrodes and alcohol precursor were based on the preceding studies related to synthesis rate and crystallinity of graphene by liquid-phase plasma synthesis method.^{28,13)} The optical emission from the in-liquid plasma was obtained in the gas phase region close to 3 mm above the liquid surface. The plasma emissions were measured using multi-channel Ocean optics HR-4000 spectrometer in the range between 200 and 900 nm.

a)



b)

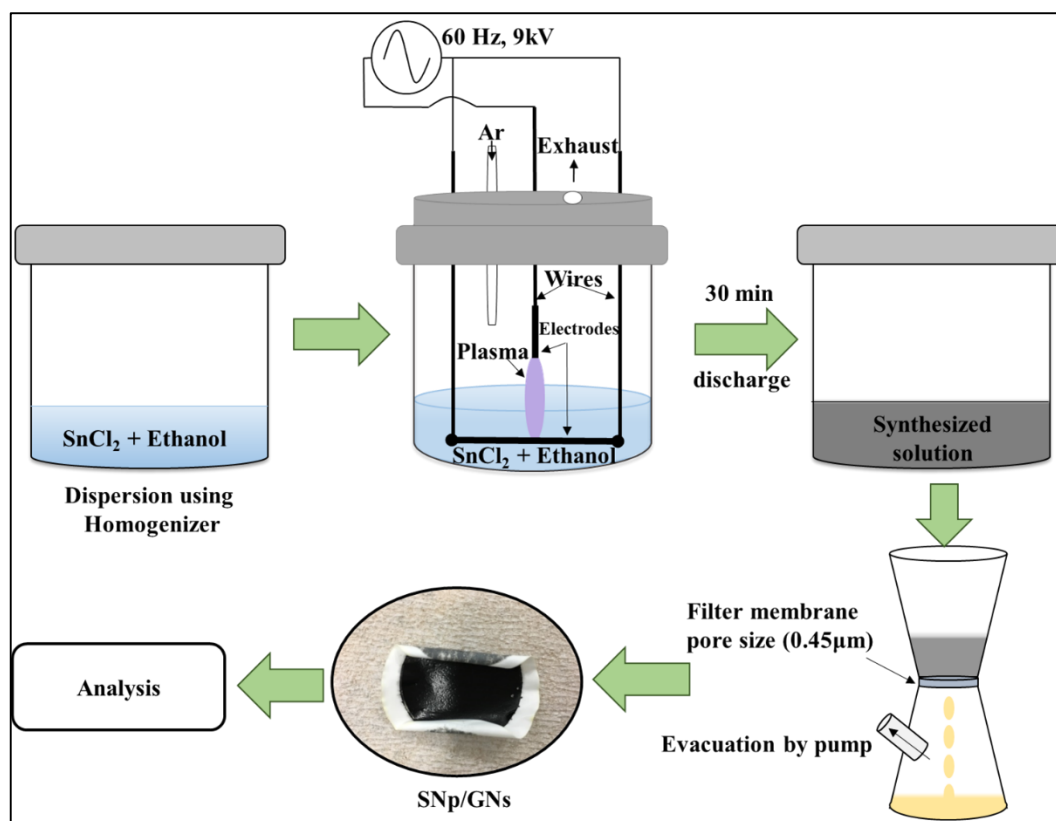


Fig. 6-1 a) Schematic of apparatus used for the experiment, and b) Schematic of an experimental procedure to synthesize Snp/GNs composite.

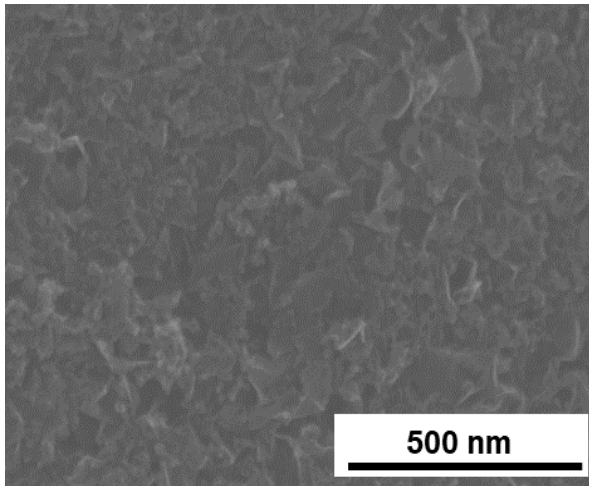
6.3 Results and discussion

6.3.1 Surface morphology and elemental distribution

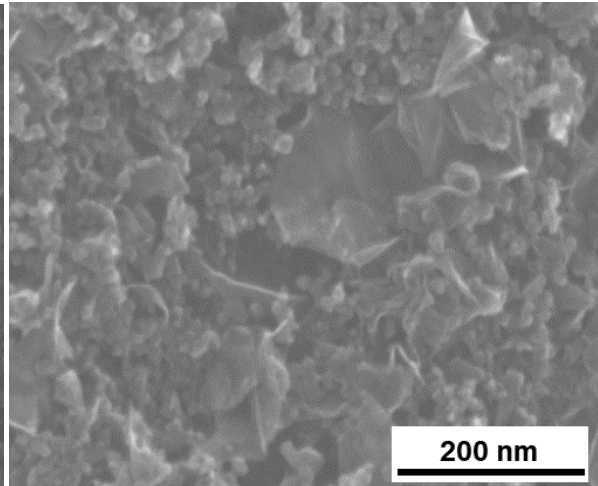
The surface morphology, structure and elemental analysis of SNp/GNs composite were studied by SEM, STEM, and EDS. Figure 6-2 (a and b) are SEM micrographs of SNp/GNs composite, the formation of SnO₂ on crumpled graphene sheets with uniform distribution can be observed. The average length of graphene sheets is from the hundred to few hundred nanometers. The Fig. 6-2 (c) is an EDS map of the composite, clearly showing a uniform distribution of SNps on graphene.

The STEM images of SNp/GNs composite noticeably shown that the SNp were well distributed on graphene sheets (Fig. 6-2 (d, e)). By careful observation, it was detected that some of SNp have dissimilar brightness, these nanoparticles may have enclosed by a thin graphene sheet. This suggests that SNp has attached to both sides of graphene sheets. The average size of these SNp is 2.6 to 3 nm with ± 0.3 nm. Since, the nanoparticles stacked between graphene sheets, the growth of these nanoparticles could have been controlled by graphene sheets. The HRTEM image in Fig. 6-2 (f) shows the clear lattice fringes of 3.53 Å corresponds to (110) plane of SnO₂ and 3.33 Å of (002) plane of graphite, which is similar to the standard JCPDS values. In Fig. 6-2 (g), the elemental analysis of composite has shown to be collected from the image area, it was found that only C, O and Sn elements were detected. The Cu element is from the membrane used for the measurements.

a)



b)



c)

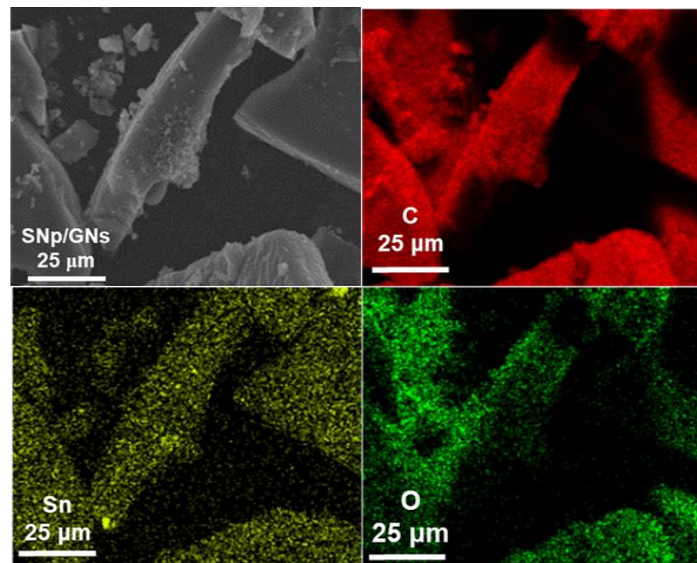
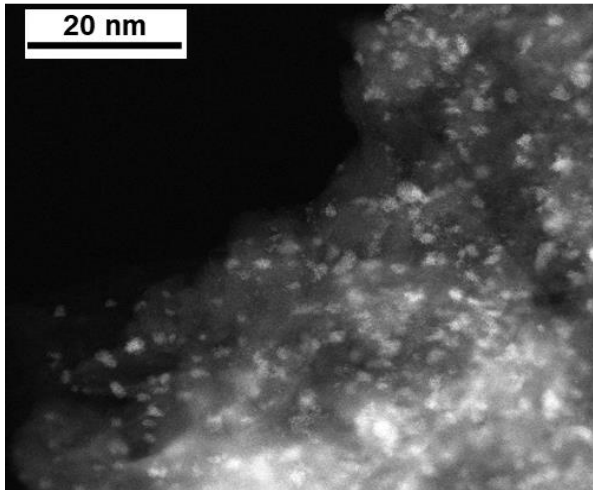


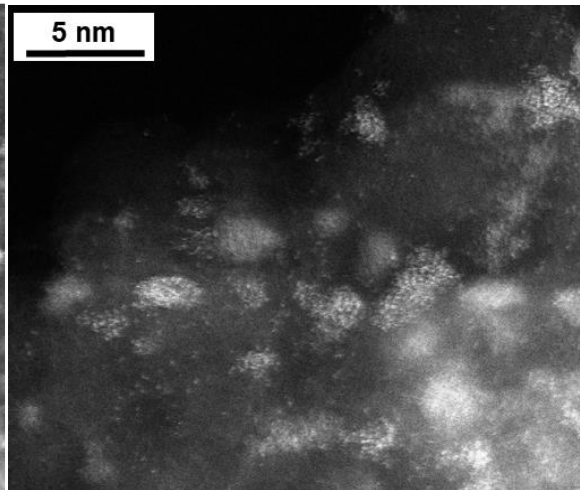
Fig. 6-2 Surface morphology and elemental analysis of SNp/GNs composite (a and b) SEM image, and (c) EDS mapping,

(cont.)

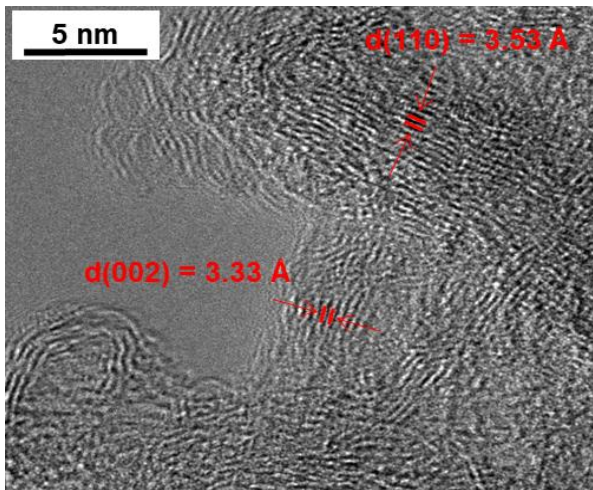
d)



e)



f)



g)

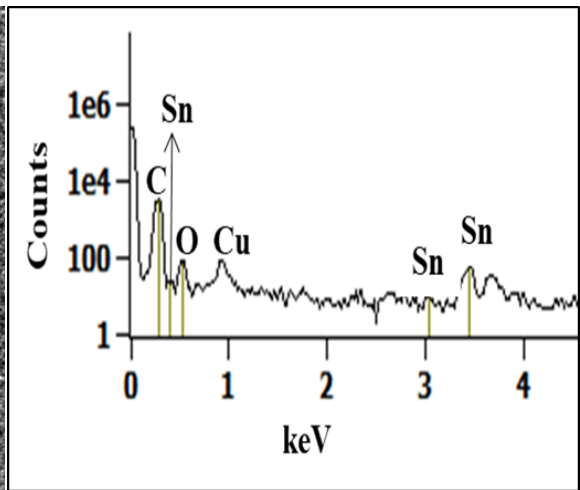


Fig. 6-2 Surface morphology and elemental analysis of SNP/GNs composite (d) Low magnification STEM, (e) High magnification STEM, (f) HRTEM, and (g) EDS analysis.

6.3.2 Microstructure analysis

The presence of SnO₂ on graphene sheets and changes in the microstructure of graphene due to SnO₂ attachment were further confirmed by the Raman analysis. Figure 6-3 (a) shows recorded Raman spectra of pristine graphene and SNP/GNs composite. In the Raman spectra of graphene, characteristic peaks at 1337.0 cm⁻¹, 1570.4 cm⁻¹, 1605.3 cm⁻¹ and 2667.7 cm⁻¹ were clearly observed. The most prominent peaks of graphene are the G-band and 2D-band appearing at 1570.4 cm⁻¹ and 2667.7 cm⁻¹ respectively. G-band and 2D-band peaks are an indication of a six-membered ring structure in the graphene.¹⁵⁾ The peaks at 1337.0 cm⁻¹ and 1605.3 cm⁻¹ are referred to as D-band and D'-band respectively. An occurrence of these peaks is due to the structural disorder.¹⁶⁾

In the case of SNP/GNs composite Raman spectrum (6-3 (b)), the peak around 615 cm⁻¹ is due to the A_{1g} mode and the peak around 250 cm⁻¹ is due to the A_{2g} mode of SnO₂, arising due to vibrations of tin and oxygen atoms.¹⁷⁾ Raman spectra of composite consists all characteristic peaks of graphene, upon comparison of Raman spectra of SNP/GNs composite and graphene, the author observed noticeable decrease (from 1.043 to 0.846) in an intensity ratio of 2D-band and D-band peaks (I_{2D}/I_G) of graphene and composite, this indicates the formation of imperfections in the edge region of the six-membered ring structure of the graphene. These imperfections in the edge region might be due to the presence of SnO₂ in graphene matrix.¹⁸⁾ The intensity ratio of peaks for G-band over D-band was maintained, indicating no effect on the crystallinity of graphene (Graphene: 0.78, Composite:0.79) due to SnO₂ binding to the graphene.¹⁵⁾ The detailed analysis of peak parameters is shown in Table 6-I.

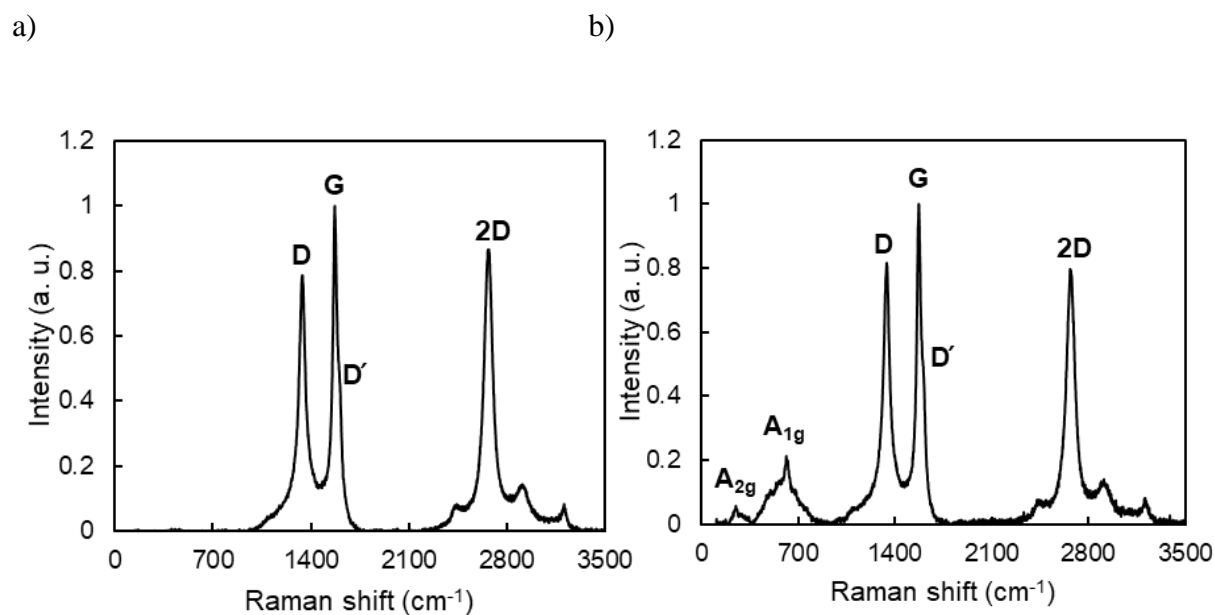


Fig. 6-3 Microstructure analysis of the composite (a) Raman analysis of graphene and, (b) Raman analysis SNp/GNs composite.

Table 6-I Peak parameters of Raman spectra of Graphene and composite.

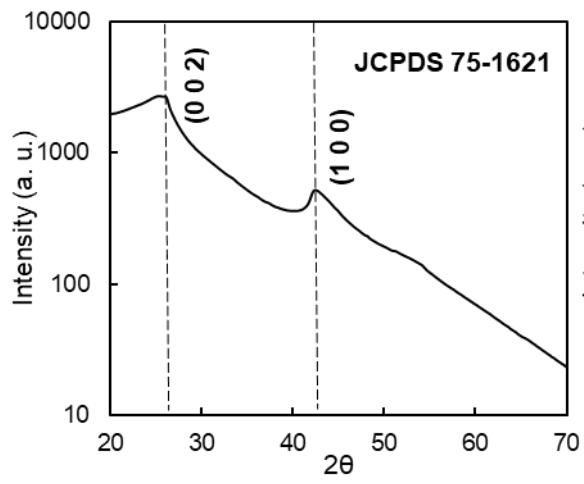
	G band peak intensity (a. u.)	G band peak FWHM (cm ⁻¹)	G band peak Position (cm ⁻¹)	D band peak intensity (a. u.)	2D band peak intensity (a. u.)	I _D /I _G	I _{2D} /I _G
Graphene	0.83	35.83	1570.4	0.65	0.866	0.78	1.043
Composite	0.91	35.43	1570.9	0.72	0.77	0.79	0.846

6.3.3 Crystal structure analysis

The crystallographic properties of SNp/GNs composite and graphene were studied by the XRD and Raman analysis. The diffraction patterns of graphene and SNp/GNs composite are shown in Fig. 6-4 (a) and (b) respectively. The diffraction pattern of pristine graphene shows two strong diffraction peaks associated with (002) and (100) planes of graphite at 25.2° and 42.4° respectively and their position matches well with JCPDS data (75-1621).

In the SNp/GNs composite spectrum, the observed (hkl) peaks are (110), (101), (200), (211), (301) associated with the tetragonal SnO_2 crystal structure (Fig. 6-4(b)). The position of peaks related to tetragonal SnO_2 crystal structure is the same as JCPDS data (41-1445) and lattice constant $a = 4.9 \text{ \AA}$ is almost similar to the standard value for bulk SnO_2 . This indicates the formation of well-crystallized SNp along with graphene. In the SNp/GNs composite spectrum, the peak due to the (002) plane of graphite has been overlapped with a peak due to SnO_2 (110) plane, however, the diffraction peak due to (100) plane of graphite is clearly visible.

a)



b)

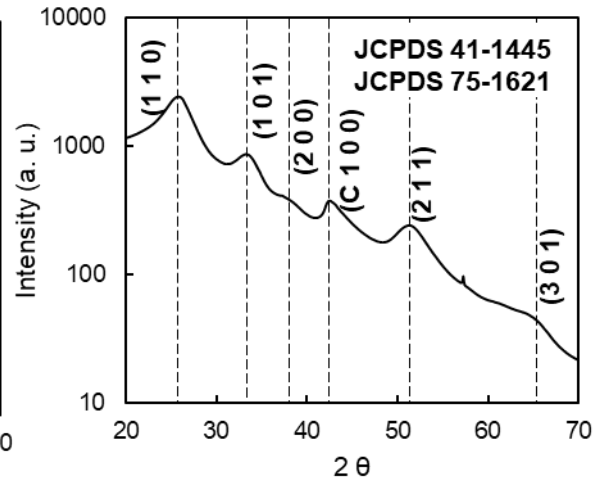


Fig. 6-4 Crystallographic study (a) XRD of graphene, (b) XRD of SNp/GNs composite.

6.3.4 Chemical composition

The FTIR spectra of graphene and SNp/GNs composite are shown in Fig. 6-5. In the graphene spectra, the absorbance band around 1590 cm^{-1} is due to the aromatic C=C stretching and 2921 cm^{-1} is due to the C-H vibrations of methylene groups. The broad peak at 3420 cm^{-1} can be attributed to O-H stretching vibrations of carboxylic group.¹⁹⁾

In the SNp/GNs composite spectra, all associated peaks of graphene emerged. In the SNp/GNs composite spectrum, the main IR features of SnO_2 appeared around 485 and 800 cm^{-1} associated with Sn-O and Sn-O-Sn respectively. The broad peak at 1090 cm^{-1} can be attributed to the Sn-OH vibrations. Thus, the composite FTIR spectrum confirmed the presence of SnO_2 related bonds and O-H bonds in the structure.^{20,21)} In addition, an absorbance peak around 1160 cm^{-1} emerged in the composite spectra. This peak is associated with the C-O-C stretching. The author believes this could be due to the bonding between SnO_2 and graphene.²²⁾

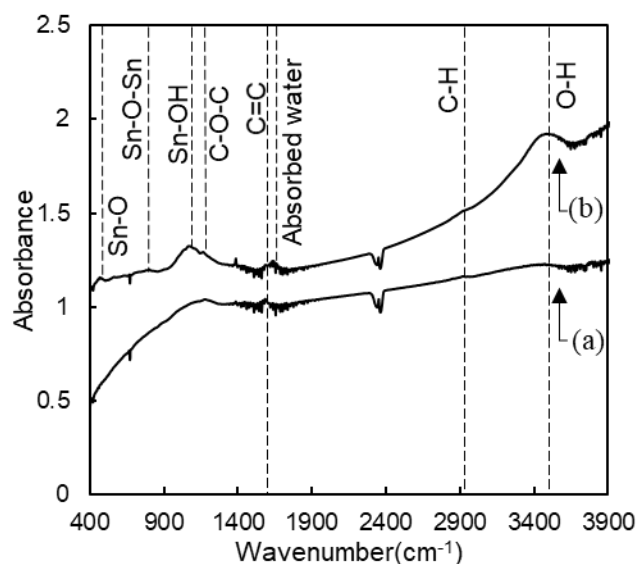


Fig. 6-5 FTIR spectrum of the (a) graphene, and (b) SNp/GNs composite.

6.3.5 Plasma diagnosis

Figure 6-6 shows OES spectra obtained when in-liquid plasma was induced in ethanol (graphene) and in the solution of tin chloride and ethanol (composite) obtained in the range 200 to 900 nm.

For the plasma, emission of OH (310 nm), CH (430 nm), H (488 and 656 nm) and C₂ (474, 516 and 564 nm) were observed in both cases. In the case of plasma in a solution of tin chloride and ethanol (composite), the emission peak of Sn II at 384 nm was observed.²⁹⁾

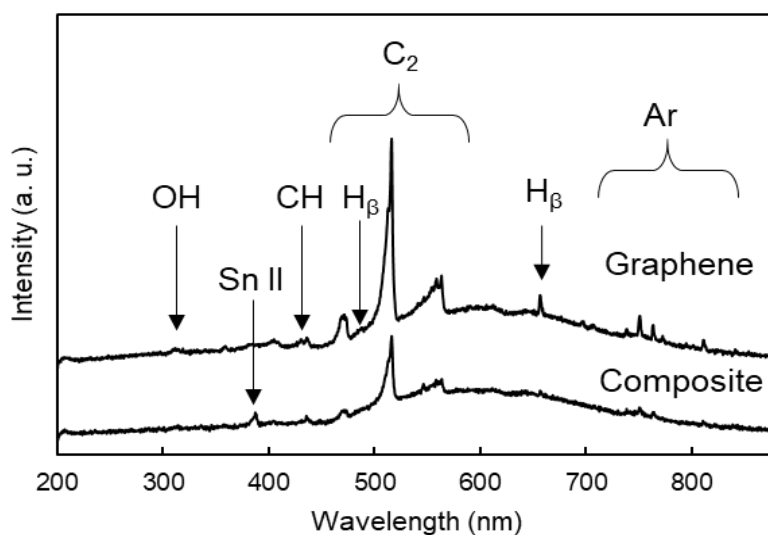


Fig.6-6 OES in the range 200 to 900 nm of the in-liquid plasma synthesis of graphene and composite.

6.4 Formation mechanism

The possible mechanism of formation of SNp/GNs composite has been illustrated in Fig. 6-7. The mechanism of nanographene formation by the in-liquid plasma process has been discussed in detail in previously.^{11,13)} The formation SNp/GNs composite is driven by in-liquid plasma in the non-equilibrium field in a multistep progression involving reduction of precursors, nucleation, and growth, assisting physical collisions of electrons in the plasma. Since the plasma discharge in the liquid phase strongly depends on the conductivity of the liquid, the amount of $\text{SnCl}_2 \cdot 2\text{H}_2\text{O}$ to be added into the 100 ml ethanol was chosen on the basis of optimum conductivity of the liquid for plasma discharge.^{23, 24)}

With the non-equilibrium natures, in the reaction fields under the in-liquid plasma, SnCl_2 undergoes reduction to form Sn^{2+} ions without any external reducing agent. In the other word, the in-liquid plasma provides reaction field with highly excited energy state.²⁵⁾ During graphene synthesis, the in-liquid plasma generates hydroxyl species from alcohol precursor.¹³⁾ The Sn^{2+} cations are possibly bonded with hydroxyl groups as well as carboxyl groups, present in the reaction field. The hydroxyl and carboxyl groups usually attach to graphene at the sheet edges.²⁶⁾ As a result of continuous plasma discharge, the formation of bubbles promotes homogenous dispersion of mixtures. This helps Sn^{2+} ions to distribute uniformly on graphene sheets. Due to the high temperature in the plasma region and the presence of oxygen atoms, Sn^{2+} ions were oxidized to form SnO_2 .²⁷⁾ The SNp attached at edges caused disorders in the six-membered ring structure as observed from Raman analysis.

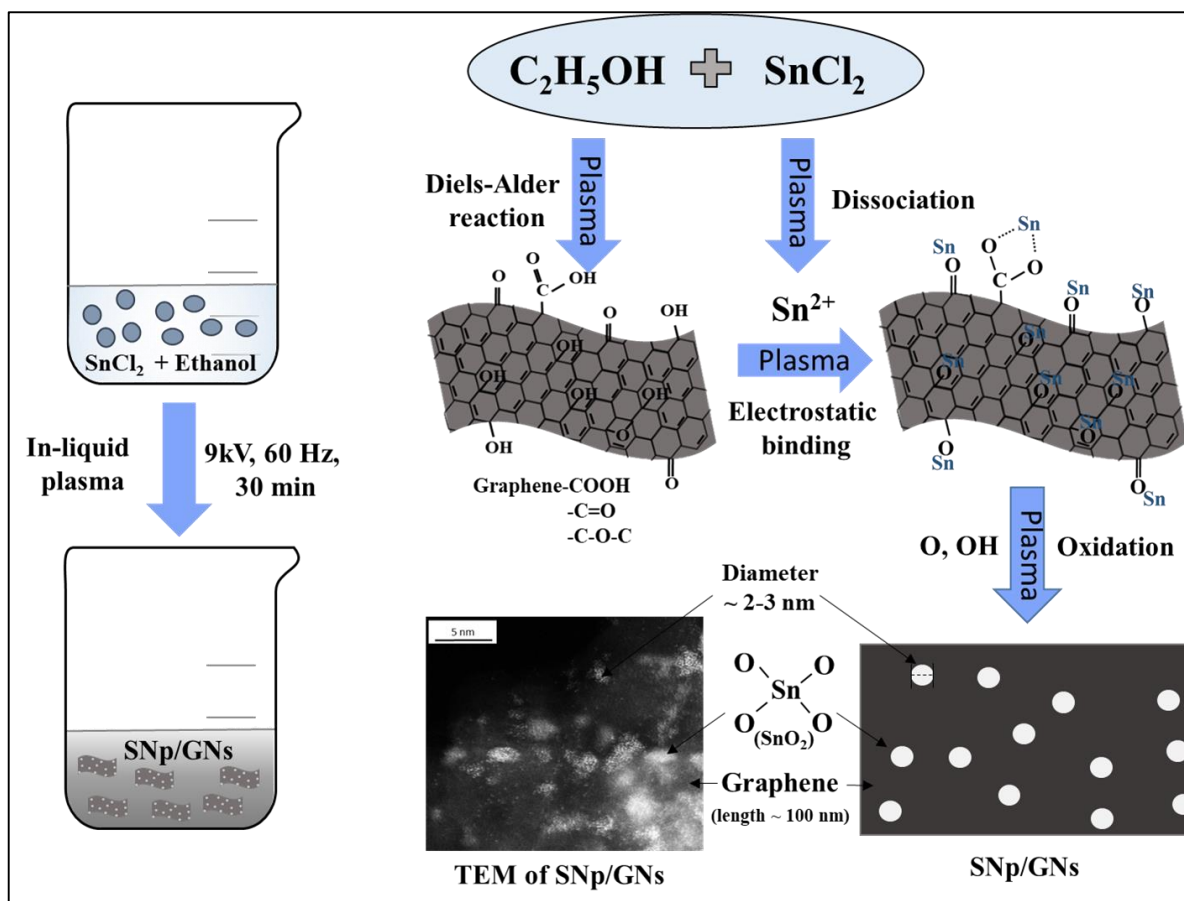


Fig. 6-7 Schematic illustration of the formation mechanism of Snp/GNs composite.

6.5 Conclusion

An *in-situ* approach for the synthesis of SNp/GNs composite synthesis based on in-liquid plasma was developed by dispersing $\text{SnCl}_2 \cdot 2\text{H}_2\text{O}$ in ethanol as single a step process. The simultaneous synthesis of SNp and GNs achieved, the SNp were bound to the GNs in a single-step process without providing external heat and at atmospheric pressure. The surface morphology of the as-synthesized SNp/GNs composite as observed by SEM, the formation of crumpled graphene sheets with uniformly distributed SNp was observed. The average length of graphene sheets was from a hundred to few hundred nanometers. The distribution of SNp on GNs was confirmed by EDS. The STEM analysis showed that SNp has attached to both sides of graphene sheets. The average size of these SNp was 2.6 to 3 nm with ± 0.3 nm. From the HRTEM observation, the clear lattice fringes of clear lattice fringes of 3.53 \AA corresponds to (110) plane of SnO_2 and 3.33 \AA of (002) plane of graphite observed. From the elemental analysis, only C, O and Sn elements were detected in the SNp/GNs composite.

In the crystal structure analysis, the X-ray diffraction pattern of pristine graphene shows two strong diffraction peaks associated with (002) and (100) planes of graphite and the SNp/GNs composite spectrum the peaks associated with the tetragonal SnO_2 crystal structure observed indicating the formation of well-crystallized SNp along with graphene. The microstructure studies by Raman analysis, in the graphene Raman analysis, an occurrence of characteristics peaks of graphene was observed. In the composite Raman spectrum, all characteristic peaks of graphene and SnO_2 appeared. Detailed analysis and comparison of Raman spectra of graphene and composite showed that as a result of composite formation, imperfections in the edge of the six-membered ring structure increased without change in crystallinity of the graphene. The chemical composition of the composite as studied from FTIR showed a presence of absorbance bands of SnO_2 and graphene indicated the formation of SNp/GNs composite. The in-liquid plasma assisted *in-situ* binding method for composite synthesis at atmospheric pressure and low temperature exhibits a simple, low cost, and can be easily scalable to fabricate devices based on the SNp/GNs composite

References:

- 1) M. Khan, M. N. Tahir, S. F. Adil, H. U. Khan, M. R. H Siddiqui, A. A. Al-Warthan, and W. Tremel, *J. Mater. Chem. A* **3** (37), 18753–18808 (2015).
- 2) Y. Huang, E. Sutter, N. N. Shi, J. Zheng, T. Yang, D. Englund, H. J. Gao, and P. Sutter, *ACS Nano* **9** (11), 10612–10620(2015).
- 3) M. Cai, R. A. Outlaw, R. A. Quinlan, D. Premathilake, S. M. Butler, and J. R. Miller, *ACS Nano* **8** (6), 5873–5882(2014).
- 4) D. H. Seo, S. Yick, S. Pineda, D. Su, G. Wang, Z. J. Han, and K. Ostrikov, *ACS Sustain. Chem. Eng.* **3** (3), 544–551(2015).
- 5) L. Lin, B. Deng, J. Sun, H. Peng, and Z. Liu, *Chem. Rev.* **118**, 9281–9343 (2018).
- 6) H. Bai, C. Li, and G. Shi, *Adv. Mater.* **23** (9), 1089–1115 (2011).
- 7) J. Yao, X. Shen, B. Wang, H. Liu, and G. Wang, *Electrochem. commun.* **11** (10), 1849–1852 (2009).
- 8) J. A. McKenna, J. Patel, S. Mitra, N. Soin, V. Švrček, P. Maguire, and D. Mariotti, *Eur. Phys. J. Appl. Phys.* **56** (2), 24020 (2011).
- 9) W. H. Chiang, C. Richmonds, and R. M.Sankaran, *Plasma Sources Sci. Technol.* **19** (3) (2010).
- 10) D. Mohanta, and M. Ahmaruzzaman, *RSC Adv.* **6** (112), 110996–111015 (2016).
- 11) T. Hagino, H. Kondo, K. Ishikawa, H. Kano, M. Sekine, and M. Hori, *Appl. Phys. Express* **5** (3) (2012).
- 12) T. Amano, H. Kondo, K. Ishikawa, T. Tsutsumi, K. Takeda, M. Hiramatsu, M.Sekine, and M. Hori, *Jpn. J. Appl. Phys.* **11**, 15102 (2018).
- 13) A. Ando, K. Ishikawa, H.Kondo, T.Tsutsumi, K. Takeda, and T. Ohta, M. Ito, M. Hiramatsu, M. Sekine, and M. Hori, *Jpn. J. Appl. Phys.* **57**, 026201(2018).
- 14) R. R. Borude, H. Sugiura, K. Ishikawa, T. Tsutsumi, H. Kondo, and M. Hori, *J. Phys. D: Appl. Phys.* Submitted for publication (2018).
- 15) A. C. Ferrari, *Solid State Commun.* **143** (1–2), 47–57 (2007).
- 16) C. Lenardi, P. Piseri, V. Briois, C. E. Bottani, A. Li Bassi, and P. Milani, *J. Appl.*

- Phys.* **85** (10), 7159–7167 (1999).
- 17) A. Diéguez, A. Romano-Rodríguez, A. Vilà, and J. R. Morante, *J. Appl. Phys.* **90** (3), 1550–1557 (2001).
 - 18) L. M. Malard, M. A. Pimenta, G. Dresselhaus, and M. S. Dresselhaus, *Phys. Rep.* **473** (5–6), 51–87 (2009).
 - 19) M. Naebe, J. Wang, A. Amini, H. Khayyam, N. Hameed, L. H. Li, Y. Chen, and B. Fox, *Sci. Rep.* **4**, 1–7 (2014).
 - 20) R. Malik, P. S. Rana, and S. Duhan, *Energy Environ. Focus* **4**, 340 (2015).
 - 21) R. C. Abruzzi, B. A. Dedavid, M. J. R. Pires, and P. Alegre, *Ceramica* **61**, 328 (2015).
 - 22) W. J. Kim, S. W. Lee, and Y. Sohn, *Sci. Rep.* **5**, 13448 (2015).
 - 23) P. J. Bruggeman, M. J. Kushner, B. R. Locke, J. G. E. Gardeniers, W. G. Graham, D. B. Graves, R. C. H. M. Hofman-Caris, D. Maric, J. P. Reid, E. Ceriani, D. Fernandez Rivas, J. E. Foster, S. C. Garrick, Y. Gorbanev, S. Hamaguchi, F. Iza, H. Jablonowski, E. Klimova, J. Kolb, F. Krcma, P. Lukes, Z. Machala, I. Marinov, D. Mariotti, S. Mededovic Thagard, D. Minakata, E. C. Neyts, J. Pawlat, Z. Lj. Petrovic, R. Pflieger, S. Reuter, D. C. Schram, S. Schröter, M. Shiraiwa, B. Tarabová, P. A. Tsai, J. R. R. Verlet, T. von Woedtke, K. R. Wilson, K. Yasui and G. Zvereva, *Plasma Sources Sci. Technol.* **25**, 53002 (2016).
 - 24) K. Shih, and B. R. Locke, *Plasma Process. Polym.* **6**, 729 (2009).
 - 25) Q. Chen, J. Li, and Y. Li, *J. Phys. D. Appl. Phys.* **48** (42), 424005 (2015).
 - 26) C. Chen, L. Wang, Y. Liu, Z. Chen, D. Pan, Z. Li, Z. Jiao, P. Hu, C. Shek,; C. M. L. Wu, J. K. L. Lai, and M. Wu, *Langmuir* **29**, 4111 (2013).
 - 27) L. Zhao, M. Choi, H. Kim, X. Lei, W. Rui, L. Yong, S. Banerjee, and A. Bumajdad, *Jpn. J. Appl. Phys.* **55**, 01AE17 (2016).
 - 28) T. Amano, H. Kondo, K. Takeda, K. Ishikawa, and M. Hori, *Jpn. J. Appl. Phys.* **57**, 045101 (2018).
 - 29) J. Zhang, X. Hu, J. Shi, P. Lu, X. Shen, P. Xu, and N. Saito, *Jpn. J. Appl. Phys.* **55**, 01AE17 (2016)

Chapter 7

Conclusions and future perspectives

7.1 Summary of this dissertation

In this dissertation, from the viewpoint that the plasma processes are advantageous to surface modification and nanomaterial synthesis, the surface modification of carbon films and tin oxide-graphene (SnO_2 -graphene) nanocomposite formation was clarified. In the case of the composite, the applicability of *ex-situ* and *in-situ* binding methods was clarified. It was realized that SnO_2 -graphene composite can be synthesized at the relatively low temperature and atmospheric pressure in a single step by in-liquid plasma. Upon studying gas sensing response of SnO_2 -polyaniline (Sn-PANI) composite, it was suggested that the composite has a better gas sensing response at room temperature than its component materials due to an overall increase in surface area for gas adsorption and formation of a p-n junction between p-type PANI and n-type SnO_2 . The chapter wise findings are summarized below.

In chapter 1, the structures, properties and point of view for application development of metal oxides (SnO_2), conducting polymers (PANI), carbon materials (graphene) and composite based on SnO_2 , polyaniline, and graphene are described. The need for composites and problems associated with traditional composite formation approaches are summarized. The author has pointed out that the traditional graphene synthesis methods are not suitable for graphene-based composite synthesis, the in-liquid plasma assisted graphene synthesis can be superior to the composite for the graphene-based composite synthesis.

In chapter 2, the synthesis methods for SnO_2 , PANI, carbon films and graphene were described. The atmospheric pressure plasma surface treatment process and apparatus were also described. Various material evaluation methods were discussed along with their operational

principle. The gas sensing measurement set up and sample preparation for gas sensing measurement was shown and discussed.

In chapter 3, the sensing properties of Sn-PANI composite synthesized by *ex-situ* approach has shown. The composite was synthesized by mixing SnO₂ and PANI powders and grinding together. The surface morphological, crystal structure and chemical composition studies showed the mutual presence of SnO₂ and PANI in a composite sample. The composite showed improvement of ammonia gas and humidity sensing response at room temperature. The synergetic effect due to the addition of SnO₂ improved gas sensing characteristics in the case of the composite.

In chapter 4, surface and bulk modification of magnetron sputtered carbon films were achieved by the atmospheric pressure plasma (APP) treatment and controlling process parameters during deposition. A relationship between surface/bulk structures and optical/electrical properties of carbon was studied. It was found that variation in power density during deposition can control bulk and surface properties of the carbon films. As an effect of post APP treatment, the surface roughness of carbon films increased with treatment time along with the selective removal of sp² clusters. The removal of sp² clusters was observed by NEXAFS studies. The APP treatment caused the increase in the sheet resistance as well as the optical band gap of the carbon films. Consequently, the author developed a technique to control structural, optical and electrical properties for bulk and surface of the magnetron-sputtered carbon films, by controlling power density variation during deposition and the subsequent APP treatments.

In chapter 5, a hybrid approach for SnO₂-graphene composite synthesis has been discussed. A hybrid approach for SnO₂-graphene composite formation based on the in-liquid plasma was developed by dispersing SnO₂ nanoparticles in ethanol, which was a single precursor for the graphene. A uniform distribution of SnO₂ nanoparticles on graphene sheets was achieved. As found in the Raman analysis and XRD, the SnO₂ dispersion caused the formation of disorder and less crystalline graphene.

The studied hybrid approach was simple, low cost, atmospheric pressure, and room temperature operation and can be easily scalable to fabricate gas sensing devices based on

SnO₂-graphene composite.

In chapter 6, an *in-situ* approach for SnO₂-graphene composite synthesis has been discussed. The *in-situ* binding of SnO₂ nanoparticles to graphene sheets by in-liquid plasma method was achieved to fabricate SnO₂-graphene composite at low temperature and atmospheric pressure in a single step processing using dissolved SnCl₂ in ethanol as the only precursor. As observed from TEM, SnO₂ nanoparticles of size around 2-3 nm were uniformly distributed and attached to both sides of graphene sheets. XRD and Raman analysis showed the formation of well-crystalline materials. The chemical composition studies from FTIR showed SnO₂ and graphene functional groups indicating the formation of SnO₂-graphene composite. The studied *in-situ* binding synthesis route was facile, low cost and can be easily used to fabricate devices based on SnO₂-graphene composite.

The author found that plasma processes are advantageous for the surface modification of carbon films and synthesis of graphene-based composite due to non-equilibrium physical-chemical process as a result of plasma. The graphene-based composite can be formed by *in-situ*, *ex-situ* and hybrid approaches using in-liquid plasma efficiently at relatively low temperature, atmospheric pressure with single step processing, which collectively reduced the complexity of the composite formation process.

Since in-liquid plasma has a big role in nanomaterial synthesis, the author thinks that the in-depth study of the plasma process is necessary. During this study, the primary plasma analysis was carried out to obtain information regarding plasma chemistry by light emission in the gas phase. The author couldn't measure the light emission in the liquid phase as solvent changed its color to black as a result of a plasma discharge to form carbon leading to attenuation of light emission. It is also necessary to study plasma process parameters collectively to understand the influence on nanomaterial synthesis.

7.2 Scopes for future works

It was found that SnO₂-polyaniline (Sn-PANI) composite synthesized by *ex-situ* approach has improved gas sensing properties. In this synthesis approach, there was no control over SnO₂ particles size, it is necessary to control the size and shape of SnO₂ particles for better results from the nanostructured SnO₂. The *ex-situ* approach proved to be a cost-effective option for composite formation. However, the surface morphology and SnO₂ distribution on PANI were out of control, considering this, it is necessary to study other approaches for Sn-PANI the composite formation. In addition, during the gas sensing measurement, due to limitations of gas sensing set-up, the gas response of Sn-PANI composite to only 100 ppm concentration of ammonia was checked, it is necessary to find the lowest detection limit with modifications in the gas sensing set-up. In addition to this, the fundamental questions about why sensor response increased as an Sn-PANI composite, how to tune the properties of Sn-PANI composite for future prototype development are needed to be addressed in the future. Since the in-liquid plasma method offers an easy and cost-effective process for composite formation, it is necessary to introduce the promising in-liquid plasma method to synthesize Sn-PANI composite in near future.

Next, the control over surface and bulk properties of carbon films were achieved by the APP treatment. It is necessary to employ the APP treatment for real-time application development such as gas sensing. The effect of plasma process parameters and mechanism of plasma process have to be studied. In addition to this, it is obligatory to study an effect of the APP treatment on the SnO₂-graphene composite as the APP treatment significantly modifies the structural and chemical properties of the surface.

Then, the author successfully employed the in-liquid plasma method for graphene-based composite by *ex-situ*, *in-situ* and hybrid approaches. In the case of a hybrid approach for SnO₂-graphene composite synthesis, it is necessary to study the effect of plasma discharge on dispersed SnO₂ nanoparticles. In the same experiment, the aggregation of SnO₂ nanoparticles was observed, more studies are required to control the aggregation of SnO₂ nanoparticles after plasma discharge. In the case of in-liquid plasmas assisted *in-situ* approach, the smaller size of

SnO₂ nanoparticles was observed (2~3 nm), however, the mechanism of this small size particle generation is not established. It is important to study further to establish the mechanism of nanocomposite formation by in-liquid plasma. In the above experiments, the plasma parameters were same, the effect of plasma parameters on size and structure of the composite should be evaluated in future.

The prime importance was given to check the applicability of plasma processes for material surface modification and one-step composite formation considering the step by step targets. In future, the application development based on surface modified carbon films and SnO₂-graphene composite is necessary. The formed SnO₂-graphene composite can be utilized as a gas sensing material in future with the film formation and as an electrode material in batteries. The in-liquid plasma method can be employed for composite based on graphene and other metal oxides. Along with this, the relation between plasma parameters and material synthesis has to be studied in order to expand the field of plasma processes for material synthesis.

Acknowledgments

The present research was performed in Professor Hori and Professor Ishikawa Laboratory, Department of Electrical Engineering and Computer Science, Nagoya University. The author would like to appreciate his research advisor, Professor Masaru Hori, Institute of Innovation for Future Society, Nagoya University, for his guidance, advice, and encouragements throughout the course of this research. The author also would like to thank his vice-advisors, Professor Kenji Ishikawa, Plasma Nanotechnology Research Center, Nagoya University, and Associate Professor Hiroki Kondo, Plasma Nanotechnology Research Center, Nagoya University, for valuable guidance and support. The author also would like to thank his vice-advisers, Professor Noriyasu Ohno, Department of Electrical Engineering, Nagoya University, Professor Hirotaka Toyoda, Department of Electrical Engineering, Nagoya University, and Professor Motonobu Goto, Department of Material Science and Engineering, Nagoya University, for their guidance and valuable suggestions in preparing this dissertation.

The author is enormously grateful to Professor Makoto Sekine, Professor Osamu Oda, Professor Toshio Hayashi, Professor Hitoshi Ito, Professor Naohiro Shimizu, Assistant Professor Takayoshi Tsutsumi, Plasma Nanotechnology Research Center, Nagoya University, Lecturer Hiromasa Tanaka, and Assistant professor Hiroshi Hashizume, Institute of Innovation for Future Society, Nagoya University, Professor Jeon Geon Han and Mr. Bibhuti Bhusan Sahu, Sungkyunkwan University, South Korea for their valuable comments and suggestions.

The author also thanks sincerely, Dr. Frank Wilson, Dr. Zecheng Liu, Dr. Naoyuki Kurake, Dr. Atsushi Ando, Dr. Tomoki Amano, Dr. Harry Zhang, Dr. Timothy Ryan Brubaker, Dr. Hirotsugu Sugiura, Dr. Masakazu Tomatsu, Dr. Yusuke Fukunaga, Dr. Shun Imai, Mr. Masato Imamura, Mr. Toshinari Ueyama, Mr. Daiki Kanno, Mr. Ren Kuramashi, Mr. Yukihiro Kurokawa, Ms. Mika Takahashi, Mr. Tomonori Ichikawa, Ms. Moe Okabe, Mr. Xitong Xie, Ms. Yao Han, Ms. Kaede Katsuno, Mr. Naoki Takeda, Mr. Yugo Hosoi, Mr. Kaito Murakami, Mr. Soutarou Yamaoka, Mr. Yasuyuki Ohashi, Mr. Takahiro Omochi, Mr. Takumi Kato, Mr. Kazuya Nakane, Mr. Masaki Hasegawa, Mr. Ryo Hamaji, Mr. Shogo Maeda, Mr. Ni Jiawei, Ms. Liu Yang, Mr. Ozaki Atsushi, Mr. Suda Yuki, Mr. Ryusei Sakai, Mr. Masahiro Hazumi, Mr.

Acknowledgments

Matsumura Shogo, Mr. Moriyama Tatsuyuki, and all other students who have studied in Professor Hori and Professor Ishikawa Laboratory for giving the big pleasure in life and creating a most enjoyable work atmosphere.

The author appreciates Ms. Yoko Kuwabara, Ms. Kanae Teshigawara, Ms. Kazuyo Hirota, Ms. Taeko Terasawa, and Ms. Aya Honda and for assisting in day-to-day life and encouragements. The author also would like to thank staff and professors of Leadership Development Program for Space Exploration and Research including Ms. Atsuko Baba, Ms. Yoshiko Kubo, Ms. Miyuki Seki, Ms. Yoko Mizuno, Prof. Kazutaka Yamaoka, Prof. Hidetaka Tanaka, Prof. Kaisuke Tanaka, Prof. Menjo Hiroki, Prof. Ichiro Nishimoto, Prof. Aoki, and Prof. Hiroyasu Tajima for help and support.

The author is grateful to his mentors and professors from India including Mr. Sandip Purane, Mr. Bajirao Shinde, Mrs. Sulochana Wagh, Mr. Sunil Palande, Mr. Santosh Sonawane, Mr. Bapurao Mali, Prof. Shivaji Sonawane, Prof. Sandip Arote, Prof. Habib Pathan, Prof. Naseem Deshpande, Prof. Jayashree Pant, Prof. Rupesh Patil, Prof. Vinod Dhage, Prof. Vidya Kalyankar, Prof. Pankaj Koinkar, Prof. Bhushan Patil, Prof. Shashikala Gangal and Prof. Sanjay Chakane for their moral support and encouragement.

Some special words of appreciation go to friends who have always been a major source of support when things would get a bit discouraging, the author is thankful to them for being there for him.

Finally, the author expresses his deep sense of gratitude towards his family, Mr. Rohidas S. Borude, Mrs. Sangita R. Borude, Mr. Khandu S. Borude, Mr. Eknath S. Borude, Mr. Sampat S. Borude, Mr. Vishvanath S. Borude, Mrs. Madhuri V. Shinde, Mr. Vishal S. Shinde, Mr. Sandip D. Bansode, his grandparents, uncles, aunts and cousins for their constant love, and blessings.

This dissertation is dedicated to the author's family.



Ranjit Rohidas Borude

February 2019

List of papers

1. Original Papers

Title	Journal	Authors and related chapter
1. Synthesis and characterization of Sn-PANI composite for humidity sensing applications	Journal of Basic and Applied Engineering Research, 2 (16), 1334-1338 (2015).	R. Borude, N. Deshpande, and S. Chakane. (Chapter 3)
2. Sn-PANI synthesis and its application as ammonia gas sensor	Journal of Atomic, Molecular, Condensate and Nano Physics, 3 (2), 73-80 (2016).	R. Borude, N. Deshpande, S. Chakane, and J. Pant. (Chapter 3)
3. Modifications of surface and bulk properties of magnetron-sputtered carbon films employing post treatments of atmospheric pressure plasma.	Japanese Journal of Applied Physics, 58, SAAC07 (2019).	R. Borude, H. Sugiura, K. Ishikawa, T. Tsutsumi, H. Kondo, J. Han, and M. Hori (Chapter 4)
4. Facile synthesis of SnO ₂ -graphene composites employing nonthermal plasma and SnO ₂ nanoparticles-dispersed ethanol.	Journal of Physics D: Applied Physics (In a review)	R. Borude, H. Sugiura, K. Ishikawa, T. Tsutsumi, H. Kondo, and M. Hori. (Chapter 5)
5. Single-step, low-temperature simultaneous formations and <i>in-situ</i> binding of tin oxide nanoparticles to graphene nanosheets by in-liquid plasma.	ACS Applied Nano Materials (In a review)	R. Borude, H. Sugiura, K. Ishikawa, T. Tsutsumi, H. Kondo, N. Ikarashi and M. Hori. (Chapter 6)

List of papers

2. International Conferences

Title	Conference	Authors
1. Study of environment-friendly piezoelectric materials.	International Youth Conference on Water, Climate and Sustainable Energy, Pune, India, Feb. 16-17, 2015.	R. Borude, R. Maral, D. Gote, S. Pandit, and J. Pant
2. Sn-PANI synthesis and its gas sensing applications	Current Developments in Atomic, Molecular, Optical and Nano Physics, Delhi University, Delhi, India, March 11-14, 2015.	R. Borude, N. Deshpande, and S. Chakane.
3. Synthesis and characterization of Sn-PANI composite for humidity sensing applications	International Conference on Contemporary Advances of Science and Technology, Banaras Hindu University, Varanasi, India, Aug. 7-9, 2015.	R. Borude, N. Deshpande, and S. Chakane.
4. Polyaniline blended with tin oxide as NO ₂ gas sensor.	International Workshop on Physics of Semiconductor Devices, Indian Institute of Science, Bangalore, India. Dec. 7-10, 2015.	R. Borude, R. Maral, N. Deshpande, and S. Chakane.
5. Design and development of japanese graphite-based thermal straps for space missions	Space Science and Technology Conference, Niigata Convention Center, Niigata, Japan. Oct. 25-27, 2017.	R. Borude, Y. Guo, S. Tanaka, J. Luang-on, T. Tong, H. Xu, B. Szasz, Y. Sasai, H. Tanaka, D. Ishihara, K. Tamura, H. Nagano, H. Kaneda, and M. Kutsumizu
6. The role of nanoscience in the development of gas sensors. (Invited)	The Asian International Workshop on Plasma Science, Nagoya University, Nagoya, Japan, Feb. 13th, 2016.	R. Borude, N. Deshpande and S. Chakane
7. Plasma surface treatment of carbon films deposited by magnetron sputtering	International Symposium on Advanced Plasma Science and its Applications for Nitrides and Nanomaterials, Meijo University, Nagoya, Japan, March 4-8, 2018.	R. Borude, H. Sugiura, K. Ishikawa, T. Tsutsumi, H. Kondo, J. Han, and M. Hori

List of papers

Title	Conference	Authors
8. Effects of deposition conditions and atmospheric pressure plasma surface treatment on optical and electrical properties of carbon films	International Workshop on Plasma Synthesis of Nanomaterials and its Applications for Sensor Devices, Gifu, Japan, March 11-14, 2018.	R. Borude, H. Sugiura, K. Ishikawa, T. Tsutsumi, H. Kondo, J. Han, and M. Hori
9. Liquid phase plasma assisted synthesis of Tin oxide- Graphene composite	The 79th Japan Society of Applied Physics Autumn Meeting, Nagoya, Japan, Sept. 17-21, 2018.	R. Borude, K. Ishikawa, T. Tsutsumi, H. Kondo, and M. Hori.
10. Synthesis, characterization, and study of electrical properties of tin oxide-graphene composite synthesized by liquid phase plasma.	International Symposium on Advanced Plasma Science and its Applications for Nitrides and Nanomaterials, Nagoya Institute of Technology, Nagoya, Japan, March 17-21, 2019. (accepted)	R. Borude, H. Sugiura, K. Ishikawa, T. Tsutsumi, H. Kondo, and M. Hori.

